Study on Hot-Smoke Behavior from A Chimney Ejecting into Turbulent Crossflow

（乱流横風内に噴出された高温煙の挙動に関する研究）

January, 2023

Doctor of Philosophy (Engineering)

Xangpheuak INTHAVIDETH

サンクア インタビデ

Toyohashi University of Technology

Title	Study on Hot-Smoke Behavior from A Chimney Ejecting into Turbulent Crossflow
Author	Xangpheuak INTHAVIDETH
Degree	Doctor of Philosophy (Engineering)
Supervisors	Professor Dr. Yuji NAKAMURA Associate Professor Dr. Nobumasa SEKISHITA Associate Professor Dr. Takashi SUZUKI

ABSTRACT

This study aimed to investigate the hot-smoke dispersion behavior released from a chimney in turbulent crossflow experimentally using specially designed wind tunnel. Two turbulence generators were conducted which an artificially obtained quasi-isotropic turbulence was generated using an active turbulence generator developed by Makita and a rectangular grid to generate grid turbulence. A heated jet and an unheated jet with smoke were injected into the crossflow from the vertically oriented chimney installed in the test section. The chimney model with an inside diameter of d_i = 4 mm, an outside diameter of d_o = 20 mm, and a height of h = 200 mm, was placed on the floor of the wind tunnel test section. In this study, the experimental parameters considered were temperature of the heated jet (smoke), jet ejected velocity, and cross-wind velocity. Smoke motion was captured by high-speed camera to obtain instantaneous patterns of the smoke dispersion. Six kinds of the featured patterns were clearly identified, such as bifurcated vortex tubes with and without a strong mutual interaction (Mode I and Mode II), connected hairpin-type vortices (Mode III), the mixture of the coherent and turbulent vortices (Mode IV), the meandering motion (Mode V), and downwash structure (Mode VI). These smoke patterns in the downstream field from the chimney were found to be depended on buoyancy, turbulent motion, and inertia forces. Under the quasi-isotropic turbulence, the smoke dispersion preferred to exhibit a meandering pattern (Mode V) under wide range of adopted flow velocities, which was hardly observed using the grid turbulence test device. Interestingly, as compared to the unheated jet, the meandering smoke structure with heated jet ejection was also observed even at the lower jet velocities and the higher crossflow velocities, suggesting that the buoyancy force shall play an important role on appearance of meandering motion and control the smoke dispersion. Direct smoke exposure case (Mode VI) was preferred to be observed when the quasi-isotropic turbulence was imposed, although the trend of appearance

depending on the jet temperature could be predicted even using grid turbulent device. It was concluded that using grid turbulence would not be suitable to predict on the smoke dispersion problem in the actual scale. The time averaged smoke concentrations profiles were analyzed at locations along the crossflow direction, and it was revealed that the effective diffusion becomes stronger when the quasi-isotropic turbulence was imposed in the cross-wind. Further, it was confirmed that the smoke dispersion behavior can be well-characterized by the existing prediction method based on the point source model. In addition, two patterns were observed under the condition studied in the quasi-isotropic turbulence condition, such as meandering motion in downstream (Mode V) and downwash (Mode VI). The boundary of these two modes was found to be sensitive to all three parameters considered in this study, suggesting that all were similarly important to determine the boundary. The observed data were summarized in the physical plane to propose the potential scaling law of Reynolds number and jet-Froude number, and it was found that all plots were collapsed into the single line. This result suggested that the viscous effect around the chimney plays a role on the appearance of downwash pattern of the hot-smoke. This proposed scaling law worked well to describe the critical condition of the appearance of the downwash pattern under the condition studied in the present work. Moreover, the interpretation of the phenomena has been further made with the numerical approach to gain more detailed physics with the insightful understanding from scientific way for the downwash pattern, it was studied in the numerical simulation using the Fire Dynamics Simulator (FDS), Large Eddy Simulation (LES). The reason how the downwash occurs from the chimney was identified. Results shown that the downwash pattern occurred when the plume was drop down into low-pressure region in the wake of the chimney which caused by low-speed zones appear at behind of the chimney. When this appears, plume rise may be diminished, or in some cases, the effluent may be trapped in the wake and eddies of the chimney, which may result in high ground-level concentrations immediately downwind on the area.

ACKNOWLEDGEMENTS

My doctoral program was supported by scholarship program funded by Japan International Cooperation Agency Technical Cooperation Project for ASEAN University Network/Southeast Asia Engineering Education Development Network (JICA Project for AUN/SEED-Net). I would like to extend my sincere gratitude to all the staff members whom it may concern for the supports.

I would like to acknowledge the valuable assistance of the following people, without whose assistance and guidance this work would not have been possible.

First and foremost, I would like to express my sincere gratitude to my supervisors, Professor Dr. Yuji NAKAMURA, Associate Professor Dr. Nobumasa SEKISHITA, and Associate Professor Dr. Takashi SUZUKI for their invaluable advice continuous support and related research, for their patience, motivation, and immense knowledge. Their immense knowledge and plentiful experience have encouraged me in all the time of my academic research and daily life. Their guidance helped me in all the time of research and writing of this thesis. I could not have imagined having the better advisors and mentors for my PhD study.

Besides my advisors, I would like to express my sincere appreciation for dedicated work and for tremendous time made by Professor Dr. Hideki YANADA, Associate Professor Dr. Takashi SUZUKI, and Professor Dr. Tamio IDA (from Kindai University) to review my dissertation. They have provided valuable and fruitful comments on my dissertation. Their invaluable comments and hard work are greatly appreciated.

In addition, I would like to express my sincere gratitude to Professor Dr. (Emeritus) Toshihiro KITADA, Dr. Xiaoyu JU, Dr. Daiki MATSUGI, Associate Professor Dr. Tsuneyoshi MATSUOKA, and Assistant Professor Dr. Takuya YAMAZAKI for technical assistance and fruitful discussions.

For my laboratory members, I would like to appreciate all of members of the Energy Conversion Engineering laboratory (ECE lab) and Sekishita laboratory. Thank you very much for the supports from you all.

Finally, my appreciation also goes out to my family and friends for their encouragement and support all through my studies.

TABLE OF CONTENTS

LIST OF FIGURES

LIST OF TABLES

NOMENCLATURE

Symbol	Description	Unit
A_j	area of the chimney outlet	[m^2]
C	clearance length between the smoke dispersion and ground	[mm]
C	time averaged brightness intensity of each pixel	[-]
C_{max}	maximum pixel value of time averaged brightness intensity distribution	[-]
C_{min}	minimum pixel value of time averaged brightness intensity distribution	[-]
c_p	specific heat capacity	[kJ/kg K]
C_y	constant of Sutton's correlation	[$m^{n/2}$]
D^*	characteristic fire diameter	[m]
d_i	inside diameter of the chimney	[mm]
d_o	outside diameter of the chimney	[mm]
E_1	one-dimension energy spectra (*u*-spectrum)	[m^3/s^2]
E_2	one-dimension energy spectra (*v*-spectrum)	[m^3/s^2]
F_b	buoyancy force of smoke	[N]
F_{i_j}	inertia force of smoke	[N]
F_{i_w}	inertia force of wind	[N]
F_g	gravity force	[N]
F_v	viscous force	[N]
Fr	Froude number	[-]
Fr_j	jet-Froude number	[-]
g	gravity acceleration	[m/s^2]
H	effective height of the plume	[mm]
h	height of the chimney	[mm]
h_{req}	stack height required to avoid the downwash effect	[mm]
k	wavenumber	[m^{-1}]
L	distance between the turbulence generator and the chimney	[mm]
L_d	downwash length	[mm]

L_{UX}	longitudinal integral scale	[mm]
L_{VX}	lateral integral scale	[mm]
M	Mach number	[-]
M	momentum ratio	[-]
M	mesh size of the grid	[mm]
n	constant of Sutton's correlation	[-]
n	constant number of exponent	[-]
P	dynamic pressure	[Pa]
Pr	Prandtl number	[-]
Q_v	volume flow rate	[m^3/s]
$\dot{Q}$	heat release rate	[kW]
R_M	mesh Reynolds number	[-]
R_L	turbulence Reynold number (integral scale)	[-]
R_λ	turbulence Reynold number (microscale)	[-]
$R=(\rho_j U_j^2)/(\rho_0 U_0^2)$	momentum ratio	[-]
Re	Reynolds number	[-]
Re_d	Reynolds number	[-]
Re_M	mesh Reynolds number	[-]
$r=U_j/U_0$	velocity ratio	[-]
$S=\rho_j/\rho_0$	density ratio	[-]
T_a	ambient temperature	[K]
TI	turbulence intensity	[%]
U_0	mean velocity of cross-wind	[m/s]
U_j	jet velocity at the top of the chimney exit	[m/s]
u_{rms}/U_0	turbulence intensity	[%]
x/M	distance between turbulence generator and measurement point in x-axis	[-]
x	axial direction of cross-wind velocity	[-]
y/d_i	distance between floor of wind tunnel test section and measurement point in y-axis	[-]
y	axial direction of jet velocity from the chimney	[-]
z	axial direction of span-wise	[-]

Greek symbol	Description	Unit
$\Delta\theta$	temperature difference between the chimney and the cross-wind	[K]
ρ_{air}	density of air in the cross-wind	[kg/m^3]
ρ_a	density of air in the cross-wind	[kg/m^3]
ρ_0	density of air in the cross-wind	[kg/m^3]
ρ_j	density of smoke in the chimney	[kg/m^3]
ρ_{smoke}	density of smoke in the chimney	[kg/m^3]
μ	dynamic viscosity of the ambient air	[kg/m s]
μ_t	turbulent viscosity	[kg/m s]
α	Kolmogorov's universal constant	[-]
η	Kolmogorov dissipation scale	[mm]
λ	microscale	[mm]
λ_g	Taylor microscale	[mm]
σ_y	vertical dispersion parameter	[m]
σ_z	horizontal dispersion parameter	[m]
δx	nominal size of a mesh cell	[m]
γ_y	constant of Passqill&Grifford's correlation	[-]
γ_z	constant of Passqill&Grifford's correlation	[-]
α_y	constant of Passqill&Grifford's correlation	[-]
α_z	constant of Passqill&Grifford's correlation	[-]
Γ	adiabatic lapse rate	[^{o}C/km]
Π	pi-number	[-]

CHAPTER 1
INTRODUCTION

1.1 Introduction and motivation

Air pollution has been one of the serious social problems throughout the world. The air pollution is inherently linked to human activities. The air pollution including particle dispersion from industrial factories, motor vehicles, ordinary houses where coal is used for heating apparatus, etc., seriously affects ecosystems and human health for which the several millions of people die every year due to the atmospheric pollution (Aunan et al., 2019; Azagba et al., 2019; Bayat et al., 2019; Graber et al., 2019; Guo et al., 2019; John, 2019; Lee et al., 2019; Singh et al., 2019). Consequently, year by year, there is an increasingly high demand to assess the particle diffusion more precisely, e.g., the diffusion of $PM_{2.5}$, for the mitigation of grave air pollution problems, especially for the one released from the chimney as shown in Fig. 1.1. Due to increasingly strict standards, industrialists where impact of smoke released by the chimneys on the surrounding area are required to study the impact of chronic or accidental pollution caused by smoke released from the chimneys and assess the potential dangers to human health and the environment. Furthermore, understanding the rate and patterns of particle diffusion, such as the smoke released by the chimneys on the surrounding area, are crucial for environmental planning (location) and for forecasting high pollution episodes (above legislation thresholds including detrimental effects on human health, ecosystems, and/or materials). As summarized, there are two points to be addressed on the aforementioned engineering demand, one is “(1) how quickly the smoke shall be dispersed” and the other is “(2) how to occur the direct exposure of the generated smoke”. Scientifically, therefore, it is preferable to provide the universal rule to describe the smoke dispersion behavior in a precise manner and figure out key essences to cause the direct exposure of the smoke, which are the motivation of the present work. From fundamental point of view, this problem is regarded as the turbulent heat and mass transfer including smoke in a hot jet flow ejected from the chimney. Because the smoke is released with hot emission gas, buoyancy may play a role on the subsequent dispersion behavior, nevertheless, the past work on smoke dispersion is neglected such effect. Furthermore, although the meandering smoke pattern has been often observed in the actual phenomena, it has been hardly seen in the laboratory scale experiment using the wind tunnel (Sekishita et al., 2019). Obviously, these facts clearly show the room to study on this subject,

especially the effect of adopted turbulent condition on the observed smoke patterns in the first place.

Fig. 1.1 Example of smoke dispersion from industrial chimney.

Many researches on the smoke dispersion from a chimney were conducted by using a wind tunnel and water tunnel as shown in Table 1.1 (Baouabe et al., 2011; Brusca et al., 2015; Gifford, 1959; Gupta et al., 2012; Huang and Hsieh, 2002; Huber and Snyder, 1976; Leelossy et al., 2014; Majeski et al., 2010; Raman and Ramachandran, 2010; Said et al., 2005; Taylor, 1959). Extensive results into these wind tunnel experiments were presented and compared with theory, field measurement, and numerical simulation results. Several theoretical researches were carried out in this field with a lack of experimental data comparison (Brusca et al., 2015; Gifford, 1959; Leelossy et al., 2014; Taylor, 1959). For example, Brusca et al. (2015) investigated the interaction of a continuous plume released from a point source with various obstacles. Baouabe et al. (2011) used particle image velocimetry (PIV) to measure velocity field around a chimney, and to describe its flow structure. The flow structure and vortex topology were studied under variety of oncoming flow conditions using flow visualization techniques. New et al. (2006) experimentally investigated the effects of jet velocity profiles on the flow field of a round jet in a cross flow. Gupta et al. (2012) investigated the downwash effect of a rooftop structure (RTS) on plume dispersion in wind tunnel experiments. Said et al. (2005) used PIV to investigate the coherent structures in the near-wake region of a turbulent round-jet ejected perpendicularly from a chimney into a cross flow. Huang and Hsieh (2002) classified the jet structure based on the momentum ratio between the cross-wind and the jet velocity. Four characteristic types of flows with apparent differences were identified such as downwash, cross-wind dominant flow, transitional flow, and jet dominant flow. Majeski et al. (2010) proposed a phenomenological model for predicting the size of a low-momentum jet diffusion flame diluted with an inert gas in a cross flow. Huber and Snyder (1976) reported concentration measurements for an elevated point source placed in the lee of a two-dimensional Gaussian

model ridge, the height of which was about one-third of the boundary layer thickness. Their results demonstrated the occurrence of significant ground level concentration upwind of the stack source when it was placed at the ridge base within the lower part of the cavity region. Pournazeri et al. (2012) presented a method for scaling the urban dispersion parameters in water channel and wind tunnel. Their results shown that plume rise associated with relatively low-level buoyant sources in urban areas is highly affected by the complex flows induced by surrounding buildings, an effect which current plume rise models are not able to accurately reproduce. Sherlock and Stalker (1941) and Briggs (1973) were point out that the downwash would not occur in the range $U_j \geq 1.5\ U_0$, namely, the ratio of the jet velocity to the mean wind velocity should be greater than 1.5 to avoid downwash pattern. However, this is true irrespective of the imposed inlet turbulent conditions especially the quasi-isotropic turbulence. In addition, Snyder and Lawson (1991) stated that downwash from non-buoyant jets occurs if the speed ratio is less than about 1.5 in the subcritical regime (light wind) and about 1.1 in the supercritical regime (strong wind). In addition, in power plants the gases leave the stacks with temperature from 120 ^{o}C to 190 ^{o}C (Sherlock and Lesher, 1954) or around 150 ^{o}C to 250 ^{o}C (Michael, 2021). Moreover, Briggs (1969) stated that plume dispersion is most easily described by discussing separately three aspects of plume behavior: (1) aerodynamic effects due to the presence of the stack, buildings, and topographical features; (2) rise relative to the mean motion of the air due to the buoyancy and initial vertical momentum of the plume; and (3) diffusion due to turbulence in the air. In reality all three effects can occur simultaneously, but in the present state of the art they are treated separately and are generally assumed not to interact.

Table 1.1 Previous studies on smoke dispersion.

Investigator	Fluid	Size (H×W×L) [m]	d_o [mm]	h [m]	r	TI (%)
Brusca et al., 2015	Air	0.500×0.500×1.130	20	0.090	0.6	-
Baouabe et al., 2011	Air	0.300×0.200×3.000	10	0.100	0.5-1.6	<0.2
New et al., 2006	Water	0.400×0.400×1.800	13.5	-	2.3-5.8	-
Gupta et al., 2012	Air	1.800×1.800×12.200	600	4.000	0.02	18-27
Said et al., 2005	Air	0.300×0.200×3.000	12	0.100	1.2-3.3	<0.2
Huang and Hsieh, 2002	Air	0.030×0.030×0.110	6.4	0.560	0.57-23.1	0.2-0.8

Although the rich past attempts have been made, it is worthwhile to note that these works have been performed with the wind tunnel using high-drag strakes, roughness blocks, a turbulence grid in order to generate the incoming turbulence in the wind. Obviously, such technique may not be enough to reproduce the actual turbulent field as pointed out by Makita (Makita, 1991). In addition, Batchelor (1953) suggested that it was difficult for the grid-induced turbulence in a laboratory wind tunnel to attain turbulence Reynolds numbers large enough to have a clear inertial subrange in energy spectra. The turbulence Reynolds number based on Taylor's microscale, R_λ, has scarcely exceeded 100 in conventional grid turbulence experiments, namely, the turbulence Reynolds numbers, R_λ, obtained in the conventional grid turbulence of about $R_\lambda \leq 100$ are not satisfactorily large to verify the hierarchical nature of the turbulence fields. Because it cannot be endowed with a wide inertial subrange satisfying the -5/3 law for more than two orders of magnitude in wave number in the spectrum. This fact means that the turbulent eddy motion could not accomplish most essential roles in transfer mechanism in such a small-scale field (Makita, 2007). Corrsin (1958) suggested that the inertial subrange could not be observed in the energy spectrum for $R_\lambda < 250$. The term "turbulence" means the state of a flow in which the inertial motion of turbulent eddies makes a dominant role in energy and momentum transfer in the wavenumber space. Therefore, attaining a sufficiently large value of R_λ is one of the most essential demands for wind-tunnel experiments either to clarify the physical nature of turbulence or to conduct some simulation experiments on practical large scale flow fields, such as wind-environmental problems and atmospheric turbulence. Furthermore, the meandering smoke pattern has been often observed in the actual phenomena (e.g., shown in Fig. 1.1), it has been hardly seen in the laboratory scale experiment using the wind tunnel as pointed out by Sekishita et al. (2019). This is because the smoke released from the chimney with hot emission gas is transported by wind and diffused by turbulent conditions in the atmosphere. Consequently, the precise smoke dispersion behavior is believed to depend on the large-scale turbulent eddy in the cross-wind and buoyancy of the hot plume ejected through the chimney which is motivated to address these issues in this research. Smoke patterns appear randomly one the smoke was issued from the chimney in the cross-wind atmosphere. However, the patterns are mainly categorized into several typical ones based on the characteristic motion of the smoke behind the chimney. With special attention should be paid to the downwash smoke pattern, such that the ejected smoke is "pushed back" to downward and smoke is distributed toward the ground behind the chimney. This is the serious problem for actual chimneys. Once this mode appears, the people living in downstream region behind the chimney are directly exposed the

harmful gas to potentially cause the severe health damage, which must be prevented (Huang and Hsieh, 2002; Overcamp, 2001; Canepa, 2004; Gnatowska, 2015; Sekishita et al., 2019). Therefore, the higher-order prediction of the appearance of downwash patterns ejected from the high-rise chimney in the natural wind is strongly demanded. Consequently, this study will introduce the law approach to obtain the scaling law for this problem to determine the appearance of the downwash pattern in feasible and universal which is the target of this research objective. Furthermore, in order to construct a turbulent diffusion model for the environmental assessment and prediction of atmospheric dispersion from a point source such as a chimney, having wind tunnel which allows to generate the turbulence in the real scale and observing the path of the smoke ejecting with the hot plume to include the buoyancy effect on the dispersion is essential for the investigation and the precise estimation of smoke dispersion. In addition, in order to investigate the mechanism of the turbulence diffusion of the smoke, it is made in laboratory experiments using a wind tunnel. It is necessary for its wind tunnel testing to realize the smoke dispersion which is similar in an actual atmospheric boundary layer for the more precise estimation of the smoke dispersion which is useful in air pollution assessment and anti-pollution measures. Consequently, the wind tunnel experiments of a buoyancy jet with the smoke vertically ejected into the crossflow, which has large-scale turbulent eddies, are conducted to investigate and to estimate the smoke dispersion from the chimney.

1.2 Research purposes

In order to fulfill the motivation as described in Introduction section, this research aims: (1) to investigate the patterns of smoke dispersion ejecting with hot-smoke from a chimney and its occurrence conditions in a rectangular grid (to generate grid turbulence) and an active turbulence grid (to promote quasi-isotropic turbulence), (2) to elucidate the scaling law of the critical condition on appearance of the downwash pattern of the hot-smoke ejected from the chimney in turbulent crossflow, and (3) to investigate the reason how the downwash occurs and what is the key to appear the downwash pattern of smoke ejected from the chimney.

1.3 Research plan and results expected

Flow visualization experiments are conducted by a high-speed camera (1000frame/s) for distinguishing smoke dispersion patterns from the chimney. The smoke structures, such as a meandering pattern, a downwash pattern, etc., are classified depending on turbulent filed, the

mean velocity in the cross-wind, U_0, the jet velocity, U_j, and the temperature difference between the cross-wind and the jet from the chimney, $\Delta\theta$; and investigate the smoke structures due to velocity shear, turbulent motion, and buoyancy; and investigate the cause of the occurrence of these smoke structures. In addition, these occurrence conditions are clarified depending on the flow conditions and temperature difference between the cross-wind and the chimney. For each smoke structures, the smoke diffusion width and the difference between the distribution for the quasi-isotropic turbulence and the grid turbulence fields are investigated. Furthermore, the scaling law is elucidated to provide the critical condition on appearance of the downwash pattern of the hot-smoke ejected from the chimney in the turbulent crossflow, which is quite important to predict the smoke dispersion and direct exposure to cause health damage. Moreover, to have an in depth understanding of the downwash pattern of the smoke ejected from the chimney, the interpretation of the phenomena has been further made with the numerical approach by computational fluid dynamics (CFD) simulation. This technique which is based on numerical models can be more advantageous than the experimental methods in many ways, such as the richness of the quantitative results, low cost, and rapid turnaround time. The reason how the downwash occurs and what is the key to appear the downwash pattern of smoke ejected from the chimney are identified, which can contribute the prevention of dangerous situation by determining in advance effluents could cause a high concentration of harmful effluents in a particular area. Based on the above explanation, is presented to Fig. 1.2.

1.4 Outline of the thesis

The thesis is organized in the following manner: Chapter 2 presents the fundamentals of wind tunnel, turbulent flow, smoke plume, and nondimensional analysis; and a brief review of past research on smoke dispersion and smoke downwash. Chapter 3 discusses in detail the methodologies and conditions of the experimental and numerical, while Chapter 4 discusses the main findings from wind tunnel experiments. Chapter 5 proposes the scaling law to provide the critical condition on appearance of the downwash pattern, and Chapter 6 elucidates the reason how the downwash pattern occurs. Finally, the conclusions and future works of the present study, and suggestions for future research are presented in Chapter 7. Furthermore, the Gaussian plume model, the dispersion parameters, scale modeling and the law approach, and glossary of terms are indicated in Appendices section. The list of publications is listed in the Appendix E.

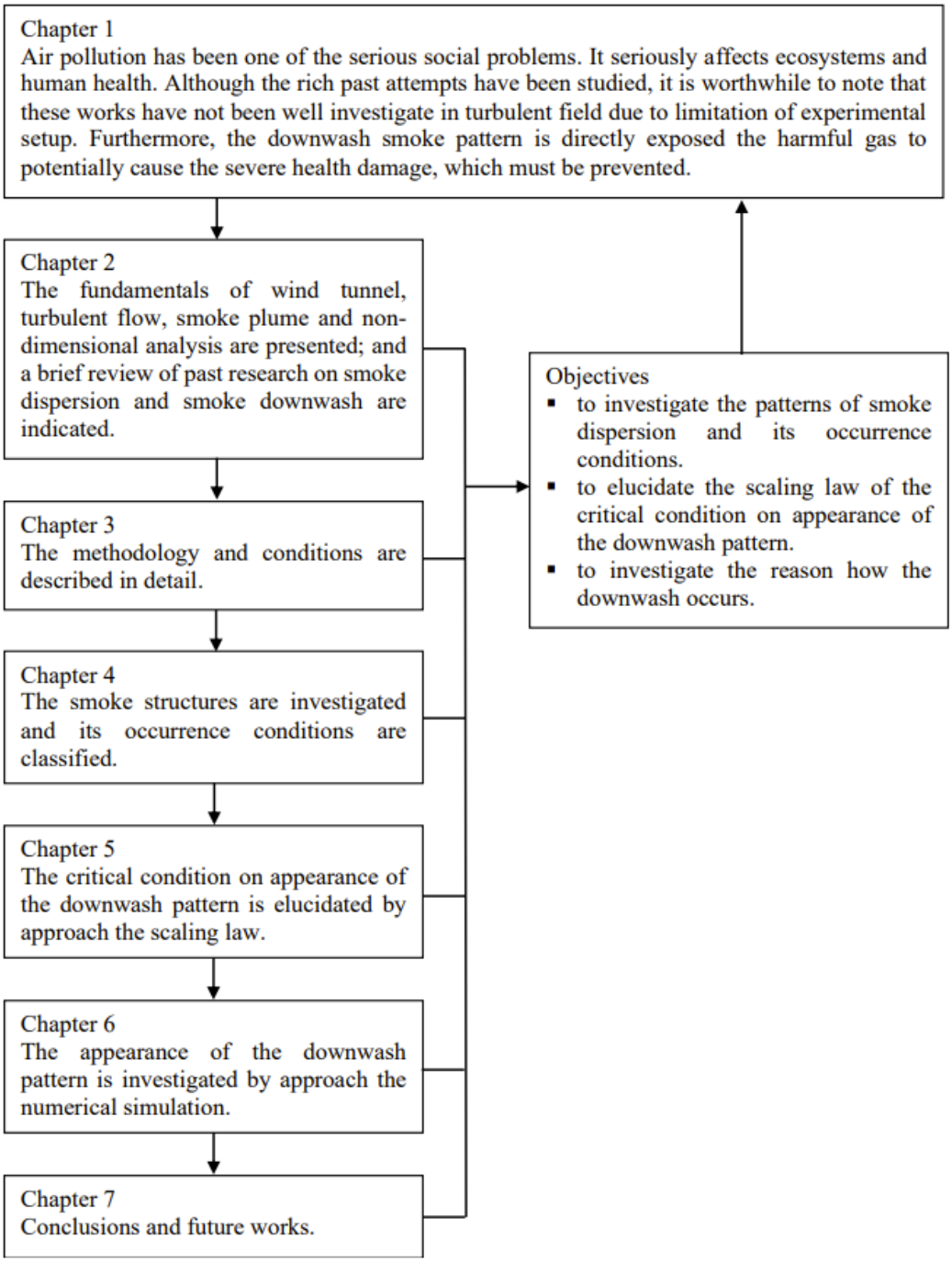

Fig. 1.2 Organization (flowchart) of this thesis.

CHAPTER 2
FUNDAMENTAL AND LITERATURE REVIEWS

Having stated research objectives in first chapter, a new strategy to understand the phenomenon of smoke dispersion will be paid an attention. The link should also be clear and highly strong for summarizing and filling this empty fundamental.

2.1 Fundamental

2.1.1 Wind tunnel

A wind tunnel is a specially designed and protected space into which air is drawn, or blown, by mechanical means in order to achieve a specified speed and predetermined flow pattern at a given instant. The flow so achieved can be observed from outside the wind tunnel through transparent windows that enclose the test section and flow characteristics are measurable using specialized instruments. An object, such as a model, or some full-scale engineering structure, typically a vehicle, or part of it, can be immersed into the established flow, thereby disturbing it. The objectives of the immersion include being able to simulate, visualize, observe, and/or measure how the flow around the immersed object affects the immersed object.

2.1.1.1 Classifications of wind tunnel

Wind tunnels can be classified using four different criteria. Four such criteria are presented. (Lerner, 2011; Rae and Pope, 1984)

Type 1 classification – The criterion for classification is the path followed by the drawn air: Open- vs. closed-circuit wind tunnels.

Open-circuit (open-return) wind tunnel: if the air is drawn directly from the surroundings into the wind tunnel and rejected back into the surroundings, the wind tunnel is said to have an open-air circuit. A diagram of such a wind tunnel is indicated in Fig. 2.1. An open-circuit wind tunnel is also called an open-return wind tunnel.

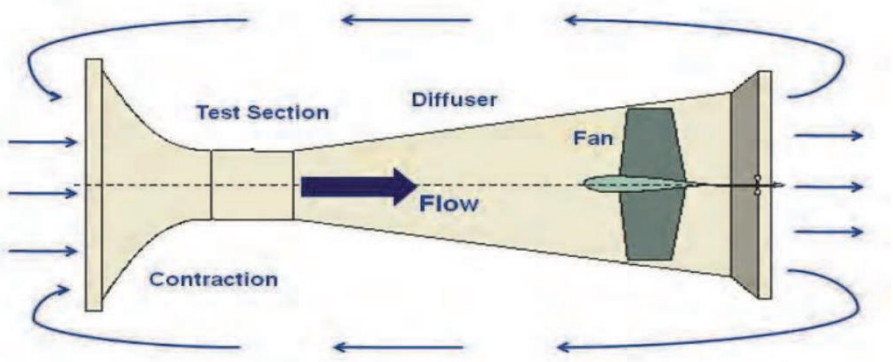

Fig. 2.1 Diagram of an open-circuit, also known as open-return, wind tunnel (from NASA) (Lerner, 2011).

Closed-circuit (closed-return) wind tunnel: if the same air is being circulated in such a way that the wind tunnel does neither draw new air from the surrounding, not return it into the surroundings, the wind tunnel is said to have a closed-air circuit. It is conventional to call that a closed-circuit (closed-return) wind tunnel. Fig. 2.2 illustrates this configuration.

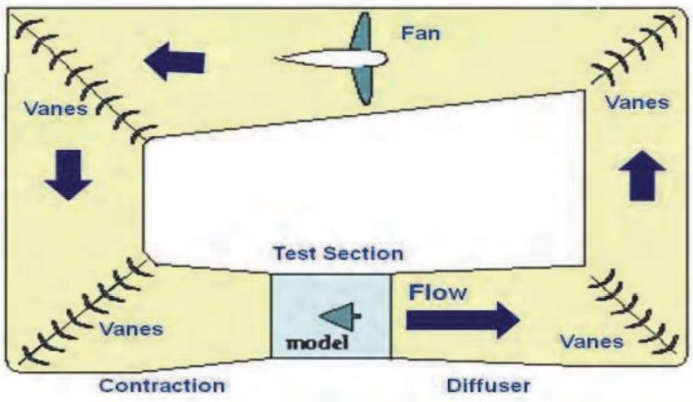

Fig. 2.2 Top view of a closed-circuit, also known as closed-return, wind tunnel (NASA) (Lerner, 2011).

Type 2 classification

The criterion for classification is the maximum speed achieved by the wind tunnel: subsonic vs. supersonic wind tunnels. It is traditional to use the ratio of the speed of the fluid, or of any other object, and the speed of sound. That ratio is called the Mach number, named after

Ernst Mach, the 19th century physicist. The classification is summarized in Table 2.1. Schematic designs of subsonic and supersonic wind tunnels are compared in Fig. 2.3.

Subsonic wind tunnel: if the maximum speed achieved by the wind tunnel is less than the speed of sound in air, it is called a subsonic wind tunnel. The speed of sound in air at room temperature is approximately 343 m/s, or 1235 km/hr. The Mach number, M <1.

Supersonic wind tunnel: if the maximum speed achieved by the wind tunnel is equal to or greater than the speed of sound in air, it is called a supersonic wind tunnel.

Table 2.1 Classification of flows based upon their Mach numbers (Lerner, 2011).

Range of the Mach number , M	Name of flow , or conditions
M<1	Subsonic
M=1, or near 1	Transonic
1<M<3	Supersonic
3<M<5	High supersonic
M>5	Hypersonic
M>> 5	High Hypersonic

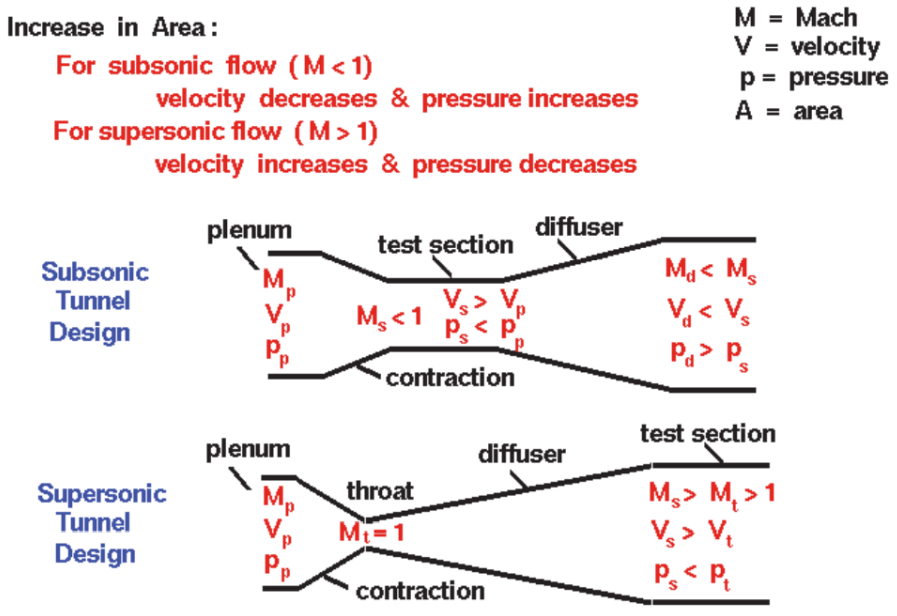

Fig. 2.3 Schematic designs of subsonic and supersonic wind tunnels (NASA) (Lerner, 2011).

Type 3 classification

The criterion for classification is the purpose for which the wind tunnel is designed: research or education. If the wind tunnel is for research, it is called a research wind tunnel. If, however, it is designed to be used for education, then, it is called an educational wind tunnel.

Type 4 classification

The criterion for classification is the nature of the flow: laminar vs. turbulent flow. Boundary layer wind tunnels are used to simulate turbulent flow near and around engineering and manmade structures.

2.1.1.2 Advantages and disadvantages of wind tunnel

As with any engineering design, there are advantages and disadvantages with both the open- and closed-circuit type wind tunnels. In general, the type of tunnel decided upon depends on funds and purpose. (Rae and Pope, 1984)

An open-circuit wind tunnel has the following advantage and disadvantages:

Advantages:

1. Construction cost is less.
2. If one intends to run internal combustion engines or do much flow visualization via smoke, there is no purging problem if both inlet and exhaust are open to the atmosphere.

Disadvantages:

1. If located in a room, depending on the size of the tunnel to the room size, it may require extensive screening at the inlet to get high-quality flow. The same may be true if the inlet and/or exhaust is open to the atmosphere when wind and cold weather can affect operation.
2. For a given size and speed the tunnel will require more energy to run. This is usually a factor only if used for developmental testing where the tunnel has a high utilization rate.
3. In general, a tunnel is noisy. For larger tunnels (test section of 70 ft^2 (21.33 m^2) and more) noise may cause environmental problems and limits on hours or operation.

Because of the low initial cost, an open-circuit wind tunnel is often ideal for schools and universities where a wind tunnel is required for classroom work and research and high utilization is not required.

A closed-circuit wind tunnel has the following the advantages and disadvantages:

Advantages:

1. Through the use of corner turning vanes and possibly screens, the quality of the flow can be easily controlled.
2. Less energy is required for a given test-section size and velocity. This can be important for a tunnel used for developmental testing with high utilization (two or three shifts, five to six days a week).
3. Less noise when operating.

Disadvantages:

1. Higher initial cost due to return ducts and corners vanes.
2. If used extensively for smoke tests or running of internal combustion engines, there must be a way to purge tunnel.
3. If tunnel has high utilization, it may have to have an air exchanger or some other methods of cooling during hot summer months.

2.1.2 Turbulent flow

Turbulent flows are characterized by irregular patterns, unpredictable behavior and the existence of numerous space and time scales. They appear when the source of kinetic energy which drives the fluid in motion is intense and able to overcome the viscosity effects that slow down the fluid. When viscosity predominates, the flow is said to be laminar, and hence regular and predictable. The pioneering work of Reynolds (1883, 1895) has defined the first concepts in the study of the turbulent regime. The energy source in a flow can be of various natures: pressure gradients in a pipe flow, initial impulsion for jets, or temperature differences in heated flows where buoyancy takes place.

At the scale of the Earth, solar radiation as well as long range attractive gravitational forces are involved. Oceanic currents such as the Gulfstream in the Atlantic Ocean or the Humboldt stream in the Pacific Ocean have a mean regular motion. Intensity and position fluctuations are, however, observed. The same is true for atmospheric winds. Fig. 2.4 displays a map of the winds over the Atlantic Ocean. These maps are used to improve our understanding

of weather abnormalities. At high altitudes, the jet streams, with speeds up to 100 km/h, are exploited by plane pilots to optimize their itinerary. Images taken by satellites for weather forecasting are another good daily illustration of the existing irregularities in geophysical flows. Turbulence is therefore encountered everywhere in our terrestrial environment. In astrophysics, the ionized gaseous atmospheres of stars and nebulas are also turbulent, induced by powerful nuclear reactions occurring in their core and leading to an electromagnetic forcing of the flow. Solar winds and Jupiter's red spot are other fascinating examples.

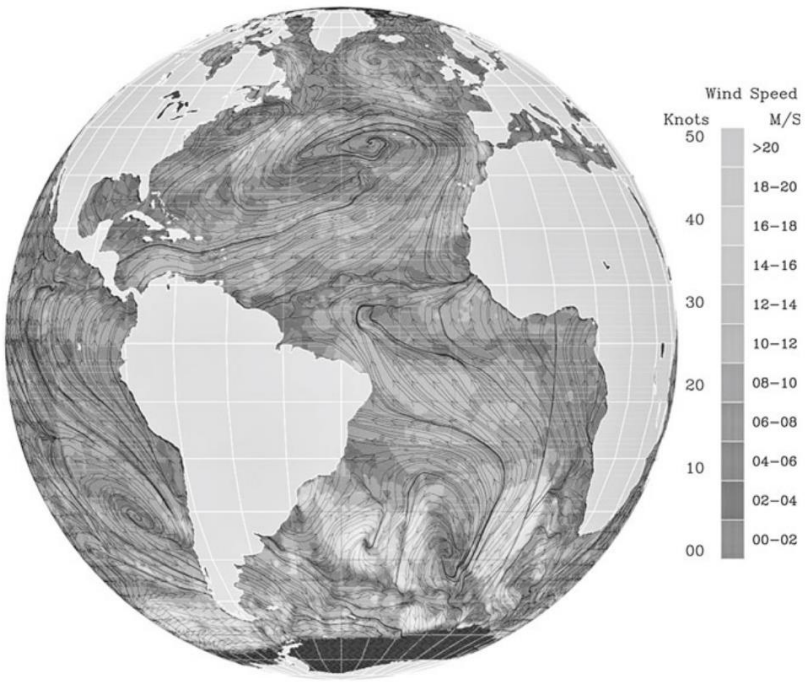

Fig. 2.4 Near-surface wind speeds 10 m above the Atlantic Ocean on August 1, 1999. Data collected by the Sea Winds scatter meter onboard NASA's QuikSCAT satellite. Courtesy of NASA's Jet Propulsion Laboratory (Bailly, 2015)

In most industrial applications, substantial energy input or loss often occurs as well. In aeronautics, the high speed and high temperature jet of engines or the relatively low speed wakes generated by the compressor and turbine blades are turbulent. In chemical engineering, turbulence appears in complex confined geometries, especially in the combustion chambers of cars, planes, and space launchers. Turbulence, indeed, plays an efficient role in mixing reactants. We use turbulent mixing daily when adding cream to our coffee or tea. A key contribution is played by the spoon that is turned to achieve a homogeneous beverage. In nuclear engineering, turbulence increases thermal exchange in cooling systems. In acoustics,

turbulence disturbs the propagation of sound waves in the atmosphere or in the ocean. Turbulence itself is also an important noise source, the so-called mixing noise in aeroacoustics. It may also induce vibration of structures and fatigue. Noise induced by wall pressure fluctuations is regularly encountered in mechanical engineering including sonar domes in underwater applications, aircraft and car cabin noise, or the protection of payloads during space launcher lift-off, among many other examples.

Fig. 2.5 Eruption of the subglacial Grimsvötn volcano, Iceland, on May 21, 2011. An initial large plume of smoke and ash rose up to about 17 km height. Until May 25 the eruption scale was larger than that of the 2010 eruption of the Eyjafjallajökull volcano, but did not lead to the air travel chaos caused in April 2010. Courtesy of Thördïs Högnadóttir, Institute of Earth Sciences, University of Iceland (Bailly, 2015)

Turbulent flows can be directly observed, sometimes in a quite spectacular way, as during a volcanic eruption for instance. Intermittent bursts deforming the free plume boundaries are shown in Fig. 2.5. In laboratories, various flow visualization techniques have been developed. For example, emission lines captured in a subsonic round jet are shown in Fig. 2.6. An electrically heated thin wire is placed near the nozzle and oil droplets along the wire produce lines of oil vapor which allow flow visualization for a sufficiently small jet velocity. The picture is taken when the first particles reach the downstream side, while others are still on the wire.

Large fluctuations are visible near the free edges of the flow, and the vanishing of emission lines downstream corresponds to tridimensional motions out of the visualization plane. Turbulent flows are not only characterized by random fluctuations, but also by the presence of coherent structures. This coexistence has been noted in the literature since the 1950s, but it has been dramatically highlighted by the experiments in jets, and in mixing layers. The appearance of coherent structures in the first diameters of a jet is linked to the laminar transition occurring at the nozzle exit. They are also present in mixing layers as illustrated in Fig. 2.7. These large vortical structures are fairly well described by the inviscid stability theory and by the so-called Kelvin-Helmholtz waves, at least during their linear growth. In addition, more detailed and careful observations can be made in laboratory experiments as shown in Fig. 2.8 and Fig. 2.9 of a turbulent jet at different Reynolds numbers.

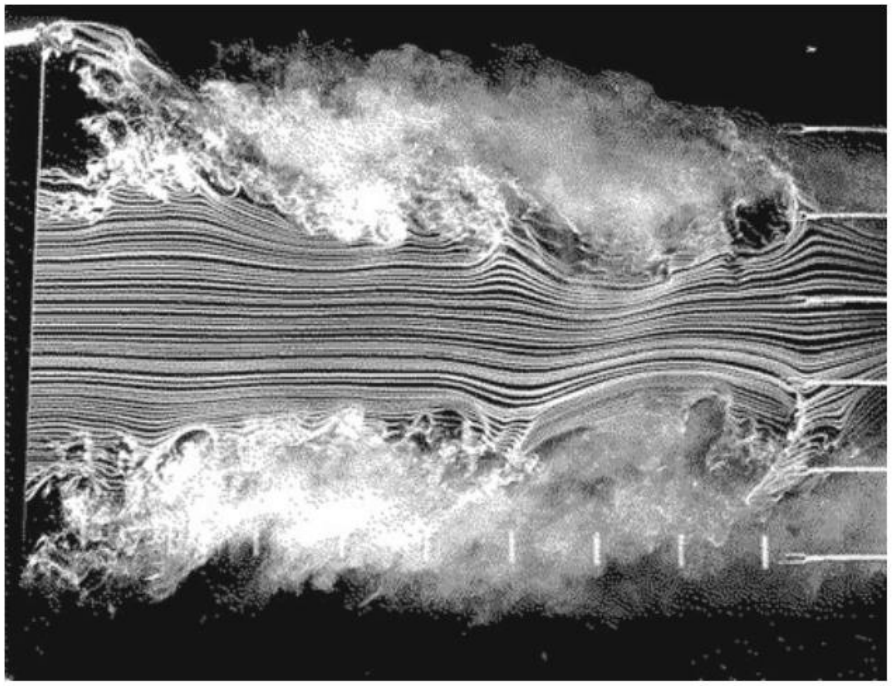

Fig. 2.6 Visualization of emission lines in a round air jet. The nozzle diameter is D = 15 cm, the jet velocity is u_j = 5 m/s and the Reynolds number is $Re_D = u_j D/\nu = 5.4 \times 10^4$. The hot wire eating the oil droplets is placed 0.5D downstream of the nozzle. In addition, 6 hot-wire probes are located downstream at 4D. Courtesy of Henry Fiedler (Bailly, 2015)

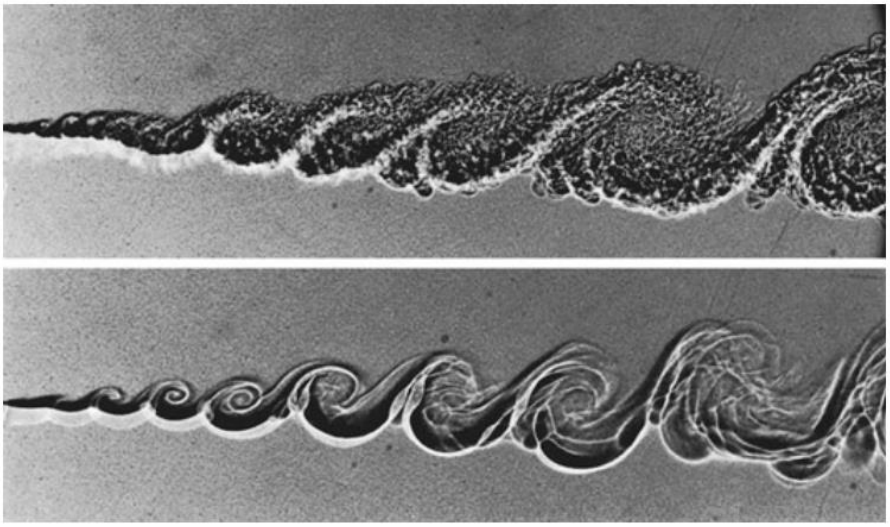

Fig. 2.7 Ombroscopy of a mixing layer between an helium flow at 10 m/s (above) and a nitrogen flow at 3.8 m/s (below). The Reynolds number of the upper flow is ten times higher than that of the lower flow. This variation is obtained by increasing the pressure, and consequently the density of the fluid. An increase in the Reynolds number produces more small structures within the large scales arising from Kelvin-Helmholtz instability waves during the initial laminar mixing at the trailing edge. (Bailly, 2015)

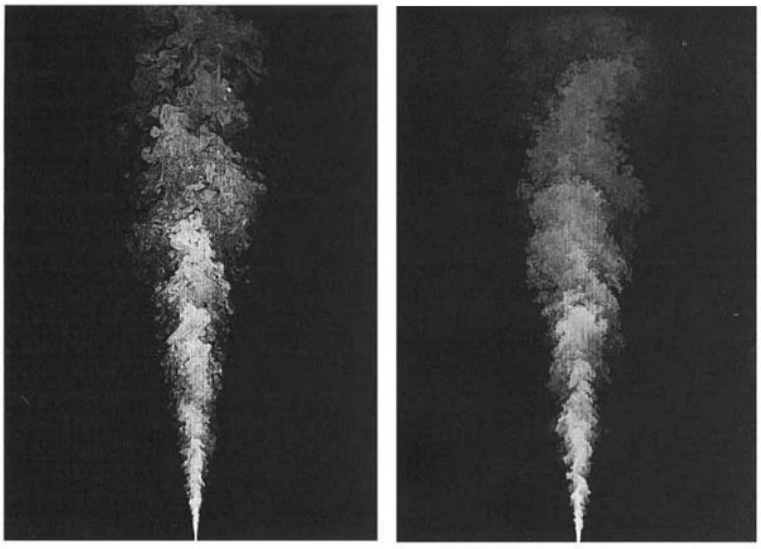

Fig. 2.8 Planar images of concentration in a turbulent jet: Left: Re=5000 and Right: Re=20000 (Dahm and Dimotakis, 1990).

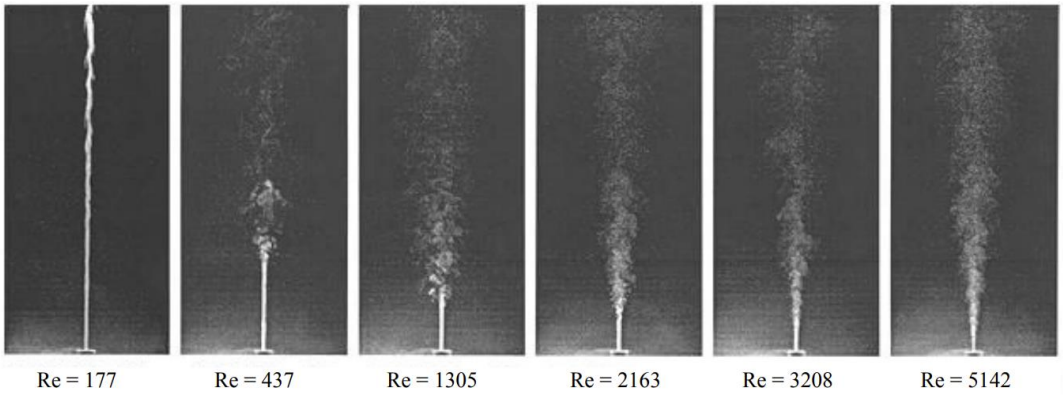

Fig. 2.9 Evolution of the round jet with increasing Reynolds Number (Kwon and Seo, 2005).

For generating the turbulence, a turbulence grid has been a popular tool in a wind tunnel since Simmons and Salter (1934) employed it (Makita, 1991). It has a simple configuration and can easily generate homogeneous, quasi-isotropic turbulence in a wind tunnel. Since it can offer experimental researchers on fluid dynamics well-defined experimental conditions, the grid-induced turbulence field is still widely used in a variety of experiments on turbulence phenomena. Batchelor (1953) suggested that it was difficult for the grid-induced turbulence in a laboratory wind tunnel to attain turbulence Reynolds numbers large enough to have a clear inertial subrange in energy spectra. The turbulence Reynolds number based on Taylor's microscale, R_λ, has scarcely exceeded 100 in conventional grid turbulence experiments, namely, the turbulence Reynolds number, R_λ, obtained in the conventional grid turbulence of about $R_\lambda \leq 100$ is not satisfactorily large to verify the hierarchical nature of the turbulence fields. Because it cannot be endowed with a wide inertial subrange satisfying the -5/3 law for more than two orders of magnitude in wave number in the spectrum. This fact means that the turbulent eddy motion could not accomplish most essential roles in transfer mechanism in such a small-scale field (Makita, 2007). Corrsin (1958) suggested that the inertial subrange could not be observed in the energy spectrum for $R_\lambda < 250$ (Makita, 1991). The term "turbulence" means the state of a flow in which the inertial motion of turbulent eddies makes a dominant role in energy and momentum transfer in the wavenumber space. Therefore, attaining a sufficiently large value of R_λ is one of the most essential demands for wind-tunnel experiments either to clarify the physical nature of turbulence or to conduct some simulation experiments on practical large scale flow fields, such as wind-environmental problems and atmospheric turbulence.

2.1.3 Smoke

Smoke is a collection of airborne particulates and gases emitted when a material undergoes combustion or pyrolysis, together with the quantity of air that is entrained or otherwise mixed into the mass. It is commonly an unwanted by-product of fires (including stoves, candles, internal combustion engines, oil lamps, fireplaces, etc.), but may also be used for pest control (fumigation), communication (smoke signals), defensive and offensive capabilities in the military (smoke screen), cooking, or smoking (tobacco, cannabis, etc.). It is used in rituals where incense, sage, or resin is burned to produce a smell for spiritual or magical purposes. It can also be a flavoring agent and preservative. Smoke inhalation is the primary cause of death in victims of indoor fires. The smoke kills by a combination of thermal damage, poisoning and pulmonary irritation caused by carbon monoxide, hydrogen cyanide, and other combustion products.

Smoke is a collection of tiny solid, liquid, and gas particles. Although smoke can contain hundreds of different chemicals and fumes, visible smoke is mostly carbon (soot), tar, oils, and ash. Smoke occurs when there is incomplete combustion (not enough oxygen to burn the fuel completely). In complete combustion, everything is burned, producing just water, and carbon dioxide. When incomplete combustion occurs, not everything is burned. Smoke is a collection of these tiny unburned particles. Each particle is too small to see with your eyes, but when they come together, you see them as smoke.

2.1.4 Behaviors of smoke plumes

Plume dispersion is most easily described by discussing separately three aspects of plume behavior: (1) aerodynamic effects due to the presence of the stack, buildings, and topographical features; (2) rise relative to the mean motion of the air due to the buoyancy and initial vertical momentum of the plume; and (3) diffusion due to turbulence in the air (Briggs, 1969). In reality all three effects can occur simultaneously, but in the present state of the art they are treated separately and are generally assumed not to interact. This is probably not too unrealistic an assumption. We know that undesirable aerodynamic effects can be avoided with good chimney design. Clearly the rise of a plume is impeded by mixing with the air, but there is not much agreement on how important a role atmospheric turbulence plays. It is known that a rising plume spreads outward from its center line faster than a passive plume, but this increased diffusion rate usually results in an only negligible decrease of ground concentrations.

2.1.4.1 Downwash and aerodynamic effects on smoke plume

All large structures distort the atmosphere and interfere with wind flow to some extent. These atmospheric distortions usually take the form of a wake, which consists of a pocket of slower, more turbulent air. If a plume is emitted near a wake, it is usually pulled down because of the lower pressure in the wake region. This effect is termed downwash. When downwash occurs, the plume is brought down to the ground near the emission source more quickly.

Downwash of the plume into the low-pressure region in the wake of a stack can occur if the efflux velocity is too low. If the stack is too low, the plume can be caught in the wake of associated buildings, where it will bring high concentrations of effluent to the ground and even inside the buildings. A similar effect can occur in the wake of a terrain feature. These three effects are illustrated in Fig. 2.10.

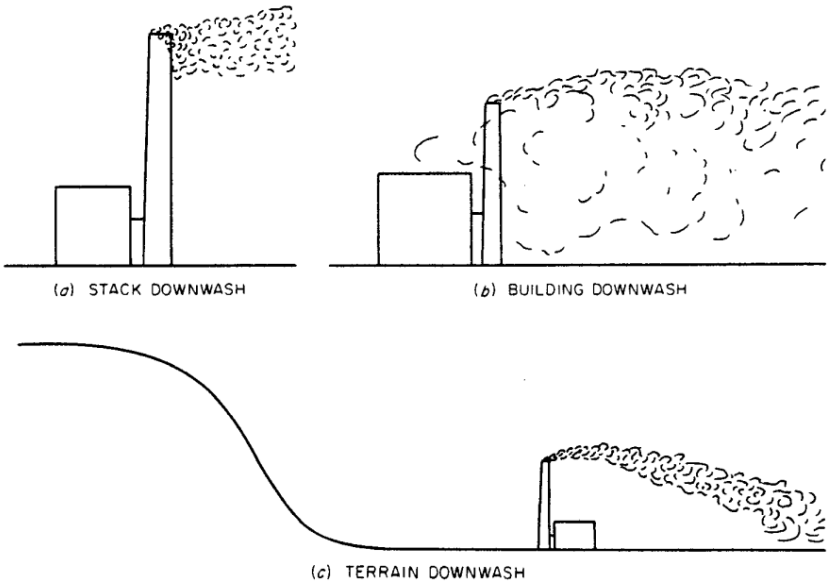

Fig. 2.10 Undesirable aerodynamic effects (Briggs, 1969).

Experiments are still needed to determine quantitatively the effect of the efflux Froude number (*Fr*) on the abatement of downwash, unfortunately, the experiments of Sherlock and Stalker involved only high values of *Fr*, and thus buoyancy was not a significant factor. One of the most enduring rules of thumb for stack design was a recommendation made in 1932 that stacks be built at least 2.5 times the height of surrounding buildings, as illustrated in Fig. 2.11.

If such a stack is designed with sufficient efflux velocity to avoid downwash, the plume is normally carried above the region of downflow in the wake of the building. If the stack height or efflux velocity is slightly lower, in high winds the plume will get caught in the downflow and be efficiently mixed to the ground by the increased turbulence in the wake of the building. Still, this is only a rough rule, because the air-flow pattern around a building depends on the particular shape of the building and on the wind direction. It is much more difficult to give any rules about the effect of terrain features, partly because of the great variety of possibilities.

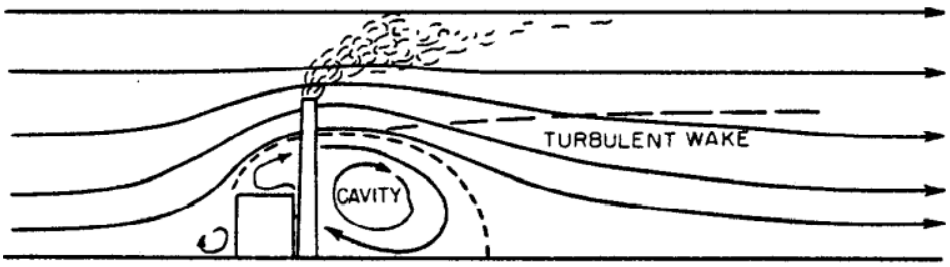

Fig. 2.11 Flow past a typical power plant (Briggs, 1969).

2.1.4.2 Plume rise of smoke

The gases are turbulent as they leave the stack, and this turbulence causes mixing with the ambient air; further mechanical turbulence is then generated because of the velocity shear between the stack gases and the air. This mixing, called entrainment, has a critical effect on plume rise since both the upward momentum of the plume and its buoyancy are greatly diluted by this process. The initial vertical velocity of the plume is soon greatly reduced, and in a cross-wind the plume acquires horizontal momentum from the entrained air and soon bends over.

Once the plume bends over, it moves horizontally at nearly the mean wind speed of the air it has entrained; however, the plume continues to rise relative to the ambient air, and the resulting vertical velocity shear continues to produce turbulence and entrainment. Measurements of the mean velocity distribution in a cross section of a bent-over plume show the plume to be a double vortex, as shown in Fig. 2.12. Naturally the greatest vertical velocity and buoyancy occur near the center of the plume, where the least mixing takes place. As the gases encounter ambient air above the plume, vigorous mixing occurs all across the top of the plume. This mixing causes the plume diameter to grow approximately linearly with height as it rises.

If the plume is hot or is of lower mean molecular weight than air, it is less dense than air and is therefore buoyant. If the heat is not lost and the atmosphere is well mixed, the total buoyant force in a given segment of the moving plume remains constant. This causes the total vertical momentum of that segment to increase at a constant rate, although its vertical velocity may decrease owing to dilution of the momentum through entrainment. At some point downwind of the stack, the turbulence and vertical temperature gradient of the atmosphere begin to affect plume rise significantly. If the atmosphere is well mixed because of vigorous turbulent mixing, it is said to be neutral or adiabatic. In such an atmosphere the temperature decreases at the rate of 9.8 ^{o}C per 1 km. This rate of decrease, which is called the adiabatic lapse rate (Γ), is the rate at which air lifted adiabatically cools owing to expansion as the ambient atmospheric pressure decreases. If the temperature lapse of the atmosphere is less than the adiabatic lapse rate, the air is said to be stable or stably stratified. Air lifted adiabatically in such an environment becomes cooler than the surrounding air and thus tends to sink back. If the temperature actually increases with height, the air is quite stable. Such a layer of air is called an inversion. If the temperature lapse of the atmosphere is greater than the adiabatic lapse rate, the air is said to be unstable or unstably stratified. Air lifted adiabatically in such an environment becomes warmer than the surrounding air, and thus all vertical motions tend to amplify.

Fig. 2.12 Cross section of mean velocity distribution in a bent-over plume (Briggs, 1969).

The potential temperature (θ) is defined as the temperature that a sample of air would acquire if it were compressed adiabatically to some standard pressure (usually 1000 millibars), The potential temperature is a convenient measure of atmospheric stability since:

$$\frac{\delta\theta}{\delta z} = \frac{\delta T}{\delta z} + \Gamma \qquad (2.1)$$

where $\Gamma = 9.8\ ^{o}C/km$.

Thus, the potential temperature gradient is positive for stable air, zero for neutral air, and negative for unstable air.

If the ambient air is stable, i.e., if $\delta\theta/\delta z>0$, the buoyancy of the plume decays as it rises since the plume entrains air from below and carries it upward into regions of warmer ambient air. If the air is stable throughout the layer of plume rise, the plume eventually becomes negatively buoyant and settles back to a height where it has zero buoyancy relative to the ambient air. The plume may maintain this height for a distance of 32,187 m or more from the source. In stable air atmospheric turbulence is suppressed and has little effect on plume rise.

If the atmosphere is neutral, i.e., if $\delta\theta/\delta z=0$, the buoyancy of the plume remains constant in a given segment of the plume provided the buoyancy is a conservative property. This assumes no significant radiation or absorption of heat by the plume or loss of heavy particles. Since a neutral atmosphere usually comes about through vigorous mechanical mixing, a neutral atmosphere is normally turbulent. Atmospheric turbulence then increases the rate of entrainment; i.e., it helps dilute the buoyancy and vertical momentum of the plume through mixing.

If the atmosphere is unstable, i.e., if $\delta\theta/\delta z<0$, the buoyancy of the plume grows as it rises. Increased entrainment due to convective turbulence may counteract this somewhat, but the net effect on plume rise is not well known. The few usable data for unstable situations seem to indicate slightly higher plume rise than in comparable neutral situations. On warm, unstable afternoons with light wind, plumes from large sources rise thousands of feet and even initiate cumulus clouds.

Measurements are made difficult by fluctuations in plume rise induced by unsteady atmospheric conditions. On very unstable days there are large vertical velocity fluctuations due to convective eddies that may cause a plume to loop, as shown in Fig. 2.14 (d). Fig. 2.13 illustrates the large variations in plume rise at a fixed distance downwind during unstable conditions. On neutral, windy days the plume trajectory at any one moment appears more regular, but there still may be large fluctuations in plume rise due to lulls and peaks in the horizontal wind speed. Since the wind is responsible for the horizontal stretching of plume buoyancy and momentum, the wind strongly affects plume rise. In stable conditions there is very little turbulence, and plume rise is also less sensitive to wind-speed fluctuations. This can be seen in Fig. 2.13. In this case the plume leveled off in stable air, and its rise increased in a smooth fashion as the air became less and less stable owing to insolation at the ground. One might ask whether plume rise is affected by the addition of latent heat that would occur if any

water vapor in the stack gases were to condense. This is an important question because there may be as much latent heat as there is sensible heat present in a plume from a conventional power plant. It is true that some water vapor may condense as the plume entrains cooler air, but calculations show that in most conditions the plume quickly entrains enough air to cause the water to evaporate again. Exceptions occur on very cold days, when the air has very little capacity for water vapor, and in layers of air nearly saturated with water vapor, as when the plume rises through fog.

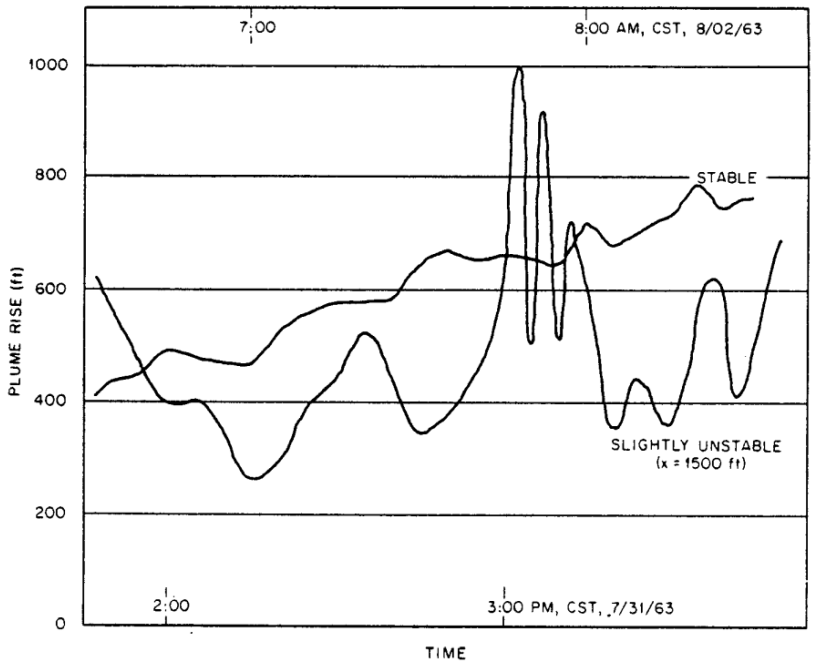

Fig. 2.13 Fluctuations of plume rise with time (Gallatin Plant, Tennessee Valley Authority) (Briggs, 1969).

2.1.4.3 Diffusion of smoke

On a clear night the ground radiates heat, most of which passes out into space. In this process the air near the ground is cooled, and an inversion is formed. The stable layer may be several thousand feet deep; so, most plumes rising through it lose all their buoyancy and level off. This behavior is called fanning and is pictured in Fig. 2.14 (a). When the sun comes up, convective eddies develop and penetrate higher and higher as the ground warms up. As the eddies reach the height at which the plume has leveled off, they rapidly mix the smoke toward the ground while the inversion aloft prevents upward diffusion. This phenomenon, called

fumigation, can bring heavy concentrations of effluent to the ground (Fig. 2.14 (b)). Just after an inversion has been broken down by convective eddies or in cloudy, windy conditions, the atmosphere is well mixed and nearly neutral. Then the plume rises and diffuses in a smooth fashion known as coning (Fig. 2.14 (c)). As the heating of the ground intensifies, large convective eddies may develop and twist and fragment the plume in a looping manner (Fig. 2.14 (d)). Diffusion is then more rapid than in a neutral atmosphere. The convection dies out as the sun gets lower, and an inversion again starts to build from the ground up. This ground inversion is weak enough at first that the plume can penetrate it, and the plume diffuses upward but is prevented by the stability below from diffusing downward. This lofting period (Fig. 2.14 (e)) is the most ideal time to release harmful effluents since they are then least likely to reach ground.

The meteorological conditions that should be considered in stack design depend on the size of the source, the climatology of the region, and the topography. In reasonably flat terrain, high wind with neutral stratification usually causes the highest ground concentrations since there is the least plume rise in these conditions. The mean concentration of the effluent in the plume is reasonably well described by a Gaussian distribution which the detail is added in the appendix A, for which the ground concentration is given by

$$C = \frac{Q_v}{2\pi\sigma_y\sigma_z U_0} \exp\frac{-z^2}{2\sigma_z^2}\left\{\exp\left(-\frac{(H-y)^2}{2\sigma_y^2}\right) + \exp\left(-\frac{(H+y)^2}{2\sigma_y^2}\right)\right\} \qquad (2.2)$$

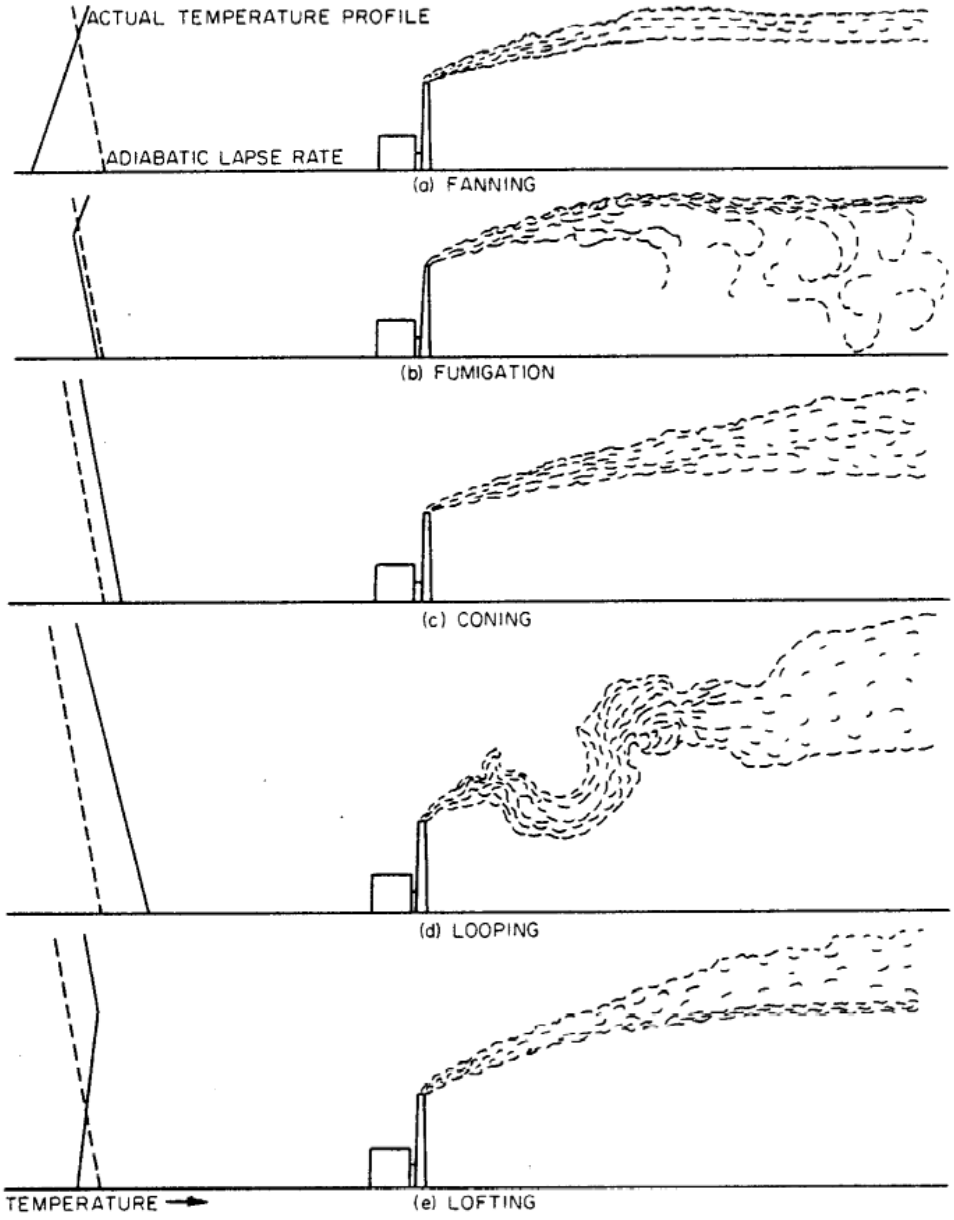

Fig. 2.14 Effect of temperature profile on plume rise and diffusion (Briggs, 1969).

2.1.5 Nondimensional analysis

Basically, dimensional analysis is a method for reducing the number and complexity of experimental variables which affect a given physical phenomenon, by using a sort of compacting technique. Although its purpose is to reduce variables and group them in dimensionless form, dimensional analysis has several side benefits. The first is enormous savings in time and money. A second side benefit of dimensional analysis is that it helps our

thinking and planning for an experiment or theory. It suggests dimensionless ways of writing equations before we waste money on computer time to find solutions. It suggests variables which can be discarded; sometimes dimensional analysis will immediately reject variables, and at other times it groups them off to the side, where a few simple tests will show them to be unimportant. Finally, dimensional analysis will often give a great deal of insight into the form of the physical relationship we are trying to study. A third benefit is that dimensional analysis provides scaling laws which can convert data from a cheap, small model to design information for an expensive, large prototype. We do not build a million-dollar airplane and see whether it has enough lift force. We measure the lift on a small model and use a scaling law to predict the lift on the full-scale prototype airplane. There are rules we shall explain for finding scaling laws. When the scaling law is valid, we say that a condition of similarity exists between the model and the prototype (White, 2003).

2.1.5.1 The Pi theorem

There are several methods of reducing a number of dimensional variables into a smaller number of dimensionless groups. The scheme given here was proposed in 1914 by Buckingham and is now called the "Buckingham Pi Theorem". The name pi comes from the mathematical notation Π, meaning a product of variables. The dimensionless groups found from the theorem are power products denoted by Π_1, Π_2, Π_3, etc. The method allows the pi groups to be found in sequential order without resorting to free exponents.

The first part of the pi theorem explains what reduction in variables to expect: if a physical process satisfies the PDH and involves *n* dimensional variables, it can be reduced to a relation between only *k* dimensionless variables or Πs. The reduction $j = n - k$ equals the maximum number of variables which do not form a pi among themselves and is always less than or equal to the number of dimensions describing the variables.

The second part of the theorem shows how to find the pi one at a time: find the reduction *j*, then select *j* scaling variables which do not form a pi among themselves. Each desired pi group will be a power product of these *j* variables plus one additional variable which is assigned any convenient nonzero exponent. Each pi group thus found is independent (White, 2003).

2.1.5.2 Reynolds Number, *Re*

The Reynolds number (*Re*) which is the basis of much physical modelling is now universally employed in the correlation of experimental data on frictional pressure drop and heat and mass transfer in convective flow. It is employed to characterize when the viscous flowing fluid changes its flow-regime to transition between the laminar and turbulent. It is always important and this number cannot be ignored if flow regions of high-velocity gradients are considered. Confined or unconfined flow can be characterized by this number, but it becomes insignificant at which the regions are far away from solid surfaces, jets, or wakes. The Reynolds number, *Re*, characterizes the relative importance of the momentum transport by convection (ρU^2) and by viscous diffusion ($\mu U/L$) (Reynolds, 1883). In general terms, it is defined as

$$\frac{convective\ flux\ of\ momentum}{diffusive\ flux\ of\ momentum} \approx \frac{\rho U^2}{\mu \frac{U}{L}} = \frac{UL}{v} = Re \tag{2.3}$$

Alternatively, another way given Reynolds number (*Re*), it can also consider as the ratio between the characteristic transport times by diffusion and convection along distances of order of magnitude L. Since v represents the diffusivity of momentum of order L^2/v and the characteristic time for convection is then of order L/U which presents the time for covering the distance L at the average velocity U of the flow. Considering altogether, we can find the ratio of the characteristic times as

$$\frac{characteristic\ diffusion}{characteristic\ convection} \approx \frac{\frac{L^2}{v}}{\frac{L}{U}} = \frac{UL}{v} = Re \tag{2.4}$$

where $v = \mu/\rho$, v is kinematic viscosity, ρ fluid density, μ fluid viscosity, U is fluid velocity and L the characteristic length (Guyon et al., 2017).

2.1.5.3 Froude Number, *Fr*

Froude number (*Fr*) becomes significant when we are dealing with free surface flow. This dimensionless number is an important value in flow analysis to which the flow is exposed

to the Earth's atmosphere. Physical meaning of interpretation can be done in the same way as Reynolds number. Generally, we start to first square it and then multiply it by the density and the area of flowing fluid ($\rho AVV/\rho AL$g). Through the order of magnitude analysis, we can interpret as the value of the inertia against the weight of fluid itself. However, due to the formation of characteristic scale for measuring the gravitational force, it is found that the gravity should be measured by values of V^2/L, so that gL/V^2 shall be utilized to represent the value of Froude number. In terms of historical reasons, however, it is preferable to measure the square root of the inverse value itself ($V/\sqrt{gL}$) and it should be interpreted that the gravity makes fluid attach to the Earth' surface. In case of value of the characteristic gravity looks too small (Froude number becomes high value) the surface of the flowing fluid that is open to the atmosphere might jump, e.g., appearing the hydraulic jump. The inertia can overcome the gravity influence (Chitsomboon, 2001).

$$\frac{inertial\ force}{gravitational\ force} \approx \frac{V}{\sqrt{gL}} = Fr \tag{2.5}$$

$$Fr = \frac{F_i}{F_g} = \frac{\rho L^2 V^2}{\rho g L^3} = \frac{V^2}{gL} \tag{2.6}$$

Where F_i and F_g are defined as the inertial and gravitational forces, respectively (Somchai and Kaewnai, 2014). The system of which the gravity and inertia play an important role predominating over, the phenomena shall be driven by frictional and gravitational forces. We need to logically judge whether the frictional force or gravitational force shall be selected (Cengel and Cimbala, 2006).

2.2 Literature review

2.2.1 Smoke dispersions

To date, there have been rich past researches (Roman and Ramachandran, 2010; Leelossy et al., 2014; Taylor, 1959; Gifford, 1959; Brusca et at., 2015; Baouabe et al., 2011; New et al., 2006; Gupta et al., 2012; Said et al., 2005; Huang and Hsieh, 2002; Majeski et al., 2010; Huber and Snyder, 1976) studied on smoke dispersion from a chimney using a wind tunnel. The extensive results of these wind tunnel experiment have been presented and compared with theory, field measurement, and numerical simulation results. Several theoretical

researches have been carried out on smoke dispersion. However, most of them lacked experimental data comparison (Leelossy et al., 2014; Taylor, 1959; Gifford, 1959).

Brusca et al. (2015) investigated the interaction of a continuous plume released from a point source with various obstacles, based on a laboratory work. They used digital image analysis to investigate the downwind influence of obstacles of various shapes and distances from a smoke dispersion source in terms of the aerosol concentrations at several points. It was conduced the analysis of variance and the results highlighted especially how the vortexes on the bottom of the obstacles amplified the concentration of aerosol particles beyond the obstacles. It was then determined the necessary distance from the source to obstacles so as the PM_{10} could decrease. The image analysis procedure allowed to visualize the profile of the plume when there were or not obstacles as shown in Fig. 2.15. Also, by this analysis it was highlighted how the plume without obstacles reached higher peaks. For future work it is under analysis the idea to use image processing to better define the plume shape and above all to define inversion layers and their relationship with obstacles. It is also under analysis the idea to use image processing to associate aerosol particles concentrations with pixel densities.

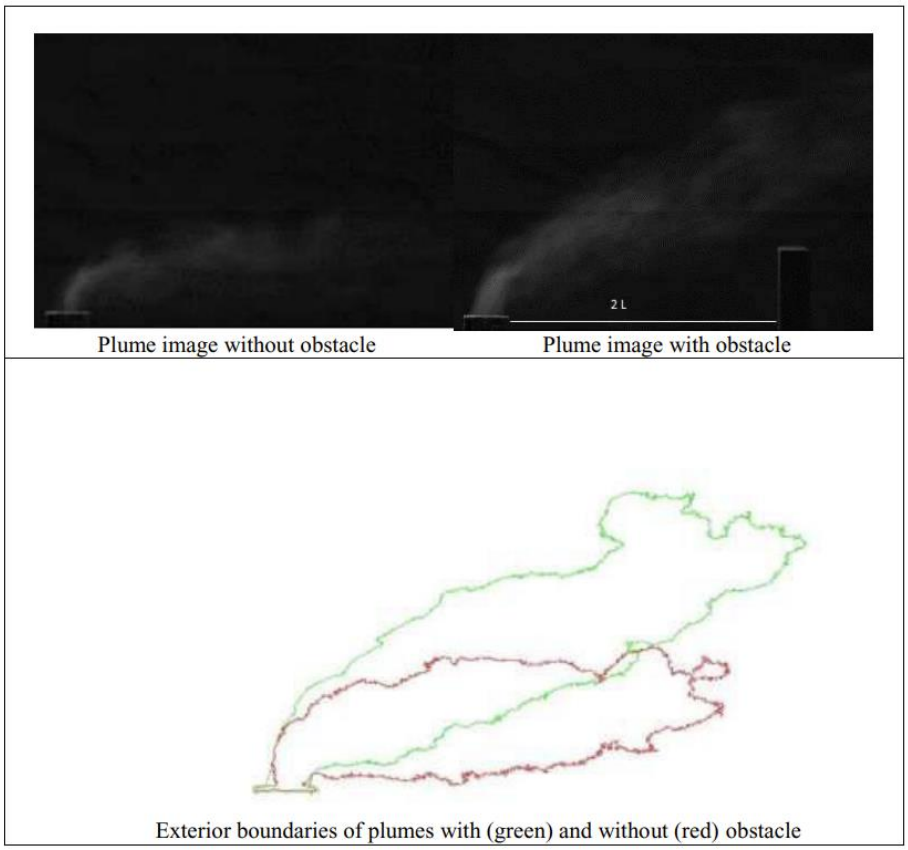

Fig. 2.15 Image analysis for the configuration with obstacle with H2 and distance 2L (Brusca et al., 2015)

Baouabe et al. (2011) used particle image velocimetry (PIV) to measure velocity field around a chimney and describe its flow structure. The flow structure and vortex topology were studied under variety of oncoming flow conditions using flow visualization techniques. As shown in Fig. 2.16, two types of chimneys (straight and bent) showed the effect of the geometry of the chimney at inlet velocity of 0.8 m/s and jet ejected of 0.8 m/s. It was shown that just before the obstacle, the flow structure is determined by the chimney configuration. In the case of the straight chimney the plume is subjected to a transverse flow. Complex flow behaviors were the results of the interaction between the downwash effect, which was induced by the cross flow passing over the pipe exit, the up-shear effect induced by the issuing plume, and the wakes behind the plume and the pipe. The emitted plume bends over into the cross flow direction. On the other hand, when the chimney was bent, the obtained flow was similar to a co-flow. The flow followed the direction of the bend; it was horizontal before meeting the obstacle. All these considerations allowed us to characterize well the impact of the injection of the jet emitted from the chimney within the cross flow, and its spreading around the obstacle and within the whole

domain. Such characterization was very important with regard to pollutant dispersion and consequently to the environmental impact. Indeed, the different species contained within the emitted fumes were mainly directed by the velocity components and their mixing and progression within the domain and around the obstacle were closely related.

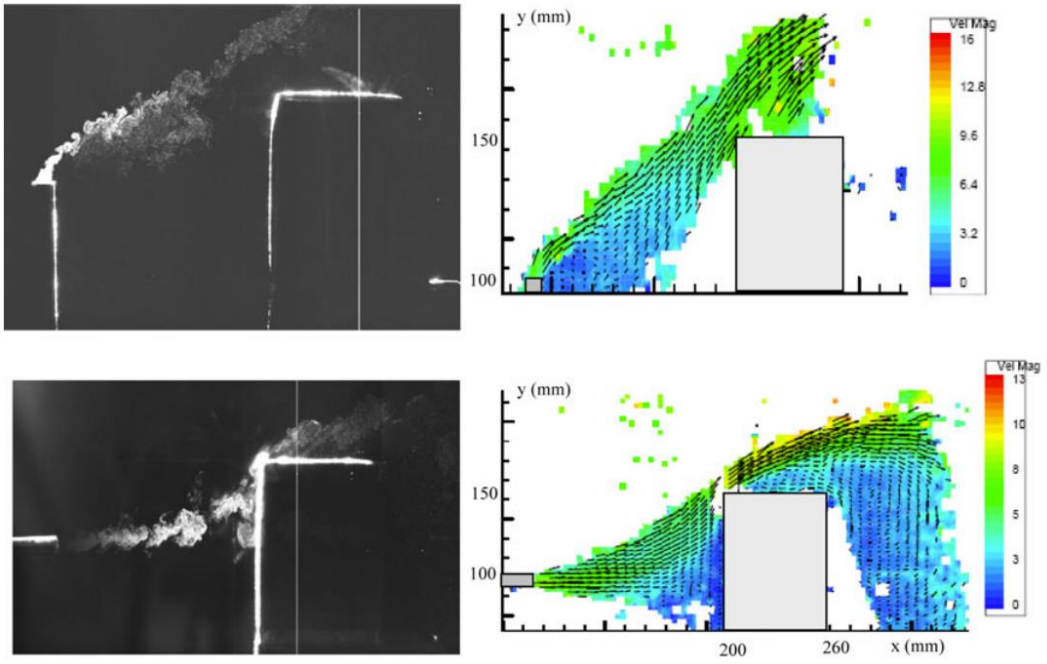

Fig. 2.16 Effect of the geometry of the chimney (Baouabe et al., 2011).

New et al. (2006) experimentally investigated the effects of jet velocity profiles on the flow field of a round jet in a cross flow (JICF). The results obtained for the two jet configurations were shown in Fig. 2.17 for MR=2.3–5.8. For the case of tophat JICF regular formation of leading-edge and lee-side vortices along the jet/cross-flow interfaces can be seen. As the MR was increased, jet penetration into the cross-flow was observed to increase correspondingly. Furthermore, the formation of the large-scale vortices also appeared to intensify, with vortices shed consecutively getting increasingly closer to one another. In contrast, the seeded parabolic JICF jet columns appeared to ‘‘thin’’ gradually as they penetrate further into the cross-flow, with the jet/cross-flow interface remaining stable until approximately the location of maximum deflection. Thereafter, leading-edge and lee-side vortices began to form in a less coherent and sporadic manner, unlike the recursive ‘‘daisy-chain-like’’ formation observed in tophat JICF. The initiation and formation of these vortices were unsteady, both spatially and temporally, except for the highest MR investigated in the

present study (MR=5.8). Moreover, these vortices travelled for shorter streamwise distance before breaking up sporadically into fine-scale structures, and the leading-edge vortices for the parabolic jets appear to be smaller than their tophat jets counterparts. Flow visualization results shown that the thicker shear layers associated with parabolic JICF are able to delay the formation of leading-edge and lee-side vortices than the corresponding tophat JICF, where the shear layers are thinner, and large-scale vortices are formed readily and regularly. As a result, there is an increase in jet penetration and a reduction in the near-field entrainment of cross-flow fluid by a parabolic JICF.

Gupta et al. (2012) investigated the downwash effect of a rooftop structure (RTS) on plume dispersion in wind tunnel experiments. The downwash effect produced by the RTS caused a significant increase in the roof level concentration depending on the building height, stack location, stack height, exhaust speed, wind direction, and RTS cross-wind width. Flow visualization photos obtained with the test buildings with and without an RTS ware presented in Fig. 2.18. The plume was deflected downwards and a significant portion of it made contact with the roof. The downwash effect of the RTS on the plume was clearly evident due to increase in height a large separation bubble was formed on the roof of tall building compared to the low-rise building. In this case, the plume and RTS were completely engulfed by the bubble. Thus, an RTS totally engulfed inside the bubble has little effect on dispersion of exhaust from a rooftop source. An attempt was made to provide design guidance for determining stack height required to avoid the downwash effect for an exhaust placed downwind of the RTS.

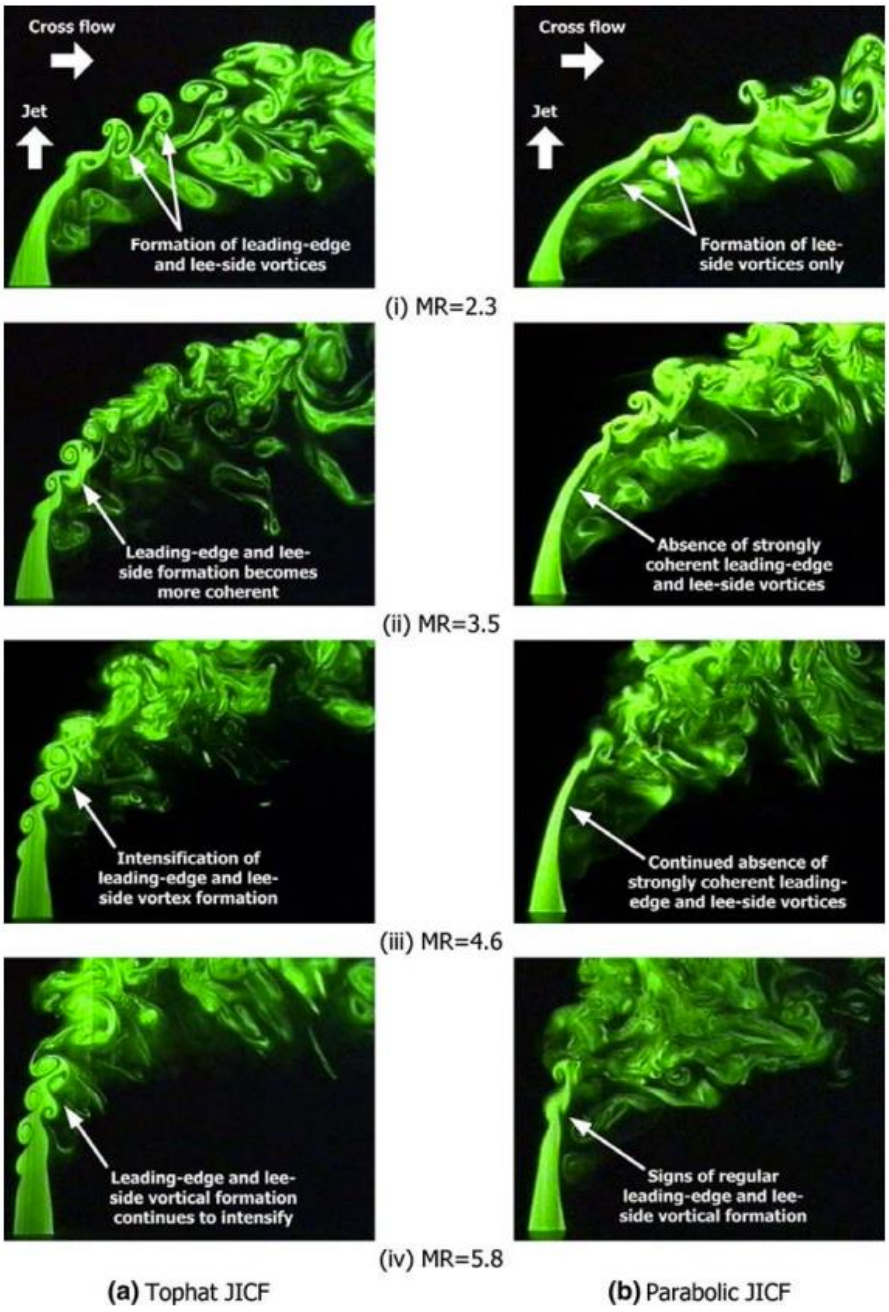

Fig. 2.17 Streamwise laser cross-sections along the symmetry plane of (a) tophat and (b) parabolic jets exhausting transversely into a cross-flow at MR=2.3–5.8 (New et al., 2006).

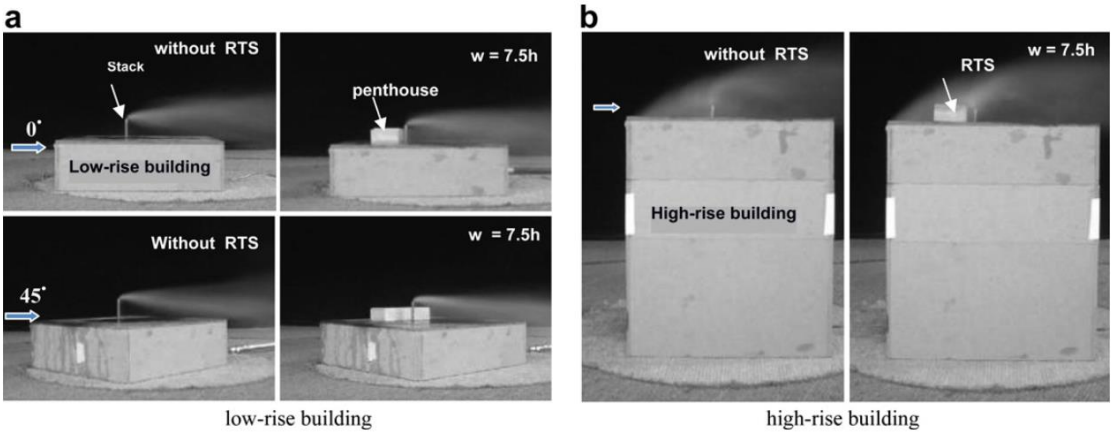

Fig. 2.18 Flow visualization showing the effect of RTS on plume (Gupta et al., 2012).

Said et al. (2005) used PIV to investigate the coherent structures in the near-wake region of a turbulent round-jet ejected perpendicularly from a chimney into a cross flow. They elucidated the Kelvin–Helmholtz vortex structures, downwash phenomena, effect of the height of the chimney and the influence of the wind velocity on the plume released by the chimney. When the velocity of the wind tunnel increased, the plume curves until it became almost horizontal to the ground. When the wind tunnel had a velocity lower than or equal to the plume's velocity, the plume spreads out in the shape of a cone, and this cone tended to bend down more quickly as the velocity of the wind tunnel increased as indicated in the Fig. 2.19. The flow field of a chimney in a crossflow is dominated primarily by the complex interactions between the plume wake, chimney wake, and the downwash effect, which is induced when a crossflow passes over the chimney top. A large plume-to-crossflow velocity ratio as presented in this paper, plays an important role, particularly in the region of the plume wake.

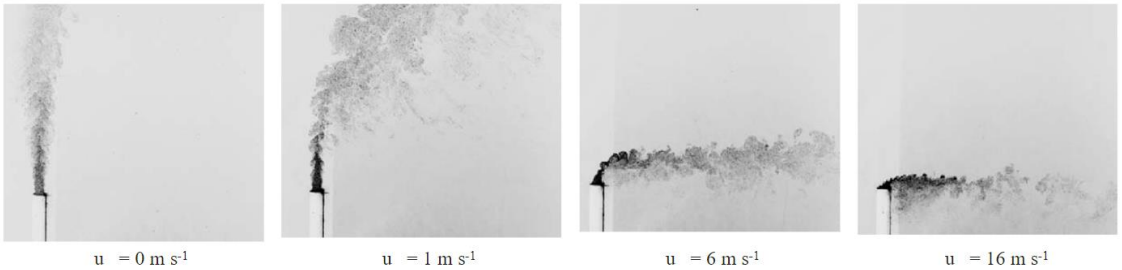

Fig. 2.19 Wind velocity effects (Said et al., 2005).

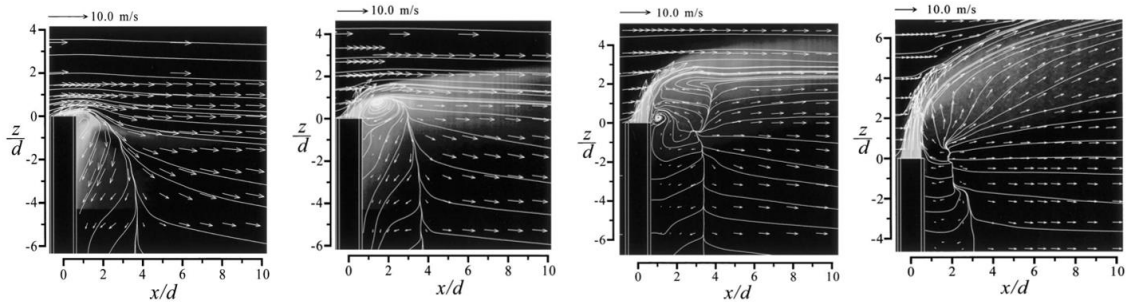

(a) (b) (c) (d)

Fig. 2.20 The jet structure : (a) downwash, (b) cross-wind dominant flow, (c) transitional flow and (d) jet dominant flow (Huang and Hsieh, 2002).

Huang and Hsieh (2002) classified the jet structure based on the momentum ratio between the cross-wind and the jet velocity. Four characteristic types of flows with apparent differences were identified: downwash, cross-wind dominant flow, transitional flow, and jet dominant flow as displayed in Fig. 2.20. Large amount of jet fluids in the downwash and crosswind-dominated flows are entrained down to the tube wake because a clockwise-rotating vortical structure is formed in the near wake due to the combined effects of the jet shear and tube-tip downwash. In the transitional and jet-dominated flows, the up-flows induced by large up-shooting jet velocities overwhelm downwash effect so that most of the jet fluids go downstream rather than to the tube wake. The jet fluids of the transitional and jet-dominated flows thus can transport and disperse to far field. The pollutants issued from the stack should not be entrained into the downwash area in order to avoid high concentration disaster. The design and operation values of the jet-to-crosswind momentum flux ratio must not go below 2. Although the flow features in the symmetry plane were measured and analyzed, the actual quantitative data for mixing and dispersion capability in each flow mode were still unknown. In order to obtain the whole picture of the flows, measurements in the off-symmetry vertical planes and the horizontal planes are needed in the future.

Majeski et al. (2010) proposed a phenomenological model for predicting the size of a low-momentum jet diffusion flame diluted with an inert gas in a cross flow. Huber and Snyder (1976) reported concentration measurements for an elevated point source placed in the lee of a two-dimensional Gaussian model ridge, the height of which was about one-third of the boundary layer thickness. Their results demonstrated the occurrence of significant ground level concentration upwind of the stack source when it was placed at the ridge base within the lower part of the cavity region. Pournazeri et al. (2012) presented a method for scaling the urban

dispersion parameters in water channels and wind tunnel. Their results shown that plume rise associated with relatively low-level buoyant sources in urban areas is highly affected by the complex flows induced by surrounding buildings, an effect which current plume rise models are not able to accurately reproduce.

2.2.2 Downwash patterns

At recent years, many studies have been carried out on pollutant dispersion from the chimney (Baouabe et al., 2011; Brusca et at., 2015; Gifford, 1959; Gupta et al., 2012; Huang and Hsieh, 2002; Huber and Snyder, 1976; Leelossy et al., 2014; Majeski et al., 2010; New et al., 2006; Roman and Ramachandran, 2010; Said et al., 2005; Taylor, 1959). Previous studies had provided valuable contributions to reveal the flow patterns and behaviors, as well as their influence on the smoke dispersion from a chimney by CFD simulation. The pollutant diffusion has been often taken as a hot research area for several years. Said et al. (2005) used PIV to investigate the coherent structures in the near-wake region of a turbulent round-jet ejected perpendicularly from a chimney into a cross flow. They elucidated the Kelvin–Helmholtz vortex structures, downwash phenomena as shown in Fig. 2.21 and Fig. 2.22, respectively. At the exhaust of the chimney, the typical turbulent pattern called Kelvin–Helmholtz instabilities was observed. This phenomenon appeared when the flow is subjected to shearing between two fluids, which slip one over the other at different velocities. This instability leaded to the formation of a ‘‘swirling sheet’’ within the mixing zone between the two fluids. Depending on wind velocity, these patterns turned clockwise or counter-clockwise. In fact, the rotational direction depended on the ratio of velocity factor. This was definitely visible in Fig. 2.21, the value of the velocity ratio being 0.545 and 1.454 for wind velocity of 6 m/s and 16 m/s, respectively. The downwash of the plume in the downstream region of the chimney was presented in Fig. 2.22. When the ratio of velocity was lower than 1.5, the effluents were aspired in the turbulent wake which develops in the downstream region of the chimney.

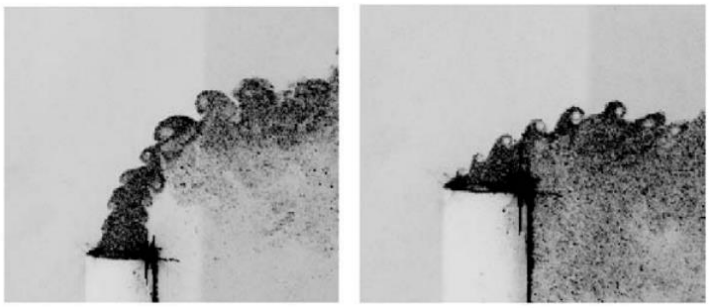

Fig. 2.21 Kelvin–Helmoltz structures (Said et al., 2005).

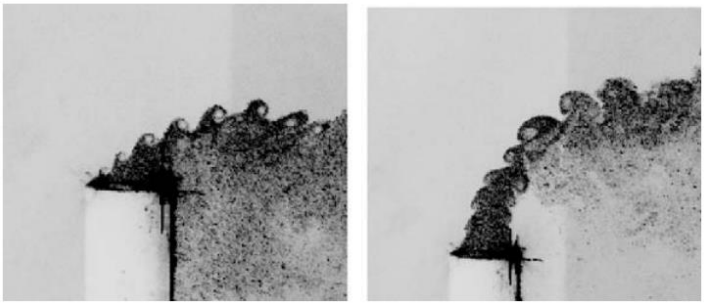

Fig. 2.22 Downwash phenomena (Said et al., 2005).

Gupta et al. (2012) investigated the downwash effect of a rooftop structure (RTS) on plume dispersion. They attempted to provide design guidance for determining stack height required to avoid the downwash effect for an exhaust placed downwind of the RTS. A simple design guidance that may be used to determine the stack height required to avoid RTS downwash effect was indicated in Fig. 2.23 such data for 0^o and 45^o for different momentum ratio (M) values. Fig. 2.23 (a) shown the variation of normalized h_{req} with M for 0^o. The values of h_{req} varied significantly with M and x_s. The h_{req} decreased with an increase in M and x_s. Fig. 2.23 (b) shown similar plots for 45^o. The trends were similar to the normal wind case. However, h_{req} values were generally smaller than those obtained for 0^o. For an oblique wind, the height of the separation bubble formed on the RTS was not significantly affected by an increase in RTS crosswind width. On the other hand, for the normal wind, the height of the separation bubble and length of RTS downwind cavity increased significantly with an increase in RTS crosswind width. Consequently, for 45^o, the plume would be discharged outside the RTS recirculation zone for lower values of h_{req} than for 0^o. This result may be used as preliminary design guidance for determining stack height to avoid downwash due to an RTS. Results indicate that depending upon RTS-stack separation gap and M; the required stack height can vary from h to 3h.

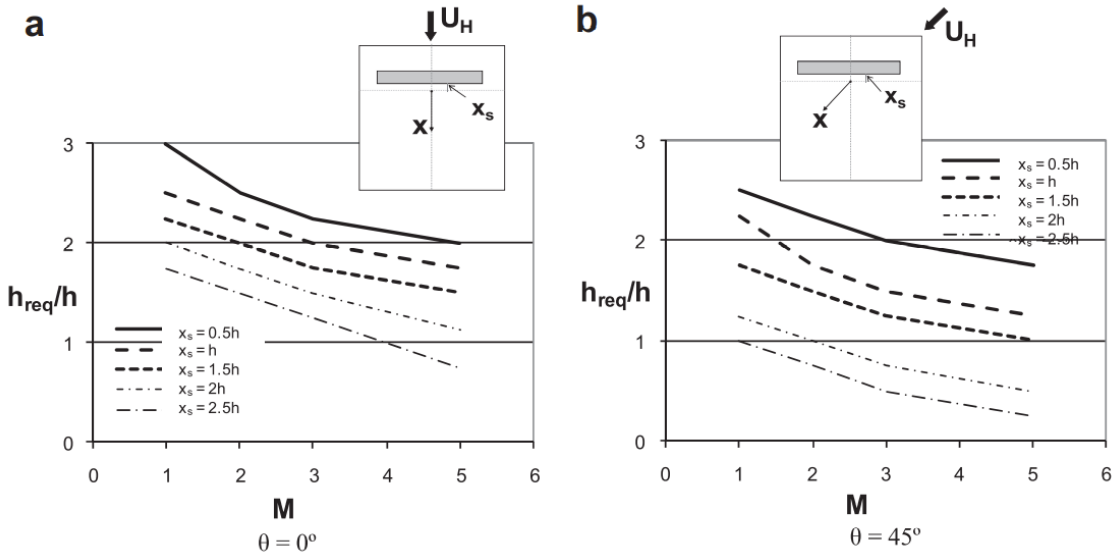

Fig. 2.23 Stack height required to avoid the downwash effect of an RTS for the low-rise building (Gupta et al., 2012).

Overcamp (2001) reviewed scaling criteria for avoiding downwash in subcritical model experiments. Then data from 10 investigators, which update the work of Overcamp (1983), were presented as shown in Table 2.2. These data were compared to a theory proposed by Tatom (1986) for predicting downwash in stack modeling experiments. A comparison was made between data on the occurrence of downwash from ten subcritical model studies to the theory proposed by Tatom (1986). In general, there was good agreement of Tatom's theory with the occurrence of downwash. Downwash was a phenomenon in which the plume from the stack was pulled into the wake of the stack. In the field, downwash could lead to diminished plume rise and higher concentrations downwind.

Table 2.2 Plume rise and downwash studies[a] (Overcamp, 2001).

Investigator	ρ_s/ρ_a	D_{int}, cm	Ambient Fluid	Re_a^{u} [b]
Barilla (1968)	1.40	0.635	Water	NA[c]
Huber et al. (1980)	0.5	1.5–4.09	Air	1750–4300
Manins (1979)	≈ 1.09	1.16	Water	700–1100
Murthy (1970)	0.64–0.69	8.89	Air	11700–15500
Overcamp and Hoult (1971)	1.02–1.1	1.57–2.22	Water	600–3400
Overcamp and Ku (1986)	0.6	2.5	Air	780–1100
Petersen (1978)	0.75	1.21–1.86	Air	150–580
Sherlock and Stalker (1941)	0.62–0.87	8.26	Air	9250
Snyder (1974)–Freon-12	4.18	NA	Air	NA
Snyder (1974)–Helium	0.138	NA	Air	NA
Wright (1977)	1.05–1.13	0.8–1.0	Water	470–1300

[a] The data indicated represent only experiments considered in this paper.
[b] Estimated using the internal stack radius with assumption that the water was at 20°C and air was at 25°C with an adjustment for atmospheric pressure based on the US standard atmosphere for the altitude of the experiments.
[c] Not available.

Canepa (2004) presented an overview of the existing literature about downwash effects in order to allow the reader to perform a quick survey of the state of the art of the study of the downwash phenomena of air borne pollutants. Recent and less recent studied concerning both building and stack downwash were presented. Some of the presented models were well established and implemented in regulatory air pollutions codes, while other one's were more sophisticated and still under development. In the last few years, efforts have been made to try to describe the downwash effect on pollutant dispersion, which was dangerous because it could cause a high concentration of harmful effluents at ground level. Despite these efforts, at the moment, in regulatory air pollution models, only 'traditional' downwash methods were implemented. Therefore, regulatory models were able to deal with more or less simplified situation only (e.g., schematic buildings and emission configurations). Moreover, different methods gave different results in principle, the method which has the best scientific basis should be preferred, but in practice, another method could be more suitable for a certain case; therefore, it was not possible to state a general rule.

Huang and Hsieh (2002) presented the multiple-mode characteristics of the flow structures and turbulence properties in the near-wake region of the elevated jets in a crosswind obtained by the flow visualization and Laser Doppler Velocimeter (LDV) measurement techniques. They classified the jet structure such as downwash, cross-wind dominant flow, transitional flow, and jet dominant flow. At jet-to-crosswind momentum flux ratio R=0.10, as shown in Fig. 2.24, the jet momentum was not large enough to sustain the impingement and the shear of the transverse stream so that it was deflected through a large angle from the vertical axis of the tube. Most of the smoke particles (the blue images) emitted from the tube were entrained into the tube wake. A little portion of the jet fluids went downstream. At this small R the downwash effect induced by the crosswind across the tube-tip was much larger than the up-shear effect of the jet, so that the velocity vectors in the tube wake display downward components. The downwash area was enclosed in a dividing streamline, which separated the reverse and forward flows in the tube wake. This dividing streamline substantially described the stagnation locations of the recirculation bubble behind the tube. Flows at R less than about 0.9 had the smoke and streamline patterns similar to Fig. 2.24. It was termed the downwash flow. The detailed flow properties of the jet-in-crosswind shown multiple flow modes. Flow structures varied significantly in different flow regimes. Practical used has to consider the characteristics of different flow modes. Although the flow features in the symmetry plane were

measured and analyzed, the actual quantitative data for mixing and dispersion capability in each flow mode were still unknown.

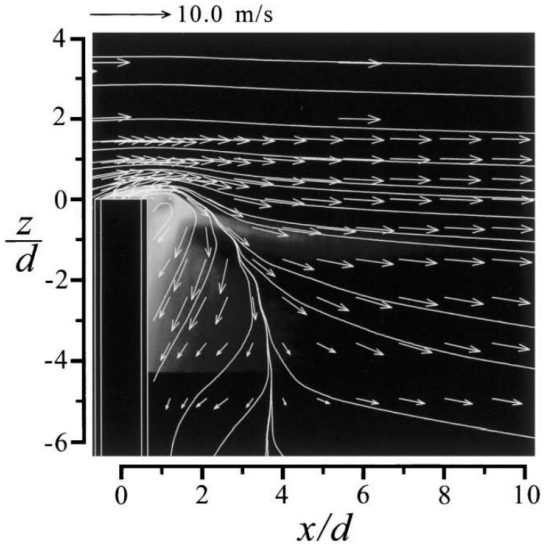

Fig. 2.24 Smoke patterns, velocity vectors, and streamlines of downwash flow in symmetry plane, R=0.10. Exposure time of smoke images: 1/100 s (Huang and Hsieh, 2002).

Gnatowska (2015) presented the results of a complex research program aimed at understanding the character of the flow field around groups of buildings in urban areas and the unsteady phenomena resulting from the character of the wind or from the interference of the wake flow connected with the vortex shedding process as shown in Fig. 2.25. Wind comfort in built-up areas may be affected by a large range of parameters, mainly by wind velocity around building and adequate air quality. Those criteria were often in contradiction, because ensuring proper air quality requires adequate ventilation of built-up areas. Its effectiveness depended on wind direction, building configuration, and location of emission sources as indicated in Fig. 2.25. The performed experimental and numerical research were aimed primarily at the development of the existing knowledge of the interaction between objects located on the ground and its influence on pollutant dispersion. Such studies may contribute to the better understanding of physical processes and provide necessary information for the development of numerical modeling. The results shown that the appropriate location of buildings and the emission sources was very important, especially when considering human health and wind comfort. The choice of emission source shape and size may positively influence pollutant dispersion emitted in building environments and in turn may lead to improved air quality at the pedestrian level.

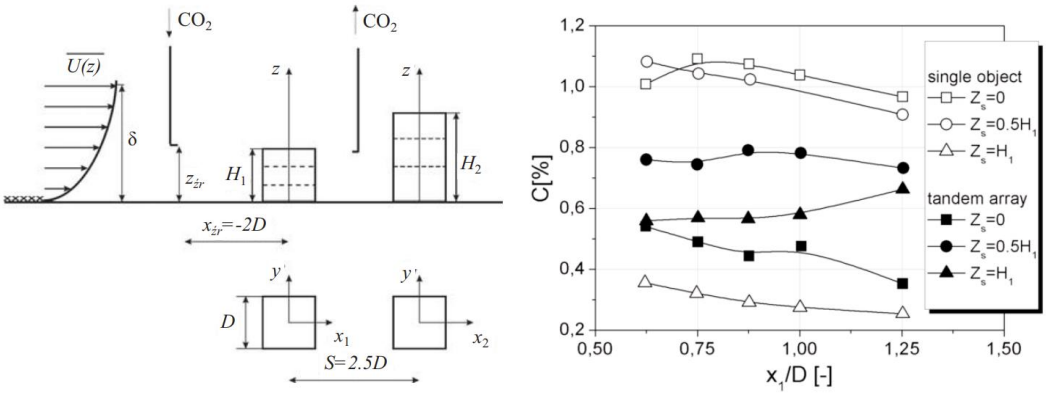

(a) (b)

Fig. 2.25 (a) Schematic presentation of the set-up and nomenclature; and (b) Ground-level centerline concentrations for different heights of emission source (Gnatowska, 2015).

Sekishita et al. (2019) aimed to investigate the patterns of smoke dispersion from a chimney and its occurrence conditions in quasi-isotropic turbulence generated by an atmospheric wind tunnel with an active turbulence generator. They succeeded in the realization of the meandering smoke dispersion (shown in the Fig. 2.26) which can be observed in an actual atmospheric boundary layer. This meandering smoke dispersion was realized in the large-scale turbulence (quasi-isotropic turbulence) generated by the atmospheric wind tunnel with the active grid. The structures of the smoke dispersion were divided into the six modes.

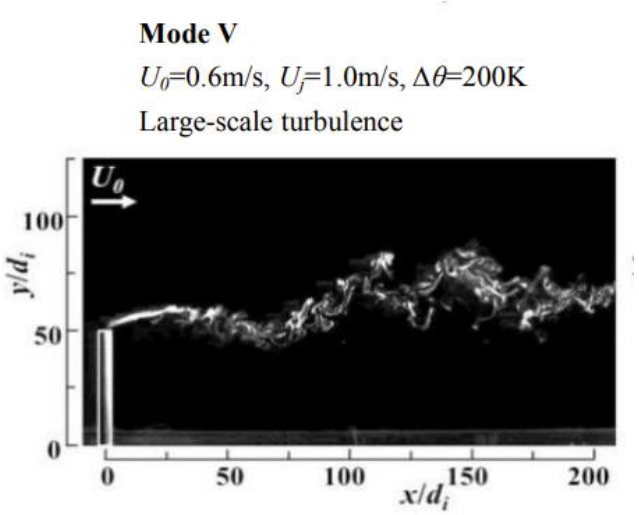

Fig. 2.26 The meandering smoke diffusion (Sekishita et al., 2019).

CHAPTER 3
EXPERIMENTAL AND NUMERICAL METHODOLOGIES

Based on wind tunnel experimental investigation in a systematic manner is selected to gain the insight physics to understand the effect of imposed turbulent character into the observed smoke dispersion patterns, the results using an active turbulence grid (to promote quasi-isotropic turbulence) and a rectangular grid (to generate grid turbulence) are compared to reveal the impact of using active turbulence grid device on this subject. Note that two turbulent conditions are referred from previous work by Makita (Makita, 1991) for the quasi-isotropic turbulence case and by Kistler and Vrebalovich (Kistler and Vrebalovich, 1966) and Makita (Makita, 1991) for the grid turbulence case.

In addition, to have an in-depth understanding of the flow pattern and dispersion of the smoke ejected from the chimney, the computational fluid dynamics (CFD) simulation enables to investigate on the flow structures in a precise manner. The interpretation of the phenomena has been further made with the numerical approach to gain more detailed physics with the insightful understanding from scientific way. The numerical simulation (FDS: Fire Dynamics Simulator), version 6.7.7, (free and open-source software provided by the National Institute of Standards and Technology (NIST) of the United States Department of Commerce), is responsible for the time-dependent of Large Eddy Simulation (LES) method.

3.1 Laboratory experiments

3.1.1 Wind tunnel

Figure 3.1 shows a blowing-type atmospheric wind tunnel employed in this study. It has a test section with the dimensions of 0.7×0.7 m^2 in cross section and 6 m in length. For generating turbulence in the wind tunnel, two turbulence generators are conducted which an active turbulence generator to generate quasi-isotropic turbulence and a rectangular grid to generate grid turbulence as shown in the Fig. 3.2. The active turbulence generator (Makita, 1991), as shown in Fig. 3.2(a), was installed upstream of the test section. The turbulence generator could generate quasi-isotropic turbulence with a high turbulence Reynolds number of R_L, R_λ , defined by the characteristic velocity and the integral scale or the microscale, about 9100 and 390, respectively, at a mean velocity in the cross-wind of U_0 = 5 m/s as shown in the

Table 3.1. That is, a large integral scale, large turbulence fluctuations, and a wide inertial subrange in the energy spectra of velocity fluctuations were achieved, as shown in Fig. 3.3. The inertial subrange, obeying Kolmogorov's famous -5/3 power law, spread for more than two orders of magnitude in wavenumber in the spectrum. These features correspond with those of the grid turbulence with $Re_M \approx 10^6$ realized in a large wind tunnel. The active turbulence grid (quasi-isotropic turbulence) generator is homogeneous and quasi-isotropic, having large turbulence intensity, u_{rms}/U_0, of more than 16% and a large longitudinal integral scale, L_{UX}, of about 200 mm. Note that this active turbulence grid (quasi-isotropic turbulence) generator could attained at satisfactorily realistic turbulence characteristics in the natural of the actual large-scale turbulence fields (Makita, 1991). The conventional rectangular grid (grid turbulence), as shown in Fig. 3.2(b), was positioned in place of the active turbulence generator to generate grid turbulence for comparison purpose. The grid turbulence has Reynolds number, Re_M, about 17×10^3, having turbulence intensity, u_{rms}/U_0, about 1.11%, at a mean velocity in the cross-wind of U_0 = 5 m/s, which is preliminary evaluated referred from previous research by Comte-Bellot and Corrsin (1966, 1971). This is closed to the results present by Makita (1991) in the case of non-quasi-isotropic turbulence (grid turbulence). In addition, from a physical point of views, the comparison of the turbulence characteristics is shown in Table 3.1. The characteristic scale of the turbulence field is represented by the turbulence Reynolds number, R_L or R_λ, defined by the characteristic velocity and the integral scale or the microscale, respectively. As shown in Table 3.1, the quasi-isotropic turbulence gives quite large values of R_L and R_λ. They almost approach to the values of the grid turbulence in the large pressurized wind tunnel with $R_M = 2.4\times10^6$ given by Kistler and Vrebalovich (1966) in spite of $R_M = 15.6\times10^3$ for the quasi-isotropic turbulence. Note that the active turbulence grid is a kind of active bi-plane grid composed of l5 vertical and horizontal oscillating rods with many agitator wings. When the wings stand still, the generator acts as a usual static grid (non-quasi-isotropic turbulence). Each rod is driven by a stepping motor on the outside of the wall as shown in Fig. 3.4. The oscillating mode of the motor is regulated by feeding two kinds of electric pulses to each motor's driver circuit; a drive pulse regulates the rotating speed of the motors while a turn pulse changes the rotating direction. The wake of the rods and the flow separation at the leading or trailing edge of the wings also produced turbulence. The present turbulence field is endowed from its birth with various spectral components of large amplitude which helped it to attain a fully developed and self-conservative state rapidly. The resultant turbulence is called the quasi-isotropic turbulence.

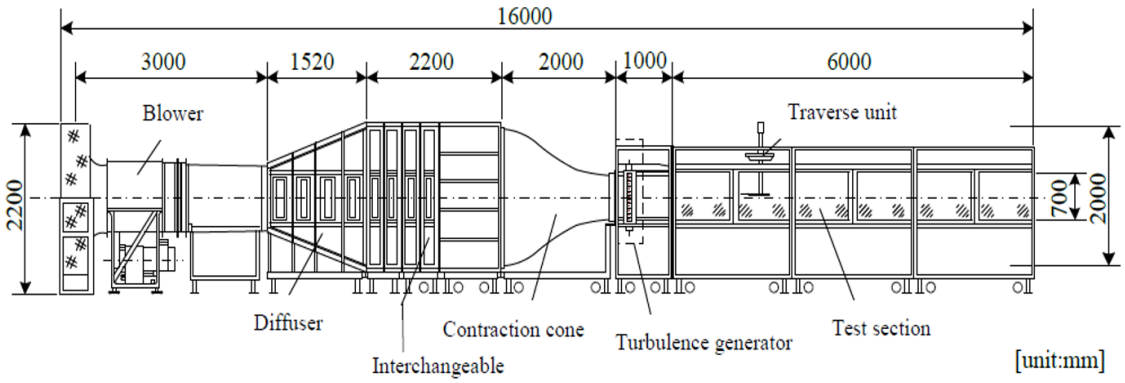

Fig. 3.1 Atmospheric wind tunnel (Makita, 1991).

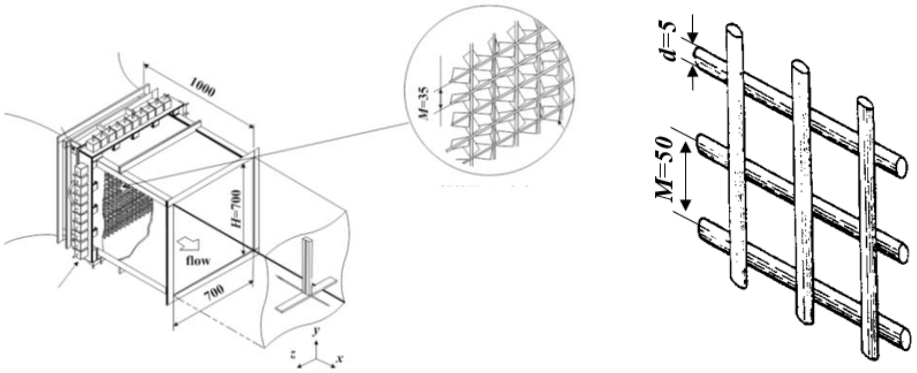

(a) active turbulence grid (Makita, 1991) b) rectangular grid

Fig. 3.2 Turbulence generators (unit: mm).

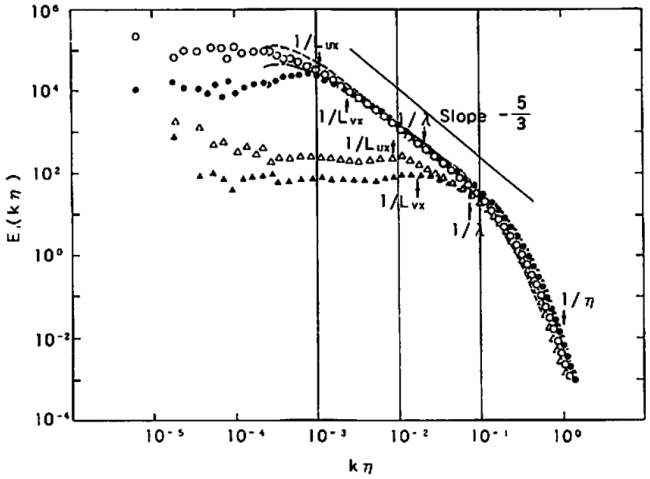

Fig. 3.3 One-dimensional energy spectra at x/M=50, E_1(u-spectrum): (○) quasi-isotropic turbulence, (△) non- quasi-isotropic turbulence, (－－－) grid turbulence (Kistler and Vrebalovich (1966)), E_2(v-spectrum): (●) quasi-isotropic turbulence, (▲) non-quasi-isotropic turbulence, (-·-·-) grid turbulence (Kistler and Vrebalovich (1966)) (Makita, 1991).

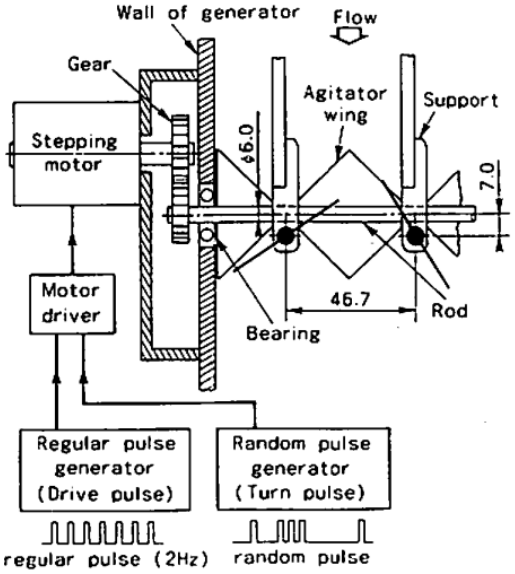

Fig. 3.4 Details of turbulence generator and control system (unit: mm) (Makita, 1991).

Table 3.1 Comparison of the turbulence characteristics (Makita,1991).

Experiment	U_0 m/s	M mm	x/M -	R_M (10^3)	u_{rms}/U_0 %	L_{UX} mm	λ_g mm	η mm	R_L -	R_λ -	n -	α -
Makita (1991)												
Quasi-isotropic turbulence	5.0	46.7	50	15.6	16.4	197	8.2	0.21	9126	387	1.43	0.64
Non-quasi-isotropic turbulence	5.0	46.7	50	15.6	1.45	13	5.9	0.65	75.4	28	1.28	-
Grid turbulence												
Comte-Bellot and Corrsin (1966, 1971)	10.0	50.8	42	34.0	2.22	24	4.9	0.29	355	72	1.25	0.41
Kistler and Vrebalovich (1966)	61.0	171.0	45	2400.0	1.97	47.8	2.4	0.047	13300	669	1.0	0.67
Jet grid												
Gad-el-Hak and Corrsin (1974)	4.2	102.0	46	41.8	3.27	134.7	9.45	0.39	2280	160	0.97	-
Vibrated grid												
Ling and Wan (1972)	0.03	64.0	45	0.94	4.24	59.3	26.7	-	75	34	1.35	-
Atmospheric turbulence												
Sheih et al. (1971)	4.3	-	-	-	12.0	-	144.0	1.05	-	4830	-	-

Where λ_g is Taylor microscale, η is Kolmogorov dissipation scale, n is decay rate, α is Kolmogorov's universal constant.

Measurements on turbulence characteristics were made at U_0 = 5 m/s by using constant temperature hot-wire anemometers and an adjustable X-wire probe shown in Fig. 3.5. The anemometer system has an *S/N* ratio of about 72 dB and the frequency response which is flat from dc to more than 20 kHz. The X-wire probe was made of a tungsten wire of 2.5 μm in diameter and its measuring volume was $0.7 \times 0.7 \times 0.2$ mm^3. The probe configuration was adjusted under a microscope ahead of every measurement. After the probe was settled to a traverse unit in the test section, its attack angle was adjusted by a pulley-coil mechanism so that symmetry of a shear stress distribution behind a circular cylinder of 6 mm in diameter was confirmed. The output signals of the anemometers were recorded by a digital data recorder, and then processed by a signal analyzer and a microcomputer. Statistical quantities of the quasi-isotropic turbulence, e.g., turbulence intensity, probability density function, auto-correlation coefficient, scales of turbulence, energy spectrum, and dissipation spectrum were obtained (Makita, 1991).

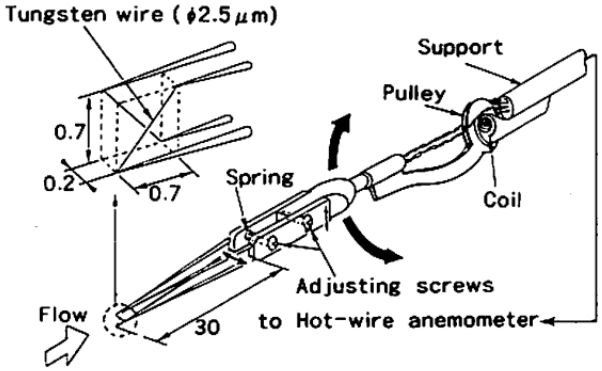

Fig. 3.5 Adjustable X-wire probe (unit: mm) (Makita, 1991).

In addition, Fig. 3.6 (a) and 3.6 (b) compare instantaneous wave traces of the stream wise component of velocity fluctuation, u, in the quasi-isotropic turbulence and the non-quasi-isotropic turbulence (grid turbulence) having the same mesh Reynolds number of R_M = 15.6×10^3. The wave trace of the quasi-isotropic turbulence shows typical random waveform of turbulence fluctuation and any periodic or spiky pattens are not observed in it. As shown by the difference in scale of notation on the vertical axis, the quasi-isotropic turbulence has an amplitude of roughly one order of magnitude larger than that of the non-quasi-isotropic turbulence (grid turbulence). The difference in patten of the wave traces shows that the quasi-isotropic turbulence is richer in low frequency components than the non-quasi-isotropic turbulence (grid turbulence). Fig. 3.6 (c) and 3.6 (d) show the time derivative of the stream wise component of the velocity fluctuation, $\partial u/\partial t$. The derivative signal emphasizes fine-scale turbulent motion. The intermittency of the fine-scale turbulent motion was reported for the first time by Batchelor and Townsend (1949). The waveform of the non-quasi-isotropic turbulence (grid turbulence) does not show a clear intermittent pattern. Kuo and Corrsin (1971) described that the intermittent structure was not clear for the grid turbulence of a low Reynolds number, because the difference in scale is not so large between the fine-scale eddies and the energy-containing eddies uniformly distributed in space. The intermittent pattern becomes notable in the waveform of the quasi-isotropic turbulence. The fine-scale turbulent eddies are known to distribute sparsely in the present quasi-isotropic turbulence (Makita, 1991).

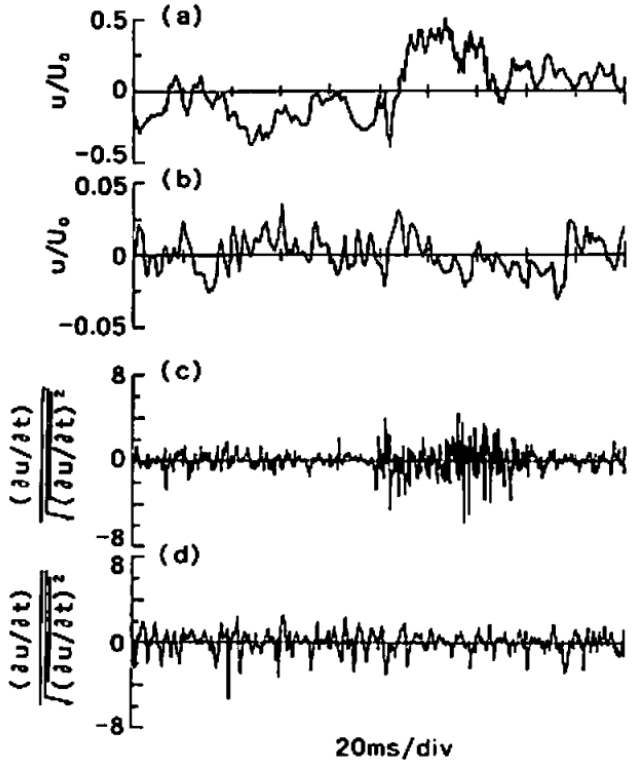

Fig. 3.6 Wave traces of turbulence fluctuation and velocity derivative at *x/M*=50; u: (a) quasi-isotropic turbulence, (b) non-quasi-isotropic turbulence; $\partial u/\partial t$: (c) quasi-isotropic turbulence, (d) non-quasi-isotropic turbulence (Makita, 1991).

3.1.2 Chimney model, smoke generation system, and experimental conditions.

The chimney model of d_i = 4 mm in inside diameter, d_o = 20 mm in outside diameter and h = 200 mm in height was placed on the floor of the wind tunnel test section as shown in Fig. 3.7. The distance between the turbulence generator and the chimney, L, was 3150 mm in the quasi-isotropic turbulence and 2900 mm in the grid turbulence. Slight difference in L for two turbulent cases is simply the wind tunnel design problem and nothing serious in the result (nearly the same turbulent character shall be obtained). The smoke generation system for ejecting heated or unheated air with the smoke from the chimney was composed of an air compressor, an air dryer, an air regulator, a flow meter, a smoke generator which was to smoke by using Shell Ondina Oil 15, a surge tank, a heater for generating the buoyancy jet, and the chimney as shown in Fig. 3.7. The origin of a coordinate system was the center of the chimney on the floor in the wind tunnel test section. The cross-wind direction was x, the vertical direction which is the direction of the jet velocity at the chimney exit was y, and the span-wise direction was z. The cross-sectional average velocity of the jet at the chimney exit was

controlled by the air regulator. The patterns of the smoke dispersion were visualized by the high-speed camera (Photron, FASTCAM SA3 model, 1000 frame/s) and a halogen light. Note that this study only deals with these physical principles of motion and dispersion of smoke released from the chimney. Possible chemical reactions in the atmosphere are not covered.

The present experiments were carried out in the experimental conditions of temperature difference between the cross-wind and the jet from the chimney, $\Delta\theta$, the jet velocity at the top of the chimney, U_j , and the mean velocity of the cross-wind, U_0 , at ambient temperature as shown in table 3.2. That is, the velocity ratio between the jet velocity and the cross-wind velocity, r, was from 0.5 to 4.7, its momentum ratio, R, was from 0.145 to 21.8 and the density ratio between the heated jet and the cross-wind, S, was 0.59, 0.74, 1.00. The mean velocity of the cross flow at the entrance of the test section was measured with a hot-wire anemometer. The vertical mean-velocity profile of the cross flow was uniform around the chimney exit as shown in Fig. 3.8 in the quasi-isotropic turbulence case. Turbulence intensity, u_{rms}/U_0, was from 9.5% to 11.0% in the quasi-isotropic turbulence and from 2.9% to 3.5% in the grid turbulence.

The smoke concentration distribution was evaluated from smoke visualization images taken by the high-speed camera. By superposing 500 instantaneous images, shown in Fig. 3.9, the time averaged brightness intensity distribution was obtained. Assuming the averaged brightness intensity, C, of each pixel, was proportional to the smoke concentration. The normalized distribution of smoke concentration, $(C\text{-}C_{min})/(C_{max}\text{-}C_{min})$, was evaluated, where C_{max} and C_{min} were maximum and minimum pixel values of averaged brightness intensity distribution. Note that the range of the experimental conditions is considered based on previous research (Sherlock and Stalker, 1941; Briggs, 1973) which is point out that the downwash would not occur in the range $U_j \geq 1.5\ U_0$, namely, the ratio of the jet velocity to the mean wind velocity should be greater than 1.5 to avoid downwash pattern. However, this is true irrespective of the imposed inlet turbulent conditions especially the quasi-isotropic turbulence. In addition, Snyder and Lawson (1991) stated that downwash from non-buoyant jets occurs if the speed ratio is less than about 1.5 in the subcritical regime (light wind) and about 1.1 in the supercritical regime (strong wind). In addition, in power plants the gases leave the stacks with temperature from 120 ^{o}C to 190 ^{o}C (Sherlock and Lesher, 1954) or around 150 ^{o}C to 250 ^{o}C (Michael, 2021). Moreover, as present in section 2.1.4 that plume dispersion is most easily described by discussing separately three aspects of plume behavior: (1) aerodynamic effects due to the presence of the stack, buildings, and topographical features; (2) rise relative to the mean motion of the air due to the buoyancy and initial vertical momentum of the plume; and (3) diffusion due to turbulence in the air (Briggs, 1969). In reality all three effects can occur

simultaneously, but in the present state of the art they are treated separately and are generally assumed not to interact. Consequently, these present experiments were carried out in the experimental conditions as shown in the table 3.2.

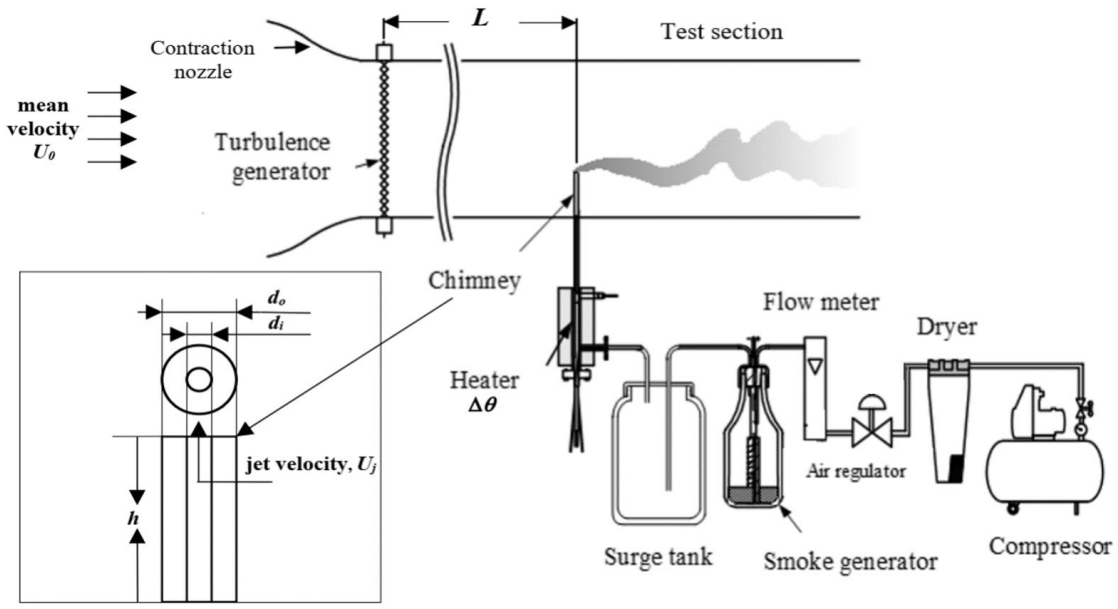

Fig. 3.7 Wind tunnel, chimney model, and smoke generation system.

Table 3.2 Experimental conditions.

temperature difference, $\Delta\theta$ [K]	0, 100, 200
jet velocity at the top of the chimney exit, U_j [m/s]	0.5, 0.6, 0.8, 1.0, 1.2, 1.4
crossflow velocity, U_0 [m/s]	0.3, 0.4, 0.6, 0.8, 1.0

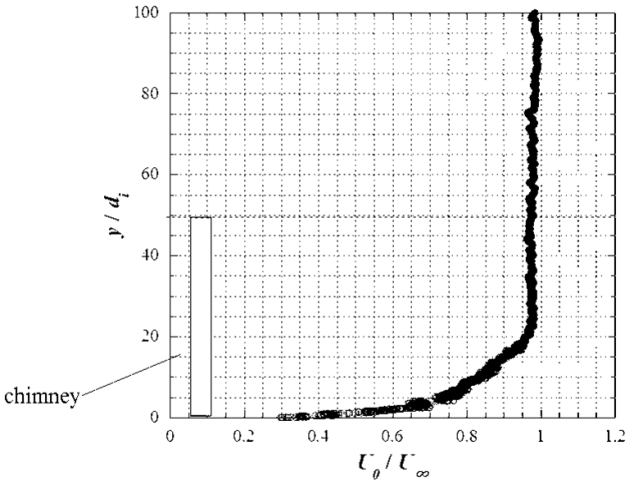

Fig. 3.8 Vertical mean wind velocity profile of the crossflow under quasi-isotropic turbulence.

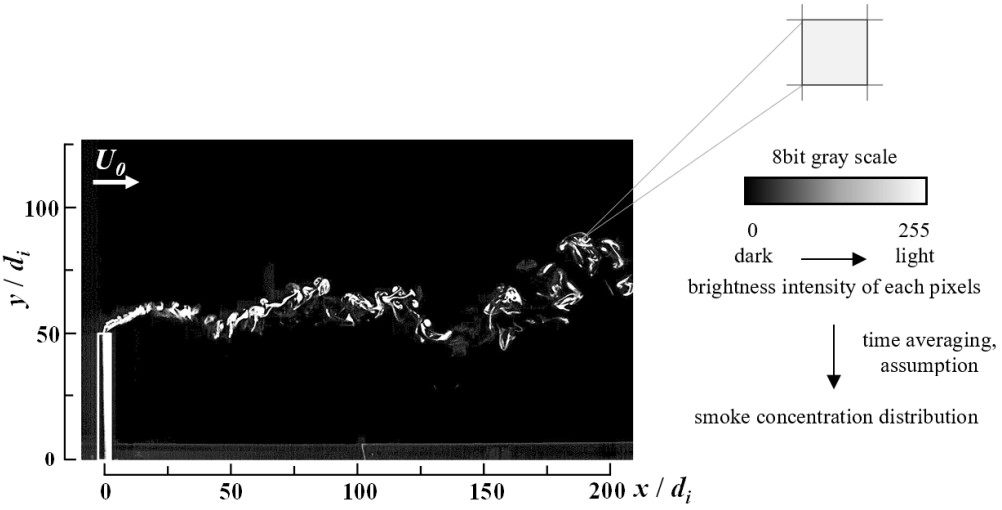

Fig. 3.9 Method for evaluating smoke concentration distribution.

3.2 Numerical simulations

Fire Dynamics Simulator (FDS, version 6.7.7) developed by the National Institute of Standards and Technology (NIST) was used for precise flow visualization of velocity, temperature, and concentration fields. The software solves numerically a form of the Navier-Stokes equations appropriate for low-speed, thermally driven flow with focus on smoke and heat transport from fires (McGrattan et al., 2021). The FDS, it has been applied in three major areas: basic research in fire dynamics, performance-based design, and forensic reconstructions of actual fires, since first publicly released in 2000 and it has recently undergone its sixth major

revision (McGrattan et al., 2014). In concept of fire triangle, a spontaneous combustion needs the following three things to be present: oxygen, sufficient temperature for ignition and combustible material. Though the perspective seems very simple, in reality, this contains many complex phenomena. For example, the combustion of the combustible gasses, the mass transfer of combustible gasses, even solid material, the heat transfers (conduction, convection, and radiation) from the flame to the combustible material and the surroundings, the buoyancy driven fluid flowing into and out going from the fire. These complex phenomena must be modelled in computational fluid dynamics (CFD) software. The CFD is a numerical tool to solve the governing equations for fluid flow. The governing equations include Navier-Stokes equations, and conservations of mass, energy, and species which can be applied to both laminar and turbulent flows. The area of interest is divided in many small volumes where the equations are discretized into algebraic equations following to the conceptual idea for derivatives over an arbitrary infinitesimal fluid element ($\Delta x, \Delta y, \Delta z$) (Kuo, 2005). Turbulence models for fire simulation, i.e., Direct Numerical Simulation (DNS), Large Eddy Simulation (LES), and Reynolds-Averaged Navier-Stokes (RANS), are gotten involve. Turbulent models of DNS require high computational cost for executing time, including fine mesh for fine tune; not likely the LES model, the uniform meshing is preferred. The DNS model is still limited to small *Re* (Wen et al., 2007). Moreover, as the compromise of the former two models, LES computes directly the large-scale eddies, and the sub-grid scale dissipative processes are simulated using sub-grid models (SGM). Most of all, LES can predict the unsteadiness and intermittency of the turbulence structure, which is the most important feature of flow fields (Hu et al., 2011). In the guidelines described by Tominaga et al. (2008) for practical applications of CFD to simulate pedestrian wind environment around buildings, which is proposed by the working group of the Architectural Institute of Japan (AIJ) as a good guide for important points when using RANS models, it is also deemed to be desirable to use a LES model to obtain more accurate results. Thus, LES is selected in this study fundamentals to simulate the flow behavior and dispersion with different wind velocities for observation the smoke ejected from a chimney. Moreover, the instability is purely driven by buoyancy force, which suits the purpose of software invention as mentioned very beginning of this section. The governing equations, except the thermal radiation solver which a finite volume technique is employed, are approximated with a finite difference's method. They are briefly discussed as the following section. For more detail, the governing equations and solution methods are described in FDS technical reference guide and FDS user's guide (McGrattan et al., 2021a, 2021b).

3.2.1 Governing equations

In LES mode, the transport Coefficients: the viscosity, thermal conductivity, and material diffusivity, are approximated from kinetic theory. That is because the temperature dependence of each coefficient is important in combustion scenarios. An empirical function of the temperature (*T*) is adopted to obtain the fluid viscosity at a point. Thermal conductivity is set as a function of viscosity and Prandtl number (*Pr*) that can be set by the user as an input property is order of 0.7 to be default value. The molecular diffusivity is based on mixture averaged binary Fickian diffusion. Postulate the nitrogen gas is the dominant species in any combustion scenario. Thus, the diffusion coefficient in the species mass conservation equations is that of the given species diffusing into nitrogen (McGrattan et al., 2021a).

3.2.1.1 Continuity

For infinitely small elemental volumes, conservation of mass can be written as the following equation.

$$\frac{\partial \rho}{\partial t} + \nabla \cdot (\rho \boldsymbol{u}) = 0 \tag{3.1}$$

Where $\boldsymbol{u}$ is velocity vector in considered spatial flow and ρ is filtered fluid density.

3.2.1.2 Momentum

$$\frac{\partial \rho \boldsymbol{u}}{\partial t} + \nabla \cdot (\rho \boldsymbol{u}\boldsymbol{u}) = -\nabla \bar{p} - \nabla \cdot \tau + (\rho - \rho_0) g \tag{3.2}$$

Where g is gravity vector, normally (0,0,-g) and variable density fluid is given by $\rho = p\bar{W}/TRu$. The inertia force is shown on the LHS and forces acting an infinitesimal volume element is spited into the terms as presented on the RHS. From the left to right, hydrostatic pressure gradient, and force due to viscous stress, and body weight, respectively.

3.2.1.3 Energy

$$\frac{\partial}{\partial t}(\rho h_s)+\nabla\cdot(\rho h_s \boldsymbol{u})=-\frac{D\bar{p}}{Dt}+\dot{q}'''+\dot{q}_b'''-\nabla\cdot\dot{q}'' \tag{3.3}$$

The LHS represents the changes of the local and convective of sensible enthalpy. First term on the RHS, Eulerian derivatives indicates the pressures in the system: the background pressure $\bar{p}(z,t)$ varying with height in gravimetric field and a perturbation pressure $\tilde{p}(x, y, z,t)$ driving the fluid motion in flow field.

$$\bar{p}=\rho T R_u \sum_\alpha \frac{Z_\alpha}{W_\alpha}=\frac{\rho T R_u}{\bar{W}} \tag{3.4}$$

The thermodynamic (background) pressure may be related in terms of the internal energy and enthalpy ($e=h_s-\bar{p}/\rho$). A given flowing fluid of a control volume per unit mass is defined as total energy ($e+\frac{v^2}{2}+gz$). The term $\dot{q}'''$ is the heat release rate per unit volume from a chemical reaction. The term $\nabla\cdot\dot{q}''$ represents combined heat fluxes: conductive, diffusive, and radiative transfers.

$$\dot{q}''=-k\nabla T-\sum_\alpha h_{s,\alpha}\rho D_\alpha \nabla Z_\alpha+\dot{q}_r'' \tag{3.5}$$

where k is the thermal conductivity and D_α is the diffusivity of species α. The Radiative Transfer Equation (RTE) is adopted to obtain the radiation intensity. Medium is considered as non-scattering medium and a relatively small number of bands with a separate RTE derived for each band (n); hence, an appropriate mean absorption coefficient (κ_n) for each band is computed. However, the drawback is if optically thin flames occur, the yield of soot is small compared to the yields of CO_2 and water vapor, the gray gas assumption (independent on wavelength, λ) can lead to an over-prediction of the emitted radiation yet, the current computation is fine anyway. The net contribution from the thermal radiation in the conservative energy equation is defined by:

$$\dot{q}_r'''=-\nabla\cdot\dot{q}_r''(x)=\kappa(x)[U(x)-4\pi I_b(x)] \quad (3.6)$$

where:

$$U(x)=\int_{4\pi} I(x,s')ds' \quad (3.7)$$

In real fires, soot is the dominant source and sink of thermal radiation ($\dot{q}_r'''$), not being particularly sensitive to wavelength (λ), so that the mean absorption coefficient (κ), is a function of species composition and temperature in spatial coordinates, from which a narrow-band model (Radcal) is adopted to obtain its values. In large scale fire simulations, the order of tens of centimeters is typically the size of grid cells. Thus, this means flame sheet cannot be resolved so that computed cell-average temperature becomes significantly lower than the temperature one would be expected in the reacting flame. Consequently, the source term is approximated in the grid cells, homogeneity of subgrid temperature filed, where the fuel and oxygen react.

3.2.2 Configurations and conditions of numerical simulation

The numerical simulations were performed using the fire dynamic simulator (FDS) software in a test section tunnel of 0.5 m of length as shown in Fig. 3.10. The cross section of test section tunnel is rectangular with a 0.2 m of width and 0.4 m of height. The two surfaces of the tunnel extremities are both open to the external ambient environment, but the tunnel entry is specified as an airflow inlet for longitudinal ventilation. The longitudinal velocity with turbulence intensity is set up by a supply air condition at ambient temperature introduced in the tunnel entry surface. The ambient temperature of the tunnel domain is prescribed via the TMPA parameter provided by FDS with values set about 20 °C in the series of tests simulations.

The chimney model with an inside diameter of d_i = 4 mm, an outside diameter of, d_o = 20 mm, and a height of h = 200 mm, was placed on the floor of the wind tunnel test section as shown in Fig. 3.10. The outside surface of the chimney is imposed the no-slip condition, while the inside surface of the chimney is imposed the adiabatic condition. The distance between the tunnel entry and the chimney is 100 mm. The wind flow is set to be perpendicular to the axis of the chimney with different levels of velocities. Flow pattern and smoke dispersion characteristics from the chimney are investigated. A specified inlet flow is set to blow into the left side of the simulation domain, whose top and other three sides are imposed the no-slip condition with no initial velocity boundary condition specified. The Reynolds number of the

inlet flow, defined by $Re = (\rho U_0 L/\mu)$, is about ranged in 3.95–11.19×10^3 with wind velocity of 0.3–1.0 m/s, which is a dimensionless number that assesses the relative importance of inertial force and viscous force in the flow fields. The present simulations were carried out with varying the numerical parameters as shown in Table 3.3: the temperature difference between the cross-wind and the jet from the chimney, $\Delta\theta$, the jet velocity at the top of the chimney exit, U_j, and the mean velocity of the cross-wind, U_0. Turbulence intensity, u_{rms}/U_0, is set about 10.25% in the quasi-isotropic turbulence case with the turbulence model of Deardorff and LES. The synthetic eddy method (SEM) vent profile for atmospheric is imposed.

In LES, the "turbulence model" refers to the closure for subgrid scale (SGS) flux terms. In FDS, gradient diffusion is the turbulence model used to close both the SGS momentum and scalar flux terms. Then, it requires a model for the turbulent transport coefficient: the turbulent (or eddy) viscosity or the turbulent (or eddy) diffusivity. The turbulent diffusivity is obtained using a constant Schmidt number (for mass diffusivity) or Prandtl number (for thermal diffusivity), as descried in detail in FDS technical reference guide and FDS user's guide (McGrattan et al., 2021a, 2021b), and so the most important transport coefficient is the turbulent viscosity, μ_t. There are several different options available that are described. The Deardorff model is the default. Its selection as the default was based on comparisons with a wide variety of full-scale experiments. As point out from Makita (Makita, 1991, 2007) that the turbulence characteristics of the flow have a significant impact on mixing and other behaviors of smoke dispersion, so the specification of nominally constant and uniform boundary conditions may be insufficient. To address this issue, FDS employs a synthetic eddy method (SEM). Refer to Jarrin (Jarrin, 2008) for a detailed description. In brief, "eddies" are injected into the flow at random positions on the boundary and advect with the mean flow over a short distance near the boundary equivalent to the maximum eddy length scale. Once the eddy passes through this region it is recycled at the inlet of the boundary with a new random position and length scale. The eddies are idealized as velocity perturbations over a spherical region in space with a diameter (eddy length scale) selected from a uniform random distribution. The selection procedures guarantee that prescribed first and second-order statistics (including Reynolds stresses) are satisfied (McGrattan et al., 2021b). Synthetic turbulence is invoked by setting the number of eddies, N_EDDY, the characteristic eddy length scale, L_EDDY, and either the root mean square (RMS) velocity fluctuation, VEL_RMS. Based on Deardorff model, the number of eddies, N_EDDY, and the characteristic eddy length scale, L_EDDY, are imposed 500 and 0.2 respectively. For the root mean square (RMS) velocity fluctuation, VEL_RMS, is 10.25%U_0 based on the experiment.

In LES simulation, the grid size is an important factor to be considered, which should be fine enough to include the turbulence scales associated with the largest eddy motions which can be described accurate enough by the sub-grid models (SGM). Balance must be considered for the grid size and the computation ability. Smaller grid size gives more detailed flow information but needs more computation resource. However, the basis of LES is that accuracy increases as the numerical mesh is refined. The reliability of such LES predictions is sensitive to the size and the quality of calculation grid. LES gives reasonable results with a grid size chosen carefully. The FDS user's guide (McGrattan et al., 2021b) suggests that a non-dimensional expression $D^*/\delta x$ can be used to measure how well the fire induced flow field could be resolved, where D^* is a characteristic fire diameter (m) and δx is the nominal size of a mesh cell (m), calculated by:

$$D^* = \left(\frac{\dot{Q}}{\rho_a c_p T_a \sqrt{g}}\right)^{2/5} \tag{3.8}$$

Where $\dot{Q}$ is heat release rate, ρ_a is ambient density, c_p is specific heat capacity, T_a is ambient temperature, and g is gravitational acceleration constant. The quantity $D^*/\delta x$ can be thought of as the number of computational cells spanning the characteristic diameter of the fire. Based on local and international scholars, the value of $D^*/\delta x$ ranged from 4 to 16 have good simulation results (Wei et al., 2013; Lui et al., 2020), so the grid size in our simulation is rectangular with a 0.002 m, 0.002 m, and 0.002 m in the *x*-, *y*-, and *z*-direction, respectively. The cell number is 250 × 100 × 200 in the *x*-, *y*-, and *z*-direction, respectively (total 5,000,000 cells). The grid size with 0.002 m is satisfactory to obtain the buoyancy-driven dynamics, assuming that characteristic buoyancy flow velocity is U = 1 m/s, the characteristic length in transport system can be estimated by U^2/g (where g is gravity acceleration) ~ 0.1 m > 0.002 m, revealing that the applied grid scale is fine enough to resolve the transport process in the present system.

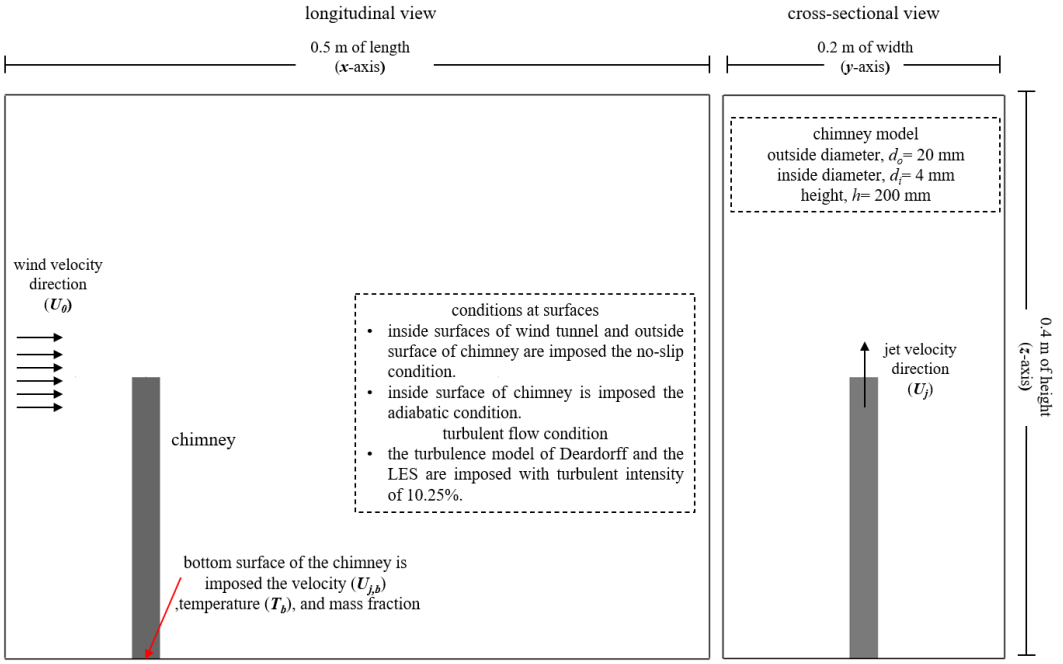

Fig. 3.10 Schematic view and cross section of the numerical model (unit: mm).

Table 3.3 Simulation conditions.

temperature difference, $\Delta\theta$ [K]	0, 200, 500
jet velocity at the top of the chimney exit, U_j [m/s] (*)	0.5–1.4
crossflow velocity, U_0 [m/s]	0.3–1.0

(*) $U_j = U_{j,b}$,where U_j stands for jet velocity at the top of the chimney exit and $U_{j,b}$ stands for jet velocity at the bottom of the chimney.

CHAPTER 4
THE EFFECT OF TURBLENCE ON HOT-SMOKE DISPERSION

4.1 Introduction and objective of this chapter

Although the rich past attempts have been made as pointed out in section 1.1 and in literature review on section 2.2, it is worthwhile to note that these works have been performed with the wind tunnel using high-drag strakes, roughness blocks, a turbulence grid in order to generate the incoming turbulence in the wind. Obviously, such technique may not be enough to reproduce the actual turbulent field as pointed out by Makita (Makita, 1991). Consequently, the precise smoke dispersion behavior is believed to depend on the quasi-isotropic turbulent eddy in the cross-wind and buoyancy of the hot-plume ejected through the chimney. In order to construct a turbulent diffusion model for the environmental assessment and prediction of atmospheric dispersion from a point source such as a chimney, having wind tunnel which allows to generate the turbulence in the real scale and observing the path of the smoke ejecting with the hot plume to include the buoyancy effect on the dispersion is essential for the investigation and the precise estimation of smoke dispersion. Therefore, the main purpose of this chapter is to investigate the patterns of smoke dispersion ejecting with hot gas from the chimney in order to fulfill the motivation as described in chapter 1 and which is the target of this research objectives. To understand the effect of imposed turbulent character onto the observed dispersion patterns, the results using the active turbulence grid (to promote quasi-isotropic turbulence) and the rectangular grid (to generate grid turbulence) are compared to reveal the impact of using active turbulent grid device on this subject.

4.2 Apparatus and method

Basically, the setup is similar to the Chapter 3 in the section 3.1 so that brief description is made here. The blowing-type atmospheric wind tunnel has the test section with the dimensions of 0.7×0.7 m^2 in cross section and 6 m in length. For generating turbulence in the wind tunnel, two turbulence generators were conducted which the active turbulence generator to generate quasi-isotropic turbulence and the rectangular grid to generate grid turbulence as shown in the Fig. 3.2. The chimney model with an inside diameter of d_i = 4 mm, an outside

diameter of d_o = 20 mm, and a height of h = 200 mm, was placed on the floor of the wind tunnel test section as indicated in Fig. 3.5. The present experiments were carried out with varying the experimental parameters as shown in Table 3.2. Turbulence intensity, u_{rms}/U_0, ranged from 9.5% to 11.0% and from 2.9% to 3.5% in the quasi-isotropic and grid turbulence cases, respectively. The patterns of the smoke dispersion were visualized by the high-speed camera (Photron, FASTCAM SA3 model, 1000 frame/s) and a halogen light.

4.3 Results and discussion

4.3.1 Observation of smoke behavior

Flow visualization experiments on two-dimensional were performed using the high-speed camera to distinguish the smoke dispersion patterns from the chimney under certain experimental conditions. A detailed observation of the behaviors of the heated and unheated jets from the chimney in the crossflow was conducted. The representative image of each smoke dispersion mode is shown in Fig. 4.1. In addition, to identify some characteristics (Fig. 4.2 (a-c)) and boundary layer (Fig. 4.2 (d-f)) of the smoke dispersion, the illustrations referred by observed facts in the experiments are also shown in Fig. 4.2. The smoke dispersion can be classified into six different patterns, Modes I-VI, based on the flow visualization images taken by the high-speed camera. These smoke patterns in the downstream field are dependent on the buoyancy force, turbulent motion, inertia force, etc. Note that the smoke patterns are categorized by its appearance with differences behavior based on the flow visualization images taken by the high-speed camera and referred by observed facts in the experiments, so that the transient case (fluctuate one mode to the other) cannot be clearly identified. Under the condition considered in this study, no such behavior is observed. Although the precise definition (not simply by the appearance) to categorize the mode is preferred when the boundary is center of discussion, the current (rough) definition is enough to fulfill the current purpose. Note that the smoke is appeared as the white zone as reflected image of the scattered light for visualization purpose.

Under the grid turbulence condition, when the buoyancy of the plume is relatively weak, two distinctive patterns so called Mode I and II can be identified. The structures of these modes are composed of (bifurcated) two longitudinal vortex tubes whose one end connected to the chimney exit. For Mode I, the two vortex tubes are apart from each other as shown in Fig. 4.2 (a). For Mode II, on the contrary, these two vortex tubes are strongly interacted due to the strong buoyancy as shown in Fig. 4.2 (b) and its cross-sectional view looks like the inverse

shape of a heart-type. Without the buoyancy, smoke patter shows differently from Modes I and II, so called Mode III as shown in Fig. 4.2 (c); the structure comprises of connecting hairpin-type vortices generated by the Kelvin-Helmholtz instability near the jet exit where the velocity shear is high. When buoyancy of the plume is further pronounced, no longer the bifurcated structure is kept, rather, the structure becomes rather random due to the developed coherent and turbulent vortices. This mode is categorized to Mode IV, and the turbulence in the field is pronounced by the shear force induced by the interface at the rising plume and the crossflow. Interesting to note that Mode IV is hardly observed when the cold jet ejecting; as noted, the smoke patterns in the cold jet tends to fall into Mode III. Important to note that these four modes (Modes I to IV) are found in the grid turbulence case adopted in this study.

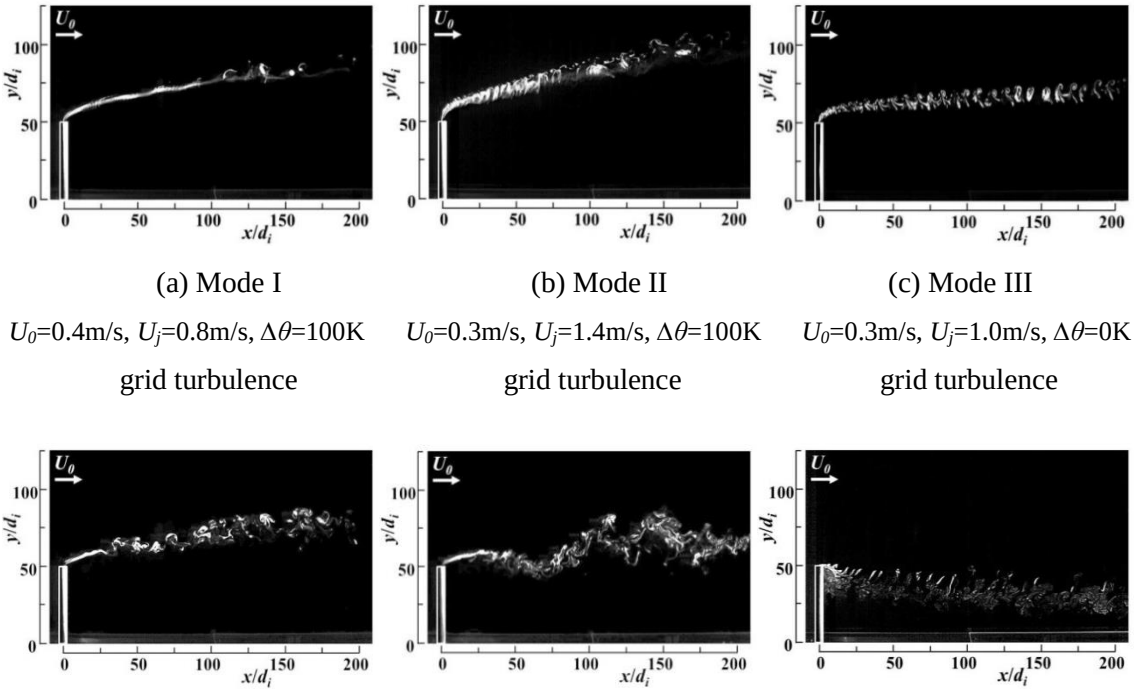

(a) Mode I
U_0=0.4m/s, U_j=0.8m/s, $\Delta\theta$=100K
grid turbulence

(b) Mode II
U_0=0.3m/s, U_j=1.4m/s, $\Delta\theta$=100K
grid turbulence

(c) Mode III
U_0=0.3m/s, U_j=1.0m/s, $\Delta\theta$=0K
grid turbulence

(d) Mode IV
U_0=0.4m/s, U_j=0.5m/s, $\Delta\theta$=200K
grid turbulence

(e) Mode V
U_0=0.6m/s, U_j=1.0m/s, $\Delta\theta$=200K
quasi-isotropic turbulence

(f) Mode VI
U_0=1.0m/s, U_j=0.5m/s, $\Delta\theta$=0K
quasi-isotropic turbulence

Fig. 4.1 Instantaneous images of smoke ejected from the chimney showing representative dispersion patterns.

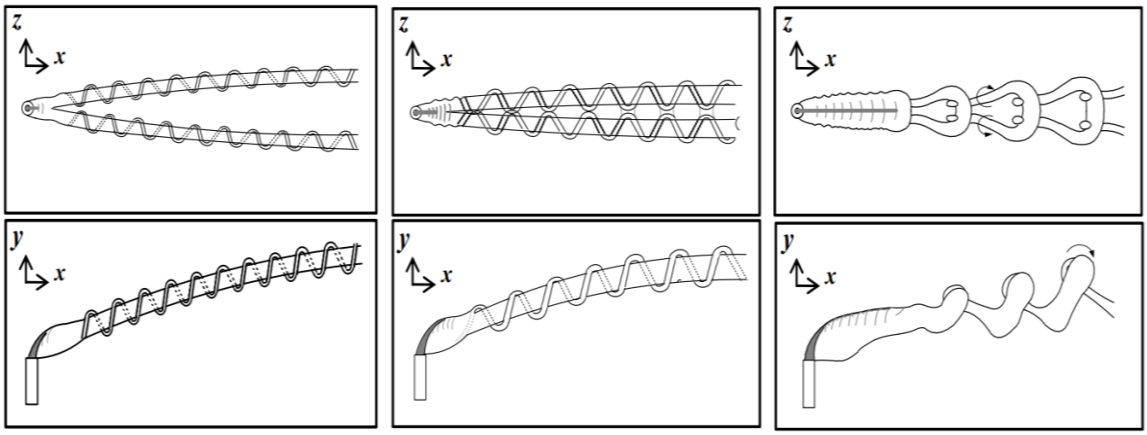

(a) Mode I (b) Mode II (c) Mode III

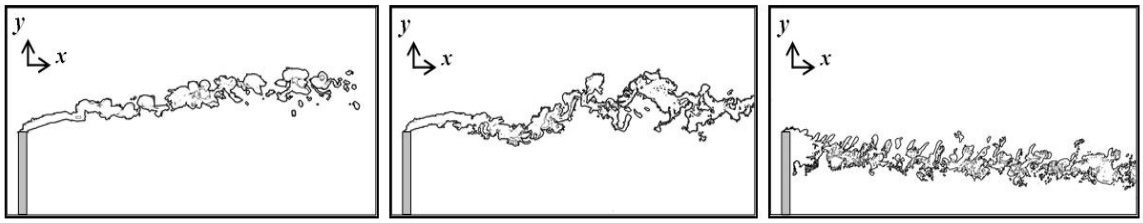

(d) Mode IV (e) Mode V (f) Mode VI

Fig. 4.2 Illustration of six smoke dispersion patterns, (a) bifurcated vortex tubes without strongly mutual interaction, (b) bifurcated vortex tubes with strongly mutual interaction, (c) connected hairpin-type vortices, (d) developed coherent vortices and the turbulent vortices, (e) meandering smoke diffusion, and (f) downwash dispersion.

By introducing the quasi-isotropic turbulence, no longer Modes I to III are observed, suggesting that such rigid structures are only available for unrealistic turbulent cases (in other word, they are only available for lab-scale testing, not actual large-scale phenomena). Instead, two different (featured) modes, called Modes V and VI, are mainly observed when the quasi-isotropic turbulence is induced in the crossflow. For Mode V, the smoke pattern shows the structure with the meandering motion is affected by the large integral scale in the quasi-isotropic turbulence case. The smoke structure of this mode is dispersed widely by the meandering motion which cannot be observed in the non-quasi-isotropic turbulence (grid turbulence) testing devices. This fact can be noticed that the turbulent eddies corresponding to the integral scale effectively contribute to the meandering smoke diffusion. The smoke diffusion is further promoted when higher jet velocity and slower crossflow velocity are adopted. The Mode V is clearly revealed that the effect of turbulent fields does effect on the smoke flow behavior which corresponding to the statement as point out by Makita (1991, 2007). For Mode VI, the smoke exhibits a downwash pattern with hairpin vortices due to the wake induced by the presence of

the chimney. In this mode, the smoke always stays below the chimney exit as shown in the figure (f) in Fig. 4.1 and Fig. 4.2, suggesting that this is quite serious case to exposure the harmful smoke directly to the people living nearby the facilities, which must be prevented. As shown in later, this mode (Mode VI) is identified at both inlet turbulent conditions (grid turbulence and quasi-isotropic turbulence), however, observed range is much limited when the grid turbulence is adopted (we will back this issue in next section).

As presented in the Section 3.1.1 that the active turbulence grid (quasi-isotropic turbulence) generator could generate quasi-isotropic turbulence fields with the high turbulence Reynolds number of R_L, R_λ , defined by the characteristic velocity and the integral scale or the microscale, about 9100 and 390, respectively, at the mean velocity in the cross-wind of U_0 = 5 m/s (Makita, 1991). That is, the large integral scale, large turbulence fluctuations, and the wide inertial subrange in the energy spectra of velocity fluctuations were achieved, as shown in Fig. 3.3. The inertial subrange spread for more than two orders of magnitude in wavenumber in the spectrum. An ideal turbulence field requires that the inertial motion of fluid takes a dominant role in the determining its structure. The requirement can be sufficed by attaining a sufficiently large turbulence number. Corrsin (1958) described that the existence of a clear initial subrange needed R_λ>250. The active turbulence grid generator is homogeneous and quasi-isotropic turbulence, having large turbulence intensity, u_{rms}/U_0, of more than 16% and the large longitudinal integral scale, L_{UX}, of about 200 mm which exceeds mesh size, M. While it is difficult for conventional grid turbulence (grid turbulence) to get the integral scale larger than the mesh size, M. Consequently, the Mode V, meandering smoke diffusion pattern, is clearly revealed the effect of imposed turbulent character onto the observed smoke dispersion patterns as shown in Fig. 4.3. It must be noticed that the scales of the meandering motion are almost the same as the integral scale of main flow turbulence in the quasi-isotropic turbulence. It is important to emphasize that Modes V and VI are mainly predicted using the quasi-isotropic turbulence generator in the lab-scale wind tunnel experiment. This fact suggests that the conventional grid turbulence generators, which often used in the wind tunnel experiment, would not be suitable to adopt in order to establish the precise assessment of the smoke-induced hazard and to work on modeling of the dispersion of the smoke in the atmosphere which is applicable to the actual scale phenomena.

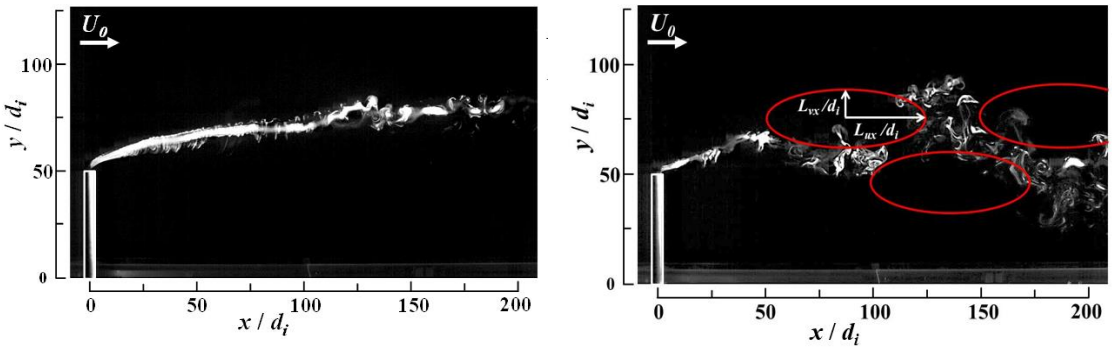

(a) grid turbulence

U_0=0.6m/s, U_j=1.2m/s, $\Delta\theta$=200K

(Mode II)

L_{vx}=6mm, L_{ux}=14mm

(b) quasi-isotropic turbulence

U_0=0.6m/s, U_j=1.2m/s, $\Delta\theta$=200K

(Mode V)

L_{vx}=68mm, L_{ux}=159mm

Fig. 4.3 The effect of imposed turbulent character onto the observed dispersion patterns.

4.3.2 Occurrence conditions of each mode

As learned so far, there are distinctive six modes of the smoke patterns depending on the inertia force of the flows (jet and wind) and buoyancy force. Let us summarize the occurrence those modes based on experimental parameters, such as temperature difference between the cross-wind and the jet from the chimney, $\Delta\theta$, the jet velocity at the top of the chimney exit, U_j, and the mean velocity of the cross-wind, U_0. Table 4.1 shows the summary comparing under the grid turbulence and the quasi-isotropic turbulence cases.

Table 4.1 Occurrence condition of each mode in the grid turbulence and the quasi-isotropic turbulence with the experimental conditions of $\Delta\theta$, U_j, and U_0.

		grid turbulence, preheated level, $\Delta\theta$ = 0 K						grid turbulence, preheated level, $\Delta\theta$ = 100 K						grid turbulence, preheated level, $\Delta\theta$ = 200 K					
		jet velocity at the top of the chimney exit, U_j [m/s]						jet velocity at the top of the chimney exit, U_j [m/s]						jet velocity at the top of the chimney exit, U_j [m/s]					
		0.5	0.6	0.8	1.0	1.2	1.4	0.5	0.6	0.8	1.0	1.2	1.4	0.5	0.6	0.8	1.0	1.2	1.4
mean wind velocity, U_0 [m/s]	0.3	III	III	III	III	III	III	I	I	I	I	II	II	IV	IV	IV	IV	IV	IV
	0.4	VI	III	III	III	III	III	I	I	I	II	II	II	IV	IV	IV	II	II	II
	0.6	VI	III	III	III	III	III	III	III	III	III	III	III	IV	IV	IV	II	II	II
	0.8	VI	VI	III	III	III	III	VI	III	III	III	III	III	IV	IV	IV	III	III	III
	1.0	VI	VI	VI	VI	III	III	VI	VI	VI	III	III	III	VI	VI	VI	III	III	III
		quasi-isotropic turbulence, preheated level, $\Delta\theta$ = 0 K						quasi-isotropic turbulence, preheated level, $\Delta\theta$ = 100 K						quasi-isotropic turbulence, preheated level, $\Delta\theta$ = 200 K					
		jet velocity at the top of the chimney exit, U_j [m/s]						jet velocity at the top of the chimney exit, U_j [m/s]						jet velocity at the top of the chimney exit, U_j [m/s]					
		0.5	0.6	0.8	1.0	1.2	1.4	0.5	0.6	0.8	1.0	1.2	1.4	0.5	0.6	0.8	1.0	1.2	1.4
mean wind velocity, U_0 [m/s]	0.3	VI	V	V	V	V	V	V	V	V	V	V	V	V	V	V	V	V	V
	0.4	VI	VI	V	V	V	V	V	V	V	V	V	V	V	V	V	V	V	V
	0.6	VI	VI	V	V	V	V	VI	V	V	V	V	V	V	V	V	V	V	V
	0.8	VI	VI	VI	V	V	V	VI	VI	V	V	V	V	VI	V	V	V	V	V
	1.0	VI	VI	VI	VI	VI	V	VI	VI	VI	VI	V	V	VI	VI	VI	V	V	V

As notified in the table, it is understood that Modes I–IV and VI appear in the grid turbulence case. Mode I, such as the bifurcation diffusion, appears by the buoyancy force only in the heated jet with temperature difference, $\Delta\theta$ = 100 K, in the case of a low cross-wind velocity and a low jet velocity. Mode II, such as the bifurcation dispersion by the buoyancy, is generated at the temperature difference, $\Delta\theta$, of 100 K and 200 K in the case of a low cross-wind velocity and a high jet velocity. It is clear to note that Modes I and II do not appear under the unheated (cold) jet. This means the buoyancy forces are sufficient to counteract some of the adverse pressure forces produced by the cross-wind velocity. This fact suggests that the buoyancy plays a role on appearance of Mode I and II. On the contrary, Mode III, such as the hairpin-type dispersion, is found in the case of a low cross-wind velocity and a high jet velocity when the cold jet is adopted. When the jet is preheated, appearance of this mode is switching to a high cross-wind velocity condition and a high jet velocity condition. Mode IV, such as the developed coherent and turbulent vortices by the turbulent motion, appears in the case of a

cross-wind velocity of U_0 = 0.3 m/s and a low jet velocity. Appearance of this mode is rather limited to the condition, only for the heated jet with temperature difference of $\Delta\theta$ = 200 K.

Again, Modes V and VI are identified mainly in the case of the quasi-isotropic turbulence adopted in the main external flow. Mode V, such as the meandering smoke diffusion pattern, appears in the case of a low cross-wind velocity and a high jet velocity with both the heated and the unheated jets. This suggests that the effect of the turbulent motion is rather dominant than that of the buoyancy force. In the case of a lower jet velocity and a higher crossflow velocity, however, the meandering smoke pattern is appeared more apparently when the highly heated jet is employed. Mode VI, such as the downwash dispersion pattern, appears under the condition of a high cross-wind velocity and a low jet velocity in both the heated and the unheated jets. Because imposing relatively high averaged cross-wind, a pair of strong vortices shall formed behind the chimney under such condition. In case the jet velocity is low or the buoyancy effect is small, the smoke does not enough force to release upwardly and tends to be drawn by the vortex behind the chimney. Previously, Sherlock and Stalker (1941) and Briggs (1973) pointed out that the downwash would not occur in the range $U_j \geq 1.5\ U_0$. In our experiment, the same conclusion is drawn, and this is true irrespective of the imposed inlet turbulent conditions.

4.3.3 Proposed model for smoke distribution trajectories

By superposing 500 instantaneous images, shown in Fig. 3.9, the time averaged brightness intensity distribution was obtained. Assuming the averaged brightness intensity, C, of each pixel, was proportional to the smoke concentration. The normalized distribution of smoke concentration, $(C\text{-}C_{min})/(C_{max}\text{-}C_{min})$, was evaluated, where C_{max} and C_{min} were maximum and minimum pixel values of averaged brightness intensity distribution. The smoke concentration distribution from the chimney in the quasi-isotropic turbulence and the grid turbulence is then examined. The normalized distributions of the time-averaged smoke concentration are shown in Fig. 4.4 as typical examples. Figure 4.4 (a) shows the case where Mode II is observed with the grid turbulence, while Fig. 4.4 (b) shows the case where Mode V is observed with the quasi-isotropic turbulence. The distribution is obtained based on the motion pictures of smoke taken by the high-speed camera. The peak of the normalized smoke concentration distribution in the quasi-isotropic turbulence case is lower than that in the grid turbulence case. In the case of the quasi-isotropic turbulence, the smoke is diffused more widely by the meandering motion of the crossflow, and the concentration peak disappear more rapidly than in the case of the grid

turbulence. This can be explained by the significant fluctuations of the velocity and direction of the cross-wind. The diffusion width in the case of the quasi-isotropic turbulence is wider than that in the case of the grid turbulence. This is because the quasi-isotropic turbulence is irregular, unsteady, and chaotic. This revealed the effect of imposed turbulent character onto the observed smoke dispersion patterns. Consequently, it is convinced that an appearance of meandering motion promotes the smoke dispersion in the present work. However, it is unfortunate that the boundary of mode V and VI is not very clear and not systematically determined. Further study is preferred to precisely understand the occurrence mechanism of mode VI which will be discussed in the next chapter (chapter 5).

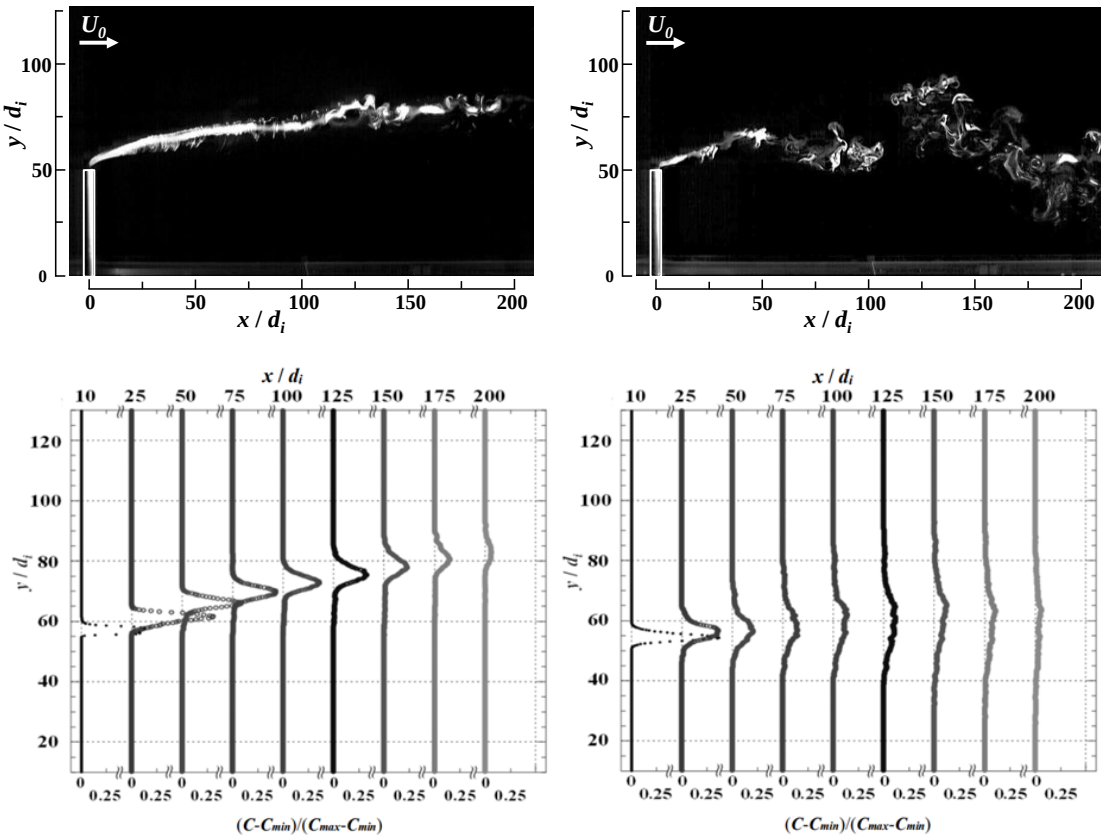

(a) grid turbulence
U_0=0.6m/s, U_j=1.2m/s, $\Delta\theta$=200K
(Mode II)

(b) quasi-isotropic turbulence
U_0=0.6m/s, U_j=1.2m/s, $\Delta\theta$=200K
(Mode V)

Fig. 4.4 Distributions of the normalized smoke concentration.

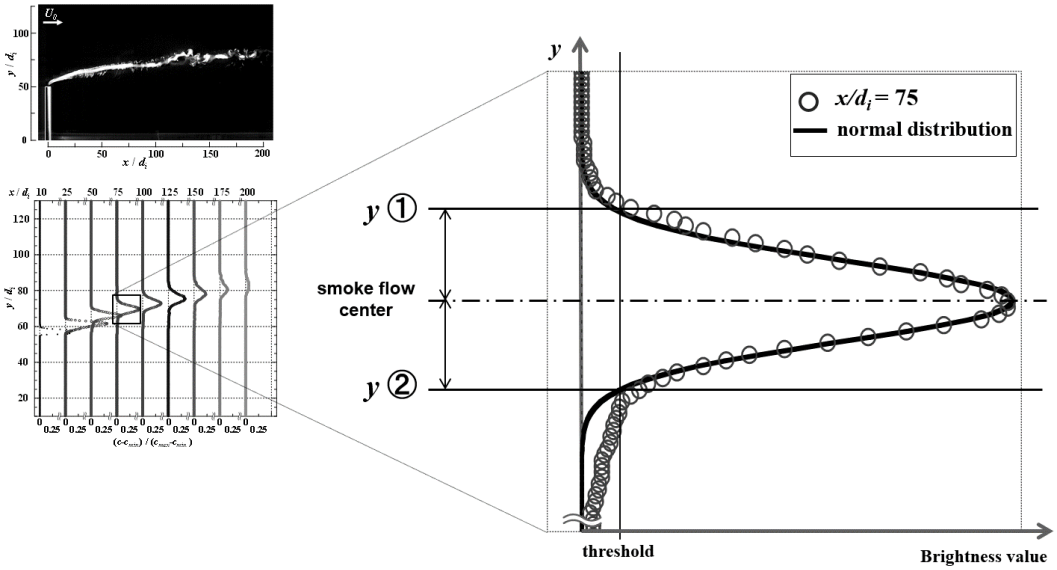

Smoke concentration distribution is assumed to follow a normal distribution

↓

Assuming that the midpoint between heights y ① and y ② is the smoke flow center

grid turbulence

U_0=0.6m/s, U_j=1.2m/s, $\Delta\theta$=200K, (Mode II)

Fig. 4.5 Fitting a Gaussian distribution to the vertical distribution data of smoke concentration.

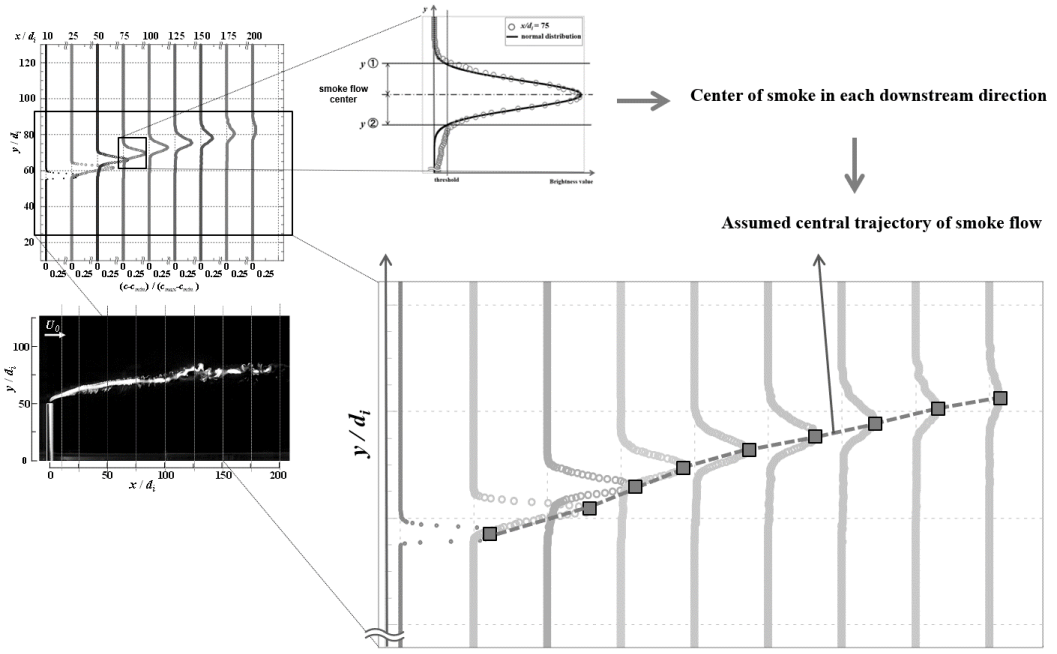

grid turbulence

U_0=0.6m/s, U_j=1.2m/s, $\Delta\theta$=200K, (Mode II)

Fig. 4.6 The peak of the Gaussian distribution of the center of smoke flow.

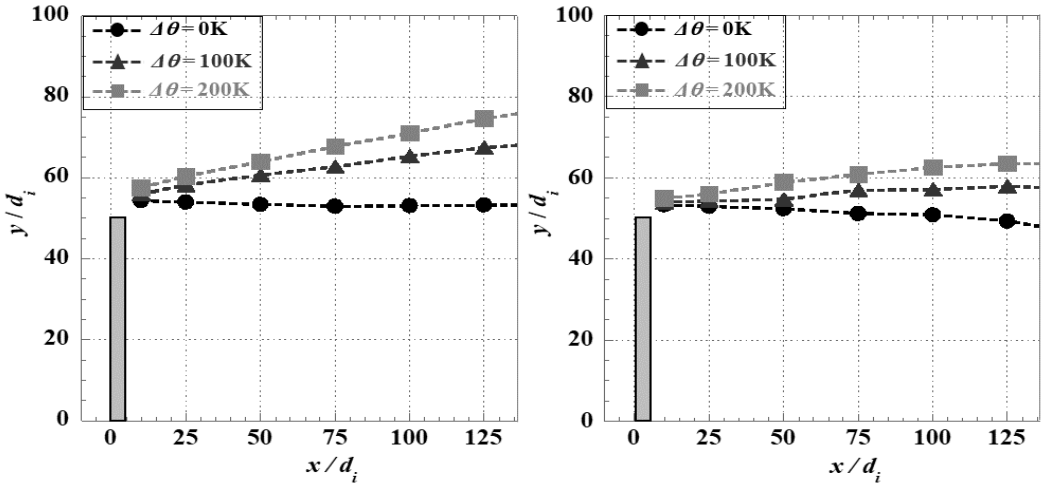

(a) grid turbulence U_0=0.6m/s, U_j=1.2m/s

(b) quasi-isotropic turbulence U_0=0.6m/s, U_j=1.2m/s

Fig. 4.7 The trajectories of the smoke flow center.

As can be seen from Fig. 4.4, the distribution of the time-averaged smoke concentration can be approximated by Gaussian distribution. By fitting the Gaussian distribution to the vertical distribution data of smoke concentration as shown in Fig. 4.5, the center of smoke flow is determined at the peak of the Gaussian distribution as shown in Fig. 4.6. The trajectories of the smoke flow center are shown in Fig. 4.7 for various temperature differences. Fig. 4.7 (a) shows the case of the grid turbulence and Fig. 4.7 (b) shows the case of the quasi-isotropic turbulence. The jet velocity and cross-wind velocity are the same in these charts. Although the smoke of the unheated jet flow down straight, the smoke of heated jet rise with an increase of the downstream distance in the grid turbulence case. In contrast to this, the smoke of the heated jet does not rise so much in the quasi-isotropic turbulence case, and the smoke of the unheated jet descend with an increase of downstream distance in the quasi-isotropic turbulence case.

By fitting the Gaussian distribution to the vertical distribution data of smoke concentration, the diffusion width is obtained as the standard deviation value of the Gaussian distribution as shown in Fig. 4.8. The variations of smoke diffusion width with an increase of downstream distance are shown in Fig. 4.9 for various temperature differences. Fig. 4.9 (a) displays the grid turbulence case and Fig. 4.9 (b) displays the quasi-isotropic turbulence case. The conditions of the cross-wind velocity and the jet velocity are the same in these charts. The diffusion width in the quasi-isotropic turbulence case is higher than that in the grid turbulence case. This is revealed the effect of the effect of imposed turbulent character onto the observed

smoke dispersion. The diffusion width is not affected so much by the temperature difference in the grid turbulence case. The diffusion width increases gradually with an increase of downstream distance in the grid turbulence case. On the other hand, the diffusion width increases more rapidly with an increase of downstream distance in the quasi-isotropic turbulence case. The diffusion width is large when the temperature difference is large.

The experimental data of dispersion width variations with downstream distance are compared with previous correlations of Sutton (Sutton, 1932)

$$\sigma_y = \frac{C_y}{\sqrt{2}} x^{\left(1-\frac{n}{2}\right)} \tag{4.1}$$

and Passqill&Grifford (Grifford, 1961)

$$\sigma_y = \gamma_y x^{a_y} \tag{4.2}$$

Where C_y, n, are constants of correlations of Sutton, these values depending on atmospheric stability and source height; and γ_y, α_y, are coefficients for dispersion parameter of correlations of Passqill&Grifford, these values depending on atmospheric stability and downwind distance.

The results are shown in Fig. 4.9 by bold solid lines. Constants of correlations of Sutton, C_y = 0.07 and n = 0.25, and coefficients for dispersion parameter of correlations of Passqill&Grifford, γ_y = 0.1046 and α_y = 0.826, for neutral air stability are employed to evaluate the diffusion width from these correlations. The widths estimated from the Sutton's correlation is closer to the experimental results than those estimated from the Passqill&Grifford's correlation in both the grid turbulence and the quasi-isotropic turbulence cases. The widths estimated from the Passqill&Grifford's correlation deviates significantly in our results because the dispersion coefficients for neutral air stability are employed to evaluate the diffusion width from this correlation based on the actual atmospheric wind and large scale of downwind distance. When compared in our results (lab scale), these coefficients for dispersion parameter γ_y = 0.1046 and α_y = 0.826, are not suitable. So, as the estimated diffusion width fit the experimental data more closely, the constants C_y and n of Sutton's correlation are modified. The modified values of C_y and n in the grid turbulence and the quasi-isotropic turbulence cases are shown in Table 4.2. The diffusion of air pollution from an elevated point source is estimated by following equation (Pasquill, 1974; Hu and Duan, 2015; Xu et al., 2021; Li et al., 2021).

$$C = \frac{Q_v}{2\pi\sigma_y\sigma_z U_0} exp\frac{-z^2}{2\sigma_z^2}\left\{exp\left(-\frac{(H-y)^2}{2\sigma_y^2}\right)+exp\left(-\frac{(H+y)^2}{2\sigma_y^2}\right)\right\} \tag{4.3}$$

By substituting experimentally obtained σ_y into σ_y and σ_z of eq. (4.3), taking experimental data of the smoke flow center into H of eq. (4.3), and setting z to zero, the concentration distribution is estimated and compared with experimental data. The results are shown in Fig. 4.10 by solid curves. Here, the volume flow rate of Q_v is determined so as the maximum of estimated concentration at x/d_i = 10 much with experimental data. A relatively fair agreement is found between the experimental and predicted results, suggesting that the smoke distribution in the quasi-isotropic turbulence and the grid turbulence almost follows the equation of the air pollution diffusion from a point source. It is noted that slight discrepancy is found in upper half of the smoke profile, where the observed smoke spreads a bit wider toward the vertical direction. To reveal this issue further, other approach would be encouraged to introduce.

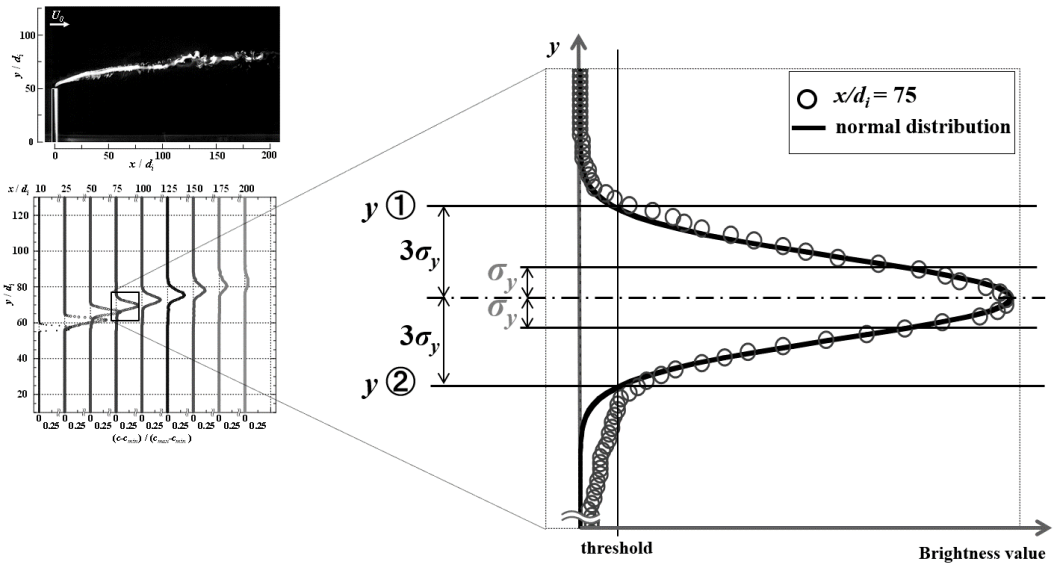

grid turbulence

U_0=0.6m/s, U_j=1.2m/s, $\Delta\theta$=200K, (Mode II)

Fig. 4.8 The diffusion width obtained as the standard deviation value of the Gaussian distribution.

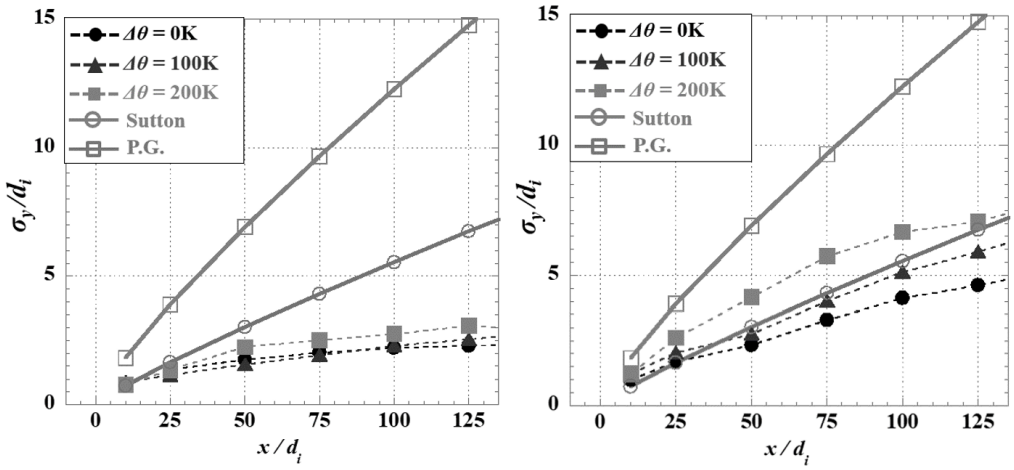

(a) grid turbulence
U_0=0.6m/s, U_j=1.2m/s

(b) quasi-isotropic turbulence
U_0=0.6m/s, U_j=1.2m/s

Fig. 4.9 Variation of the diffusion width of smoke with an increase of the downstream distance.

Table 4.2 Modified values of constants of C_y and n in the grid turbulence and the quasi-isotropic turbulence cases.

grid turbulence			quasi-isotropic turbulence		
$\Delta\theta$ [K]	C_y [m$^{n/2}$]	n [-]	$\Delta\theta$ [K]	C_y [m$^{n/2}$]	n [-]
0	0.0175	1.2	0	0.0420	0.65
100	0.0190	1.1	100	0.0515	0.68
200	0.0260	0.9	200	0.0630	0.71

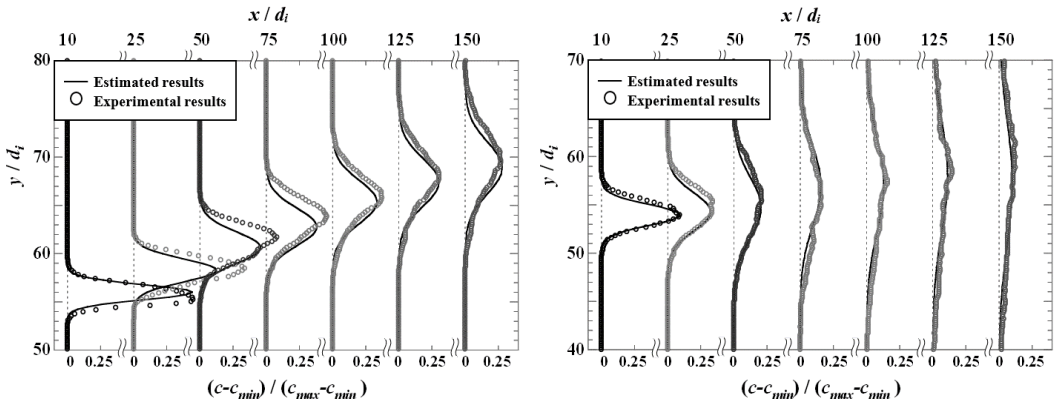

(a) grid turbulence
U_0=0.6m/s, U_j=1.2m/s, $\Delta\theta$=100K
(Mode III)

(b) quasi-isotropic turbulence
U_0=0.6m/s, U_j=1.2m/s, $\Delta\theta$=100K
(Mode V)

Fig. 4.10 Comparison of the smoke concentration distributions between experimental results and estimated results from eq. (4.3).

The present experiment is successful in the realization of the smoke dispersion patterns of the heated and the unheated jets from the chimney which can be observed in the actual atmospheric boundary layer using the atmospheric wind tunnel with the active turbulence grid (namely, quasi-isotropic turbulence). The present experimental results can serve as a reference for construction of turbulence diffusion models for the environmental assessment and prediction of atmospheric dispersion from the point source such as chimneys. Nevertheless, the boundary of appearance of the downwash pattern is not yet open discussion and yet to be modeled with logical manner which is studied in the next chapter by approach the scaling law.

4.4 Concluding remarks of this chapter

Flow visualization experiments were performed using a high-speed camera to distinguish the smoke dispersion patterns from the chimney under certain experimental conditions. The structures of the dispersed smoke with the heated and unheated jets from the chimney were investigated, and their occurrence conditions under the grid turbulence and the quasi-isotropic turbulence cases were clarified. The following conclusions were deduced:

(1) It was succeeded to reproduce meandering smoke dispersion which could be observed in the actual atmospheric boundary layer. This meandering smoke dispersion was realized under the quasi-isotropic turbulence generated in the atmospheric wind tunnel with the active turbulence grid (quasi-isotropic turbulence), suggesting that using active turbulence

generator with the lab-scale wind tunnel was quite powerful tool to predict the actual smoke dispersion observed in the wide range of the wind condition.

(2) The meandering smoke dispersion was dispersed more widely affected of the meandering motion by the large integral scale in the quasi-isotropic turbulence, suggesting that the turbulent eddies corresponding to the integral scale effectively contribute to the meandering smoke diffusion.

(3) The patterns of the smoke dispersion in the downstream field from the chimney were divided into six modes depending on the turbulent motion, the inertia forces, the buoyancy force, etc. Mode V, the meandering dispersion, occurred in the quasi-isotropic turbulence case. Conversely, Modes I-IV appeared in the grid turbulence case. Mode VI, the downwash dispersion, occurred in both the quasi-isotropic turbulence and the grid turbulence cases.

(4) For the Modes I and II, the two longitudinal vortex tubes were generated without and with strongly mutual interaction, respectively. The bifurcation structure was produced by the buoyancy force near the jet exit when the buoyancy was dominant. For the Mode III, the hairpin-type vortices occurred by the Kelvin-Helmholtz instability. For the Mode IV, the structure was comprised of the developed coherent vortices and the turbulent vortices. For the Mode V, the meandering structure was affected of the turbulent motion. For the Mode VI, the downwash structure occurred behind the chimney. These smoke diffusions were depended on the turbulent motion, the inertia force, the buoyancy force, etc.

(5) Mode VI, the downwash pattern occurred behind the chimney, preferred to appear under the quasi-isotropic turbulent case, implying that the selection of proper turbulent field was strongly demanded to predict the condition to have direct smoke exposure.

(6) In the quasi-isotropic turbulence case, the variations of the smoke diffusion width with an increase of downstream distance almost agreed with Sutton’s correlation for neutral air stability case. The concentration distribution of smoke could be estimated using equation on the diffusion of air pollution from point source with experimentally obtained constants.

CHAPTER 5
SCALE MODELING OF AN APPEARANCE OF DOWNWASH

5.1 Introduction and objective of this chapter

Based on our finding in chapter 4, smoke patterns appear randomly one the smoke was issued from the chimney in the cross-wind atmosphere. However, the patterns are mainly categorized into several typical ones based on the characteristic motion of the smoke behind the chimney. With special attention should be paid to the downwash smoke pattern, such that the ejected smoke is “pushed back” to downward and smoke is distributed toward the ground behind the chimney. This is the serious problem for actual chimneys. Once this mode appears, the people living in downstream region behind the chimney are directly exposed the harmful gas to potentially cause the severe health damage, which must be prevented (Huang and Hsieh, 2002; Overcamp, 2001; Canepa, 2004; Gnatowska, 2015; Sekishita et al., 2019). Therefore, the higher-order prediction of the appearance of downwash patterns ejected from the high-rise chimney in the natural wind is strongly demanded. Interestingly, our finding in chapter 4 has been figured out that the turbulence field does affect on the smoke dispersion patterns, suggesting that the precise study on the appearance of the downwash patterns in the actual scale needs the special wind tunnel which can generate the turbulent field of the natural wind. Nevertheless, the boundary of appearance of the downwash pattern is not yet open discussion and yet to be modeled with logical manner. Moreover, although, the occurrence condition of downwash pattern was pointed out, but this is in the certain experimental condition. Furthermore, the universal rule to determine the appearance of downwash is not yet discussion. Consequently, this study will introduce the law approach to obtain the scaling law for this problem to determine the appearance of the downwash pattern in feasible and universal which is the target of this research objective. Therefore, in this chapter, parametric studies on visualizing the smoke patterns ejected from the chimney are widely made using the specialized wind tunnel, which shall generate quasi-isotropic turbulence field developed by Makita (Makita, 1991). From the observed results, the law approach is adopted to find the candidate of the scaling law to exhibit the appearance of downwash smoke pattern in the cross-wind.

5.2 Experimental and numerical apparatus

Basically, the system is identical to chapter 3 in the section 3.1 of the experiment and in the section 3.2 of numerical simulation, only brief description is made here. Note that only one case of turbulence (namely, the quasi-isotropic turbulence generated by the active turbulence generator) is considered in both the experiment and the numerical simulation. The active turbulence generator developed by Makita (Makita, 1991) was equipped at upstream of the test section to produce the quasi-isotropic turbulence. It is ensured to generate the large integral scale, large turbulence fluctuations, and the wide inertial subrange in the energy spectra of velocity fluctuations at 5 m/s of averaged flow speed. The chimney model of d_i = 4 mm in inside diameter, d_o = 20 mm in outside diameter and h = 200 mm in height was placed on the floor of the test section as same in both the experiment and the numerical simulation.

The experiments and numerical simulation were carried out in the experimental and numerical conditions of temperature differences between the cross-wind and the jet from the chimney, various jet velocities at the top of the chimney exit, and various mean velocities of the cross-wind as shown in the Table 3.2 and Table 3.3, respectively.

5.3 Dataset for scale modeling

5.3.1 Two modes of smoke patterns (Mode V and Mode VI)

Based on our finding in chapter 4, six-kinds of the featured patterns are clearly identified, whereas only two-kinds of modes (Mode V and Mode VI) were observed in the active turbulence case (namely, the quasi-isotropic turbulence) which is quite powerful tool to predict the actual smoke dispersion observed in the actual atmospheric boundary layer. This fact suggests that the conventional grid turbulence generators, which often used in the wind tunnel experiment, would not be suitable to adopt in order to establish the precise assessment of the smoke-induced hazard and to work on modeling of the smoke dispersion in the atmosphere which is applicable to the actual scale phenomena. With this respect, only one case of turbulence (namely, the quasi-isotropic turbulence generated by the active turbulence generator) is considered to propose the scaling law to provide boundary for appearance of downwash pattern.

Figure 5.1 shows the typical two types of smoke pattens (i.e., Modes V and VI) appeared in this experiment. Note that the smoke is appeared as the white zone as reflected image of the scattered light for visualization purpose. As clearly shown in the Fig. 5.1, Mode V

exhibits a meandering motion toward downstream, where the smoke is dispersed more widely by the meandering motion due to the large integral scale. Mode VI exhibits downwash, where the smoke is attached behind the top of the chimney and directed to the ground downstream to cause potential health damage by the eddies and the wake behind the chimney. The downwash pattern tends to appear when a high cross-wind velocity was adopted even at heated jet condition. Note that the smoke patterns are categorized by its appearance with differences behavior based on the flow visualization images taken by the high-speed camera and referred by observed facts in the experiments, so the transient case (fluctuate one mode to the other) cannot be clearly identified (transition is rather continuous). In this study, it is considered that Mode VI is defined as more than half-chance appearance of the "attached smoke behind the chimney". Although the precise definition to categorize the mode is preferred, it is difficult to work further in the present experiment. Therefore, further discussion on any behavior in the transition case is not included in this work. However, the current (rough) definition is enough to fulfill the current purpose according to Overcamp (2001) point out that the criteria for downwash differ in many researches. Overcamp (2001) point out that, in a few cases, the original investigator described downwash as the condition in which the lower boundary of the plume drops below either the top of the stack or some specified distance, such as one diameter, below the top of the stack. In other studies, this author inferred the absence of downwash if the far-field data for the centerline of the plume fit the two-thirds law for buoyant plumes (Overcamp, 2001). In fact, it was refrained that the main issue on this work is to figure out the key mechanism to identify Modes V and VI (appearance of downwash pattern of the smoke behind the chimney) through scale modeling approach.

Table 5.1 summarizes the appearance of these modes in tested range of the experimental parameters, such as temperature difference between the cross-wind and the jet from the chimney, $\Delta\theta$, the jet velocity at the top of the chimney exit, U_j, and the mean velocity of the cross-wind, U_0. Interestingly, it is noted that the region which appeared as Mode VI clearly depends on the heated smoke temperature in certain experimental conditions, suggesting that the buoyancy of the smoke would lift-up the smoke to prohibit the occurrence of the downwash patterns. Furthermore, it is clearly confirmed that the overall trend to appear downwash mode (transition boundary between Mode V and Mode VI) is similar to any preheated cases. This observed fact brings the possibility of having certain scaling law to identify the boundary of two modes, namely, the appearance of the downwash pattern, which is the target of the present study. Notice that, in our finding in chapter 4, it is interesting to find that the range of the appearance of Mode VI is not sensitive to turbulence. Namely, Mode VI is preferred to appear

as a “high-mean flow and low-buoyancy condition” even when using the grid turbulence generator. This fact suggests that the appearance of downwash pattern (Mode VI) might be insensitive to the turbulence character.

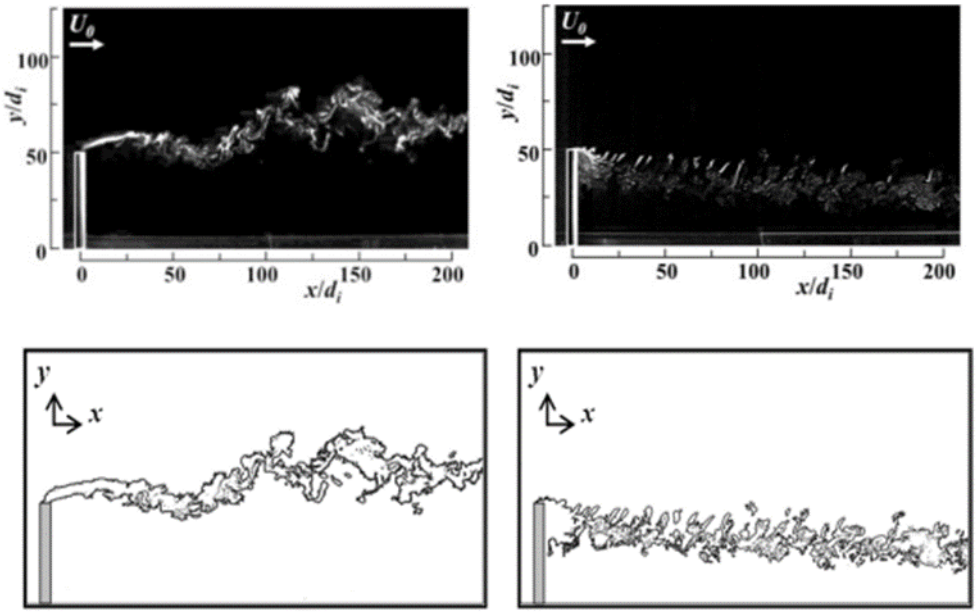

Mode V

U_0 = 0.6 m/s, U_j = 1.0 m/s, $\Delta\theta$ = 200 K

Mode VI

U_0 = 1.0 m/s, U_j = 0.5 m/s, $\Delta\theta$ = 0 K

Fig. 5.1 Representative and distinctive illustration of two patterns of smoke behaviors (Modes V and VI).

Table 5.1 Appearance of each mode (Mode V and Mode VI (shaded)) in the quasi-isotropic turbulence with the experimental conditions of $\Delta\theta$, U_j, and U_0.

		quasi-isotropic turbulence, preheated level, $\Delta\theta$ = 0 K						quasi-isotropic turbulence, preheated level, $\Delta\theta$ = 100 K						quasi-isotropic turbulence, preheated level, $\Delta\theta$ = 200 K					
		jet velocity at the top of the chimney exit, U_j [m/s]						jet velocity at the top of the chimney exit, U_j [m/s]						jet velocity at the top of the chimney exit, U_j [m/s]					
		0.5	0.6	0.8	1.0	1.2	1.4	0.5	0.6	0.8	1.0	1.2	1.4	0.5	0.6	0.8	1.0	1.2	1.4
mean wind velocity, U_0 [m/s]	0.3	VI	V	V	V	V	V	V	V	V	V	V	V	V	V	V	V	V	V
	0.4	VI	VI	V	V	V	V	V	V	V	V	V	V	V	V	V	V	V	V
	0.6	VI	VI	V	V	V	V	VI	V	V	V	V	V	V	V	V	V	V	V
	0.8	VI	VI	VI	V	V	V	VI	VI	V	V	V	V	VI	V	V	V	V	V
	1.0	VI	VI	VI	VI	VI	V	VI	VI	VI	VI	V	V	VI	VI	VI	V	V	V

Figure 5.2 shows the typical of smoke downwash patten (Mode VI) appeared in the numerical simulation where Fig. 5.2 (a) is smoke contour and Fig. 5.2 (b) is line-smoke contour. As clearly shown in the Fig. 5.2, Mode VI exhibits downwash, where the smoke is attached behind the top of the chimney and directed to the ground downstream to cause potential health damage by the eddies and the wake behind the chimney as same in the experimental results as shown in Fig. 4.1 (f) or in Fig. 5.1. The downwash pattern tends to appear when a high cross-wind velocity was adopted even at heated jet condition. This reveals that the descending downwash flow entrains large amounts of ambient fluids. The turbulent masses of smoke immediately above and behind the chimneys are separated from the smoothly flowing upper layers of wind flow by a vortex sheath as same as present in the section 2.1.4.1. Note that the concentration of carbon monoxide (CO) higher than 100 ppm (>100 ppm) is assumed to defined as the smoke concentration which effect to human health. This threshold is referred according to statistics (ATSDR, 2012), when the concentration of CO in the indoor air exceeds 100 ppm, it will produce a toxic effect on the human body, resulting in hypoxia and suffocation. For the criteria for downwash pattern, the smoke coverage length (L_d, called "downwash length") at the behind of the chimney is characteristic length scale to define the pattern of the downwash in this study. $L_d/d_i \leq 0$ is defined that the meandering motion pattern (mode V) and $L_d/d_i > 0$ is defined that the downwash pattern (mode VI). Based on this definition, the appearance of the mode V and mode VI is investigated.

Table 5.2 summarizes the appearance of these modes in tested range of the numerical simulation parameters, such as temperature difference between the cross-wind and the jet from the chimney, $\Delta\theta$, the jet velocity at the top of the chimney exit, U_j, and the mean velocity of the cross-wind, U_0. It is found that the region which appeared as Mode VI clearly depends on the heated smoke temperature in certain numerical simulation conditions as same in the experimental results as shown in Table 5.1, it reveals to convinced that the buoyancy of the smoke lift-up the smoke to prohibit the occurrence of the downwash patterns. Furthermore, it is clearly confirmed that the overall trend to appear downwash mode (transition boundary between Mode V and Mode VI) is similar to any preheated cases. Note that the jet velocity from the chimney of U_j = 0.3 m/s is conducted in the case of temperature difference of $\Delta\theta$ = 500 K for getting more results of the appearance the downwash pattern to support the proposed the scaling law.

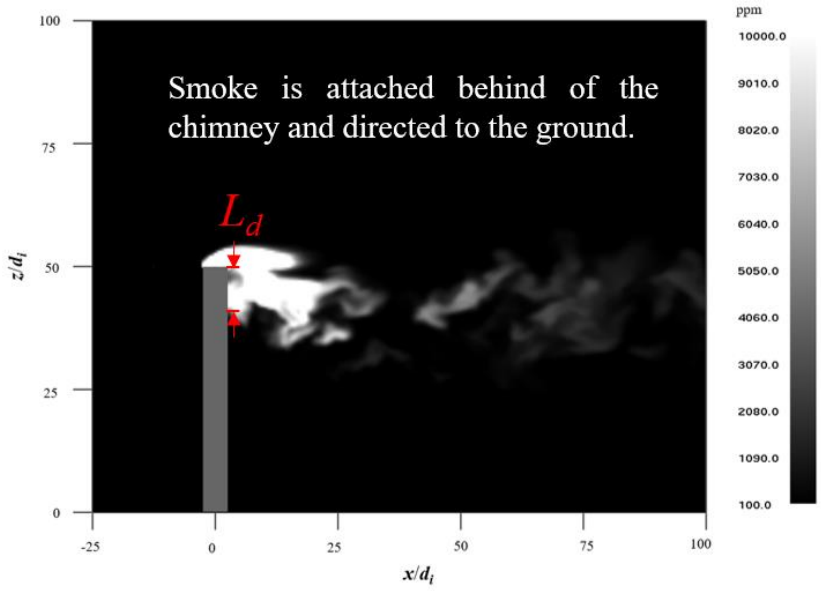

(a) smoke contour

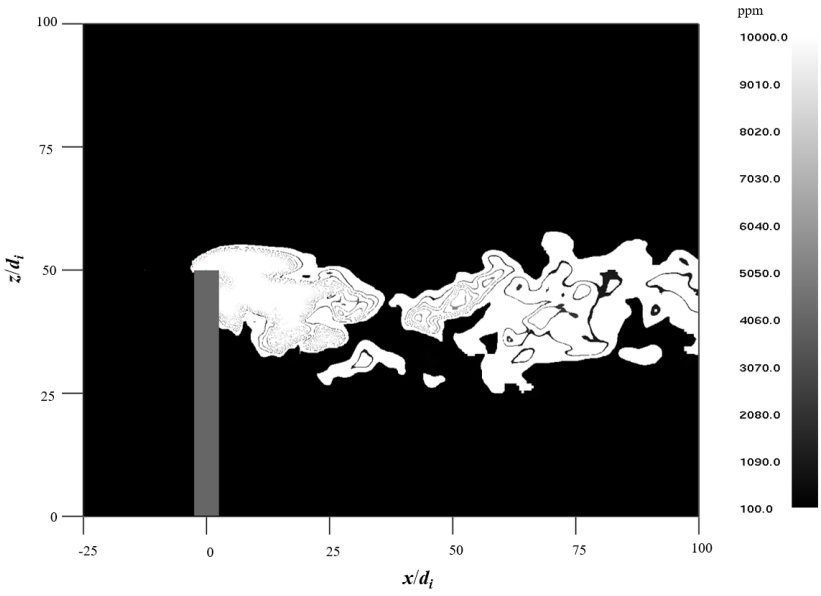

(b) line-smoke contour

U_0 = 1.0 m/s, U_j = 0.5 m/s, $\Delta\theta$ = 0 K

Fig. 5.2 Instantaneous images of smoke ejected from the chimney showing representative downwash pattern.

Table 5.2 Occurrence condition of each mode (Mode V and Mode VI (shaded)) in numerical simulation results.

		preheated level, $\Delta\theta$ = 0 K						preheated level, $\Delta\theta$ = 200 K						preheated level, $\Delta\theta$ = 500 K						
		jet velocity at the top of the chimney exit, U_j [m/s]						jet velocity at the top of the chimney exit, U_j [m/s]						jet velocity at the top of the chimney exit, U_j [m/s]						
		0.5	0.6	0.8	1.0	1.2	1.4	0.5	0.6	0.8	1.0	1.2	1.4	0.3	0.5	0.6	0.8	1.0	1.2	1.4
mean wind velocity, U_0 [m/s]	0.3	VI	V	V	V	V	V	V	V	V	V	V	V	V	V	V	V	V	V	V
	0.4	VI	VI	V	V	V	V	V	V	V	V	V	V	V	V	V	V	V	V	V
	0.6	VI	VI	V	V	V	V	V	V	V	V	V	V	V	V	V	V	V	V	V
	0.8	VI	VI	VI	V	V	V	VI	V	V	V	V	V	VI	V	V	V	V	V	V
	1.0	VI	VI	VI	VI	VI	V	VI	VI	VI	V	V	V	VI	VI	V	V	V	V	V

5.3.2 Critical condition for the appearance of downwash pattern (Mode VI)

As presented in Table 5.1 and Table 5.2, it is found that transition criteria between two modes in this study are equally affected by the buoyancy of smoke (driven by the preheated of the jet), inertia force of smoke (namely, jet velocity) and inertia force of wind (namely, cross-wind velocity). Therefore, Figure 5.3 replots the transition boundary between Mode V and Mode VI to show the transition boundary is a clearer manner. The boundary for all conditions studied in the present experiment in the physical plane is summarized. This plane consists of two velocities in the present system, namely, the jet velocity at the top of the chimney exit, and the cross-wind velocity, respectively. It is found that the qualitative trend of the transition boundary between Mode V and Mode VI for each preheated condition seems identical irrespective of the imposed preheated conditions and a relatively fair agreement is found between the experimental and numerical simulation results, suggesting that the combination of two velocities (U_j and U_0) might be responsible to determine the criteria of the appearance of downwash pattern. In this way, it can be suggested that there is empirical scaling law. However, it is difficult to figure out the physics on this observed fact. Obviously, the scaling law cannot be drawn via attempt to introduce the simple curve fitting (as example, exponential curve fit was adopted in Fig. 5.3). Hence, physical consideration is demanded. Thus, an attempt to introduce the physical consideration to derive the potential scaling law based on law approach (Saito and Williams, 2015) would be valuable which the concept is added in the appendix C. The following section tries to obtain the scaling law to identify the downwash smoke pattern in the observed range.

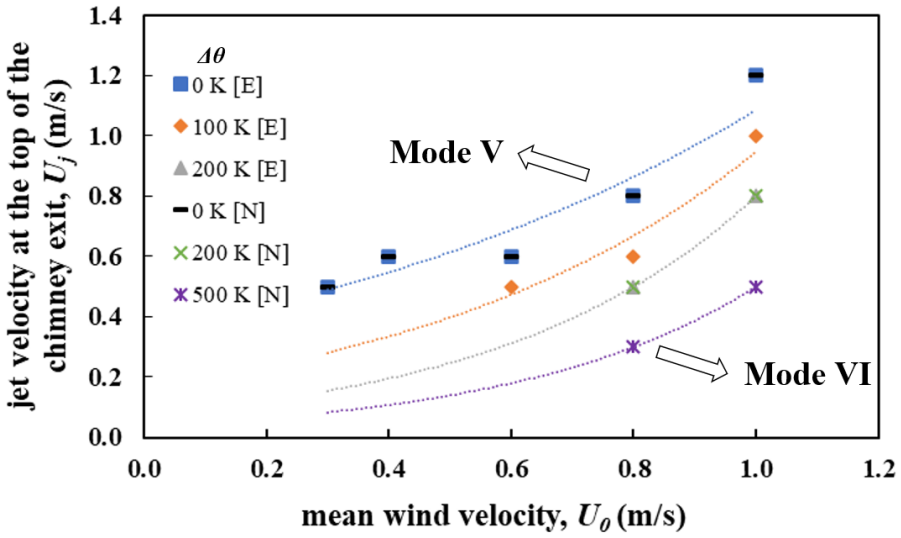

[E] experiment; [N] numerical simulation

Fig. 5.3 Summary of the transition boundary to appear as Mode V and Mode VI using U_j and U_0 in the experiment and the numerical simulation.

5.3.3 Scaling law to provide boundary for the appearance of downwash pattern (Mode VI)

To start to derive the scaling law instructed by Emori's law approach which the concept is added in the appendix C, a potential force to characterize the smoke dynamics shall be considered in the first place. Referred by the observed facts by the experiment, the potential force to characterize the smoke dynamic patterns is depicted as shown in Fig. 5.4.

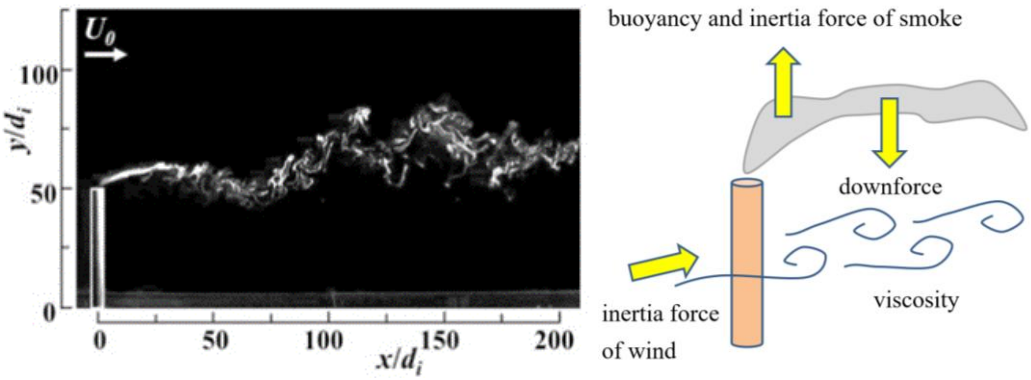

Fig. 5.4 Potential forces.

Assuming that the observed smoke pattern appeared in 2-D (***x***-***y***) plane, there are two directions of force to characterize it. Suppose that there is no backflow against the main flow direction (left to right in this figure). The main force to derive the *x*-direction of the smoke flow shall be the wind inertia force. On the contrary, the *y*-direction of the smoke flow is affected by either upward or downward forces. Jet (smoke) inertia force and jet (smoke) buoyancy are the candidates for the upward force, while the negative pressure induced by the chimney may cause the downward force because the downwash appears immediately behind the chimney. Considering the fact that Reynolds number defined by the mean flow velocity in the cross-wind and the outside diameter of the chimney is less than 2300 under the condition considered in this study, a vortex that appeared in the post-chimney zone is one of the candidates as the source of the negative pressure. With this respect, a viscous force induced by the chimney surface would not be immediately eliminated from the candidates of key force to be taken into account to derive the scaling law. Additionally, as described above and our previous chapter, the appearance of Mode VI is insensitive to the adopted turbulent condition (the range to the appearance of Mode VI is quite similar irrespective when the grid or active turbulence generators were used), suggesting that turbulent characteristics may not be necessary to consider here. Consequently, the following four candidate forces are considered for the law approach.

(1) The buoyancy of smoke (driven by the preheated of the jet), F_b.

(2) The inertia force of smoke (namely, jet velocity at the top of the chimney exit), F_{i_j}.

(3) The inertia force of wind (namely, cross-wind velocity), F_{i_w}.

(4) The viscous force generated by the post-chimney zone, F_v.

Note that there are two inertia forces (by the ejected jet, $F_{i\_j,}$ and the crossflow, F_{i_w}), yet they are nearly the same under the condition studied in this work because the imposed jet/flow velocity is within the same range and only a single characteristic length scale (as chimney outside diameter) is considered. Hence, assume that the inertia force of smoke is equal to the inertia force of wind, $F_{i\_j} \sim F_{i\_w}$. There are then three independent forces to conform two non-dimensional numbers, such as pi-numbers, namely,

$$\Pi_1 = F_b/F_{i\_j} \tag{5.1}$$

$$\Pi_2 = F_{i\_w}/F_{i\_j} \sim 1 \tag{5.2}$$

$$\Pi_3 = F_v/F_{i\_j} \sim F_v/F_{i\_w} \tag{5.3}$$

It is known that Π_1 is the inverse of Froude number ($\Pi_1 = F_{i\_j}/F_b = Fr$) and Π_3 is the inverse of Reynolds number ($\Pi_3 = F_{i\_w}/F_v = Re$). Therefore, the jet-Froude number, Fr_j, and the Reynolds number, Re_d, based on the cross-wind velocity are defined as:

$$Re_d = \left(\frac{\rho U_0 d_o}{\mu}\right) \tag{5.5}$$

$$Fr_j = \left(\frac{U_j^2}{2g\sqrt{A_j/\pi}(T_a/\Delta\theta)}\right)^{1/2} \text{ (Canepa et al., 2004)} \tag{5.6}$$

Where, U_0 is the mean wind velocity, d_o is the characteristic length scale (outside diameter of the chimney), ρ is the ambient air density, μ is viscosity of the ambient air, U_j is the jet ejecting velocity from the chimney exit, g is the gravity acceleration, A_j is area of chimney outlet, T_a is the ambient temperature, and $\Delta\theta$ is the temperature difference between hot jet and ambient. Note that the Reynolds number, Re_d, determines the nature of flow around the chimney, defined by the characteristic of cross-wind velocity and characteristic length of chimney's outside diameter. Also note that the term of non-dimensional temperature difference, ($T_a/\Delta\theta$), in Eq. (5.6) inversed compared with the equation in the reference (Canepa et al., 2004) is applied properly in this work. The verification is confirmed in the wide range of temperature difference testing data in the numerical simulation, ranging at $\Delta\theta$ = 0–500 K, which the present experiment tested condition is limited. Note that the jet velocity from the chimney of U_j = 0.3 m/s is conducted in the case of temperature difference of $\Delta\theta$ = 500 K for getting more results of the appearance the downwash pattern to support the proposed the scaling law.

In order to check whether these two pi-numbers work to identify the boundary of Mode V and Mode VI observed in the experiment, data plots in Fig. 5.3 are summarized in Fig. 5.5 with a logarithm plane. For comparison, other data plots taken from reference (Canepa et al., 2004) and numerical simulation are also included. According to previous work of Canepa et al. (2004), smoke downwash shall appear when $Fr^2 \geq 3$, and the jet velocity at the top of the chimney exit is less than or equal to the mean wind velocity ($U_j \leq U_0$). It is shown that the transition boundary between the two modes moderately fits the single line, suggesting that the boundary can be summarized by the coupling effect due to the competition of the buoyancy of the smoke, (driven by the preheated of the jet), the inertia force of the smoke (jet velocity at the top of the chimney exit), and the inertia force of the wind (cross-wind velocity), suggesting that

the jet-Froude number and Reynolds number can determine in general way to describe the boundary condition to appear Mode VI. In addition, it is found that with the increase in the Reynolds number, the appearance of Mode VI became higher; conversely, with the increase jet-Froude number, the appearance of Mode VI became lower. Furthermore, the figure clearly reveals that all data plots are satisfactory falling into single line, whose gradient is 0.80, suggesting there would be certain physics to be a source of mode separation depending on both Re_d and Fr_j, and interestingly, the criteria suggested by the past work (Canepa et al., 2004) follow the proposed line as shown in Fig. 5.5. However, it is important to note that the suggested criteria by Canepa et al. (2004) are only available for preheated conditions since it requires $Fr^2 \geq 3$. In this sense, the present boundary expression is more feasible and universal to predict the critical condition for the appearance of the downwash pattern (Mode VI) as compared to the one proposed in the past work (Canepa et al., 2004). The present boundary expression could cover in the actual smoke temperature according to on previous research point out that in power plants the gases leave the stacks with temperature from 120 ^{o}C to 190 ^{o}C (Sherlock and Lesher, 1954) or around 150 ^{o}C to 250 ^{o}C (Michael, 2021). Moreover, the observed data seems fit into the single line, whose exponent is 0.80, suggesting that there are certain physical explanations to satisfy this exponent number (though it is still an open question at present). Additional efforts are necessary to prove the feasibility of the relationship between Fr_j and Re_d to bound two modes and go deeper. As noted, the data shows relatively large fluctuation (not organized well), and the covered range is not wide enough. Thus, a numerical approach is preferable, allowing to perform the numerical experiment in order to identify the universal scaling law in an efficient manner.

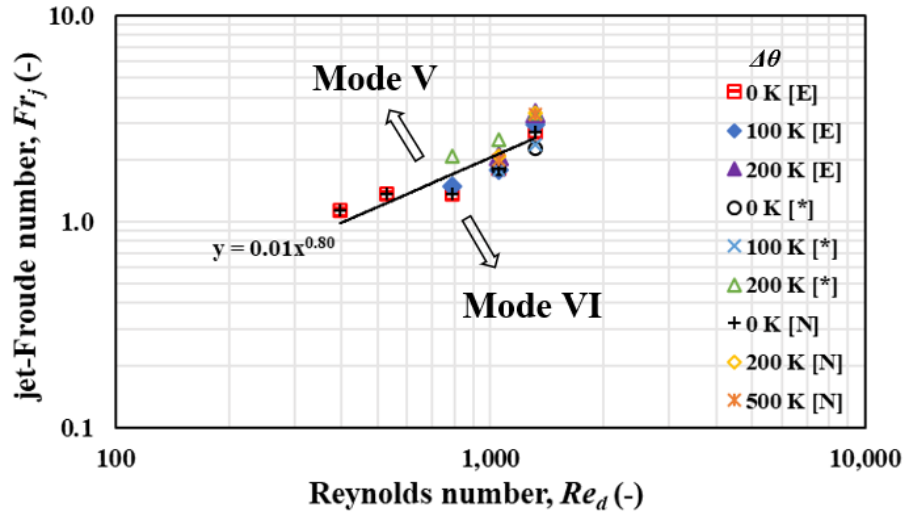

[E] experiment; [*] Canepa et al., 2004; [N] numerical simulation

Fig. 5.5 Jet-Froude number versus Reynolds number of the transition boundary of Modes V and VI. Data from Canepa et al. (2004) and numerical simulation are also added to support the proposed scaling law.

The present work is successful to predict the appearance of downwash pattern of the smoke from the chimney in the actual atmospheric boundary layer using the atmospheric wind tunnel with the active turbulence grid (namely, quasi-isotropic turbulence), namely, it could contribute the prevention of dangerous situation by determining in advance effluents could cause a high concentration of harmful effluents in a particular area. However, through this work, although it seems that there is concrete scaling law in the present work, it should be concerned whether the proposed scaling law is more universal or more conditional. For instance, this study only focused on the range of Π_2~1 as stated in Eq. (5.2) and the results are obtained by using the single chimney size (no dependency on the characteristic length is taken into account). Indeed, supposing that the actual scale of the chimney (because the characteristic length of the chimney (its diameter) is in order of meters) is considered, jet Reynolds number becomes extremely larger, suggesting that the viscosity force is relatively negligible. Other forces may be needed to drive the downward force instead of the negative pressure generated by the vortex. To confirm this issue, working on a wide range of testing data is demanded to verify the potential scaling law, which will be also the focus of the future work. As suggested, numerical approach would be valuable on this regard. This technique which is based on the numerical models can be more advantageous than the experimental methods in many ways, such as the richness of the quantitative results, low cost, and rapid turnaround time. For instance, we could increase wide

ranged of the cross-wind velocity and jet velocity, changed the size and shape of the chimneys to investigated on this regards (for future work). Due to limited time, our work could not be accomplished in wide range of tests, consequently, the wide range of testing is still demanded to verify the potential scaling law, which will be also the focus of the future work.

5.4 Concluding remarks of this chapter

This study experimentally and numerically investigated the smoke behavior ejected from the chimney into the cross-wind and elucidated the critical condition for the appearance of the downwash pattern. It was found that inertia force of wind, the buoyancy of smoke, the inertia force of smoke, and the viscous effect around the chimney were equally responsible for the appearance of the downwash pattern. Such experimental and numerical facts were considered to propose the potential scaling law, $Fr_j \propto Re_d^{0.80}$, where Fr_j stands for the jet-Froude number and Re_d stands for Reynolds number defined by characteristic length scale on chimney's outside diameter. Although further verification on a wide range of testing data was needed, this proposed scaling law worked well to describe the critical condition of the appearance of the downwash pattern under the condition studied in the present work.

CHAPTER 6
NUMERICAL STUDY ON THE DOWNWASH PATTERN

6.1 Introduction and objective of this chapter

As point out in the Introduction section on Chapter 1, an understanding of the physical principles of pollutant's motion and dispersion is highly demanded in order to determine the impact of air pollution on the environment and humans. Several environmental standards have been set to reduce or immigrate concentrations of pollutants including smoke in atmosphere and in the emissions from the chimneys. From fundamental point of view, this problem is regarded as the turbulent conditions in the atmosphere including smoke ejected from the chimney. This is because the smoke released from the chimney is transported by wind and diffused by turbulent conditions in the atmosphere. Furthermore, although the meandering smoke pattern has been often observed in the actual phenomena, it has been hardly seen in the laboratory scale experiment using the wind tunnel (Canepa, 2004; Gnatowska, 2015; Sekishita et al., 2019;). As expected, designing the real-scale experiment on this subject is quite difficult task because we have no way to control the natural wind. The meandering and downwash modes, which are quite important to predict the smoke dispersion and direct exposure to cause health damage (Canepa, 2004; Gnatowska, 2015; Huang and Hsieh, 2002; Overcamp, 2001; Sekishita et al., 2019), however, it is unfortunate that the boundary of smoke behavior is not very clear and not systematically determined. Therefore, downwash mode of smoke dispersion is of interest because it contributes to the understanding of the processes that case pollution problems. On this regard, the interpretation of the phenomena has been further made with the numerical approach to gain more detailed physics with the insightful understanding from scientific way. That is to say, it can contribute the prevention of dangerous situation by determining in advance effluents could cause a high concentration of harmful effluents in a particular area. Consequently, the main objective of this chapter is to investigate the reason how the downwash occurs from the chimney to provide a mean of predicting the presence of downwash resulting from the wake due to the chimney. To understand the effect of imposed turbulent characteristics onto the observed downwash pattern, the results using the Fire Dynamics Simulator (FDS) with certain turbulence intensity is revealed the quasi-isotropic turbulence effects on the smoke behavior from the chimney.

6.2 Numerical method and model configuration

A brief explanation is made here for numerical setup. This is because the main configuration of numerical simulation is similar to what already explained in section 3.2. The numerical simulations are performed using the fire dynamic simulator (FDS) software. FDS, as a computational fluid dynamics model for fluid flow, is used to investigate the dispersion characteristics for such a scenario, as now a popular CFD tool in fire related research, as well as used to simulate the concentration and flow distribution in the chimney. FDS presents a simple turbulence model based on the technique of LES which is built on a good approximation of equations for the low Mach number. The numerical simulations are performed using FDS in the test section tunnel of 0.5 m of length as shown in Fig. 3.6. The cross section of test section tunnel is rectangular with 0.2 m of width and 0.4 m of height.

The chimney model with an inside diameter of d_i = 4 mm, an outside diameter of d_o = 20 mm, and a height of h = 200 mm, was placed on the floor of the wind tunnel test section. The present simulations were carried out as same in the experimental conditions of temperature difference between the cross-wind and the jet from the chimney, ranging at $\Delta\theta$ = 0–500 K, the jet velocity at the top of the chimney exit, ranging at U_j = 0.5–1.4 m/s, and the mean velocity of the cross-wind, ranging at U_0 = 0.3–1.0 m/s. Turbulence intensity, u_{rms}/U_0, is set about 10.25% to produce the quasi-isotropic turbulence fields.

6.3 Results and discussion

6.3.1 Flow characterization

Flow visualizations were performed using Fire Dynamics Simulator (FDS), Large Eddy Simulation (LES), to investigate the reason how the downwash pattern occurs from the chimney under certain numerical conditions. A detailed observation of the smoke behaviors ejected from the chimney in the crossflow was conducted. In order to understand the effect of freestream turbulence on the downstream fields, it is necessary to characterize the incoming flow in turbulence resolution on the initial boundary condition in the velocity fields. The mean wind velocity measurements upstream of the test section of wind tunnel simulation were taken for different wind velocities. The mean wind velocity displayed in Fig. 6.1 (a) shows a uniform flow profile across the tunnel height in downstream fields in the quasi-isotropic turbulence case as closed to the experimental results as shown in the Fig. 3.6. The turbulence intensity profile is shown in the Fig. 6.1 (b). The turbulence intensity profile of the crossflow is uniform in the

quasi-isotropic turbulence case. The turbulence resolution on the initial boundary condition of velocities before and after the chimney location of the mean wind velocity of U_0 = 1.0 m/s is shown in Fig. 6.2. The fluctuation of mean wind velocity in the quasi-isotropic turbulence is high in both before and after the chimney locations. It indicates that the level turbulent in the quasi-isotropic turbulence of wind velocity field is high. This result reveals to convince that the initial condition inputted in the FDS is corrected to reproduce the turbulence structure which could attained at satisfactorily realistic turbulence characteristics in the natural of the actual large-scale turbulence fields referred to previous research of Makita (Makita, 1991).

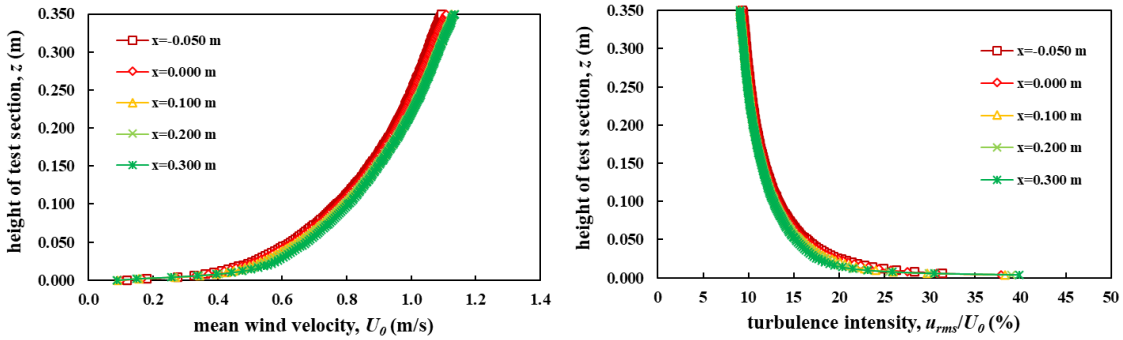

(a) (b)

Fig. 6.1 Vertical mean wind velocity profile and turbulence intensity profile of U_0 = 1.0 m/s.

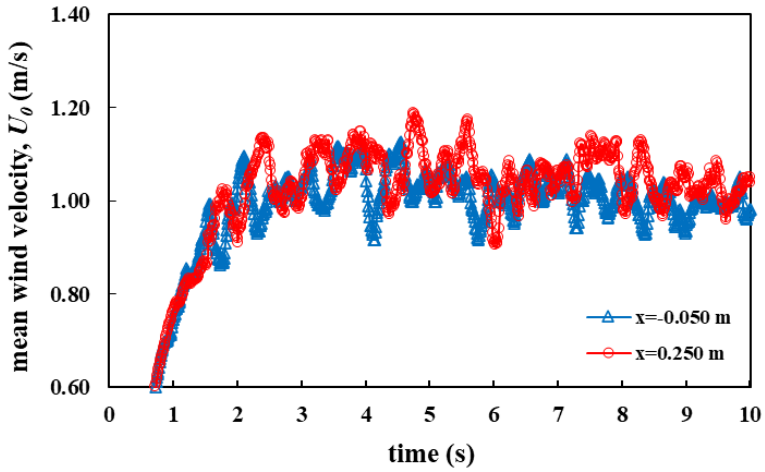

Fig. 6.2 Turbulence resolution on the initial boundary condition in the mean wind velocity fields of U_0 = 1.0 m/s.

6.3.2 Downwash pattern (Mode VI)

As presented in Fig. 5.2, the downwash pattern is the phenomenon in which the smoke from the chimney is drop down into low-pressure region in the wake of the chimney which caused by low-speed zones appear at the behind of the chimney. The representative image on the mean wind velocity field of cross-wind and pressure filed of cross-wind in the quasi-isotropic turbulence case are shown in Fig. 6.3 and Fig. 6.4, respectively. Complex flow behaviors are the results of the interactions between the downwash effect, which is induced by turbulent crossflow passing over the chimney exit, the up-shear effect induced by the issuing smoke, and the wakes behind the smoke and the chimney as shown in Fig. 6.3 of (a) velocity contour, (b) line-velocity contour, and (c) velocity vector. As the wind flow past the chimney, it generates turbulence in the wake of the chimney which cause of the appearance of the downwash. A counter-rotating vortex pair is observed above the chimney referred by the observed facts in the experiment as shown in the Fig. 5.4. The left-side and right-side vortices rotate in a clockwise and counter-clockwise directions, respectively, similar to the tip vortices formed along the leading edge of a delta wing at incidence. The two vortices are of similar size and are nearly symmetric with respect to the central plane of the wake. The counter-rotating twin-vortex is formed by the roll-up motion of the shear flow separated from the edges of the chimney. After separating from the chimney, the flow descends along the central section of the wake. The size of the swirling vortices increases at the downstream, the vortices expand laterally and move slightly downwards. This is caused by the entrainment of ambient fluids.

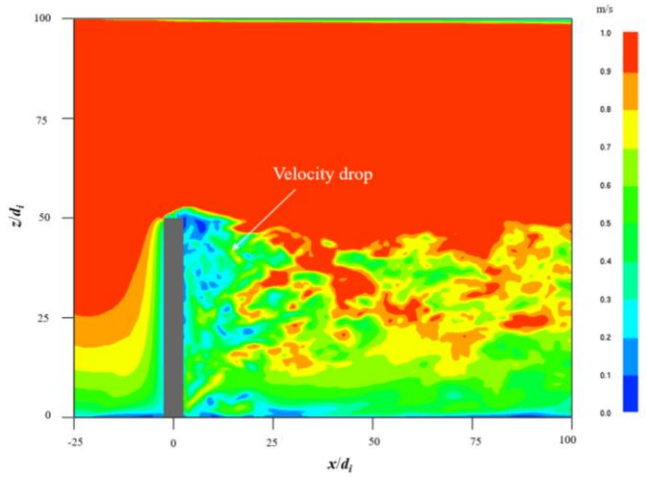

(a) velocity contour

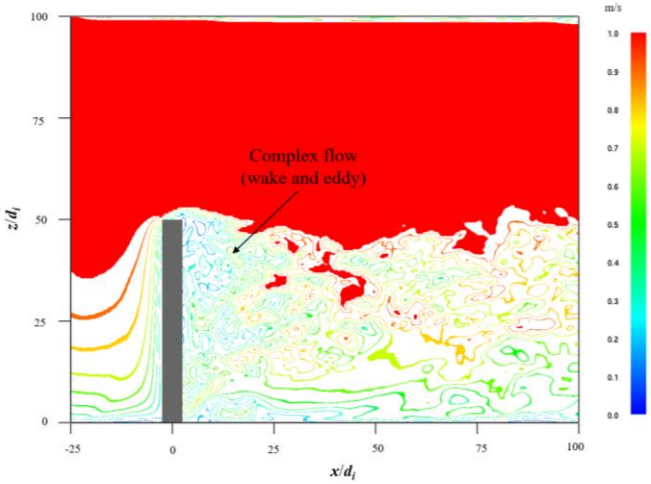

(b) line-velocity contour

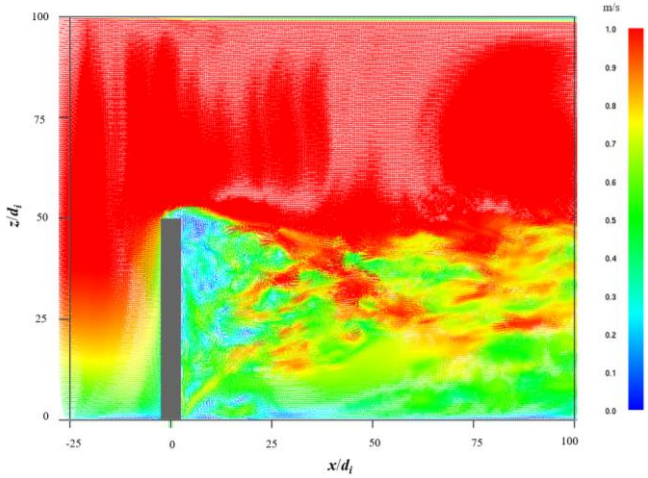

(c) velocity vector

U_0 = 1.0 m/s, U_j = 0.5 m/s, $\Delta\theta$ = 0 K

Fig. 6.3 Instantaneous image of mean velocity field in the quasi-isotropic turbulence.

The downwash flow caused by the counter-rotating vortices interacts with the vortices shed from the two sides of the chimney in the upper half of the near-wake region. If the smoke emitted by the chimney come under the influence of the turbulence generated by the chimney, the smoke may be brought down and penetrate the vortex sheath so that they are brought to the ground by the turbulence behind the chimney. This reveals that the jet inertia force is not large enough to sustain the impingement and the shear of the transverse stream so that it is deflected through a large angle from the vertical axis of the chimney. Most of the smoke particles emitted from the chimney are entrained into the wake. A little portion of the jet fluids goes downstream. The downwash area is enclosed in a dividing streamline, which separates the reverse and forward flows into the low-pressure region in the chimney wake. Under such conditions the concentrations of obnoxious constituents of the smoke on the ground may be very high in the area close to the source of emission. In general, the downwash will be used to designate that condition in which the bottom of the smoke has been forced by aerodynamic causes to descend below some specified height within a downstream distance from the chimney.

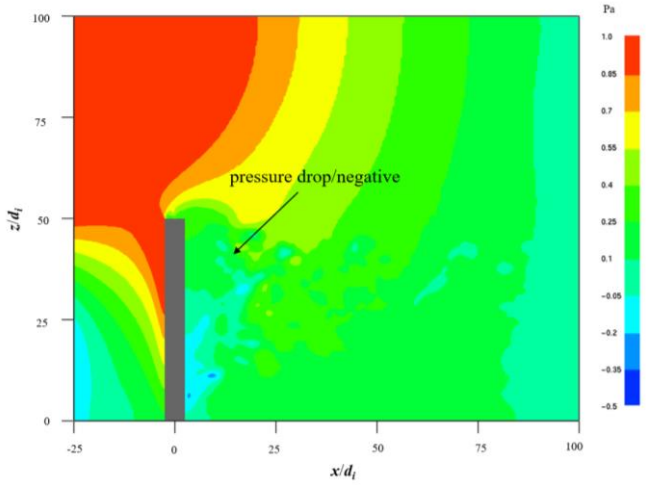

U_0 = 1.0 m/s, U_j = 0.5 m/s, $\Delta\theta$ = 0 K

Fig. 6.4 Contours of pressure field.

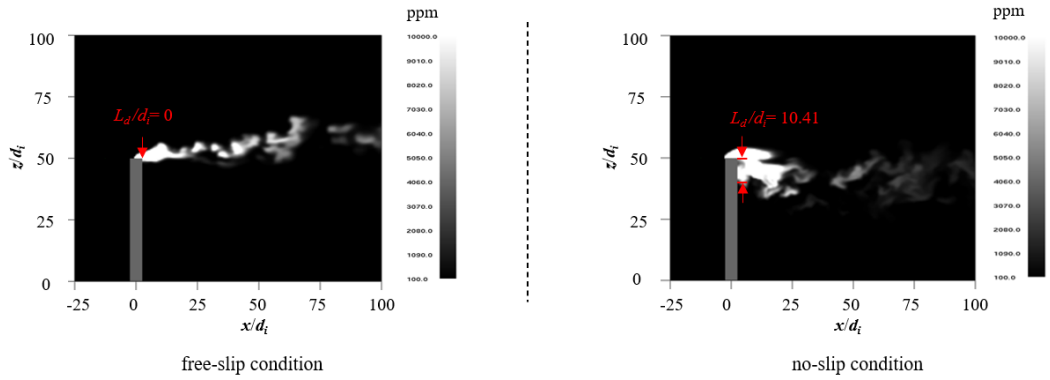

smoke contour

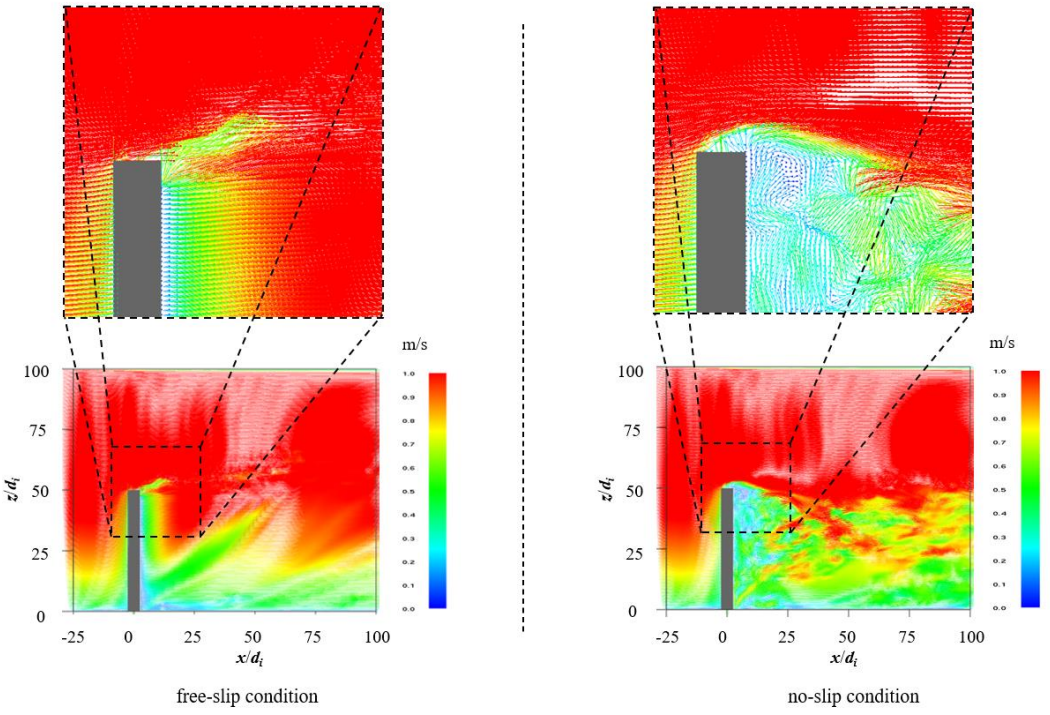

velocity vector

(a) (b)

U_0 = 1.0 m/s, U_j = 0.5 m/s, $\Delta\theta$ = 0 K

Fig. 6.5 Instantaneous images of smoke ejected from the chimney showing representative the boundary conditions of the chimney.

As pointed out in the results of chapter 5 that the vortex and the viscous effect around the chimney are important role for the appearance of the downwash pattern, Fig. 6.5 and 6.6 show the results for validation. To avoid the generation of vortex of the chimney, Fig. 6.6 shows the boundary conditions of the outside surface of the chimney effect on downwash pattern in the smoke contour field and velocity vector field. Fig. 6.5 (a) is free-slip condition of the outside surface of the chimney and Fig. 6.5 (b) is no-slip condition of the outside surface of the chimney. It is found that when the outside surface of the chimney setting in the free-slip condition, the downwash does not occur. In the other hand, the downwash occurs in the case of the outside surface of the chimney setting in the no-slip condition. Due to the no-slip condition of the outside surface of the chimney, the inertia force of wind will have zero relative to the boundary outside chimney surface. As indicated in the Fig. 6.5 (zoom image) of velocity vector, when the wind flow past the chimney, it generates turbulence in the wake of the chimney which cause of the appearance of the downwash. This means that the vortex of the chimney plays a role on the appearance of the downwash pattern. In addition, to avoid the generation of vortex of the chimney and viscous effect around the chimney, Fig. 6.6 shows the smoke ejecting on the top of the chimney effect on downwash pattern in the smoke contour field and velocity vector field. Fig. 6.6 (a) is free-slip condition and Fig. 6.6 (b) is no-slip condition. It shows that the downwash does not occur in these cases. This result is proved that the viscous effect around the chimney plays a role on the appearance of the downwash pattern.

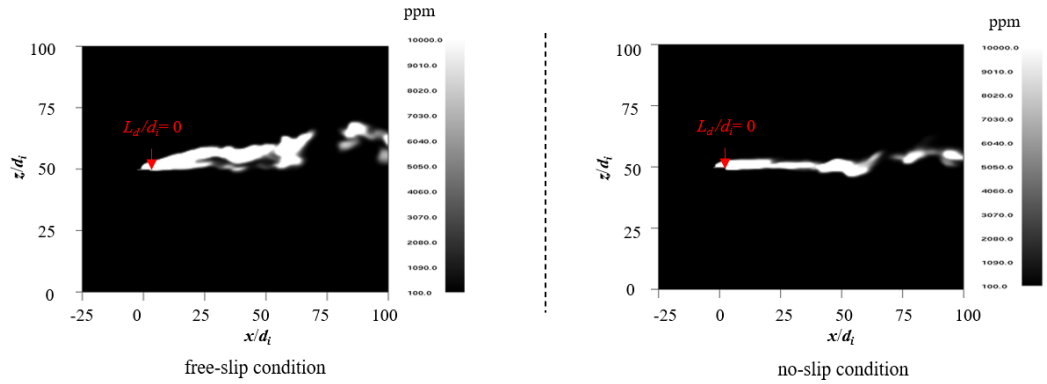

smoke contour

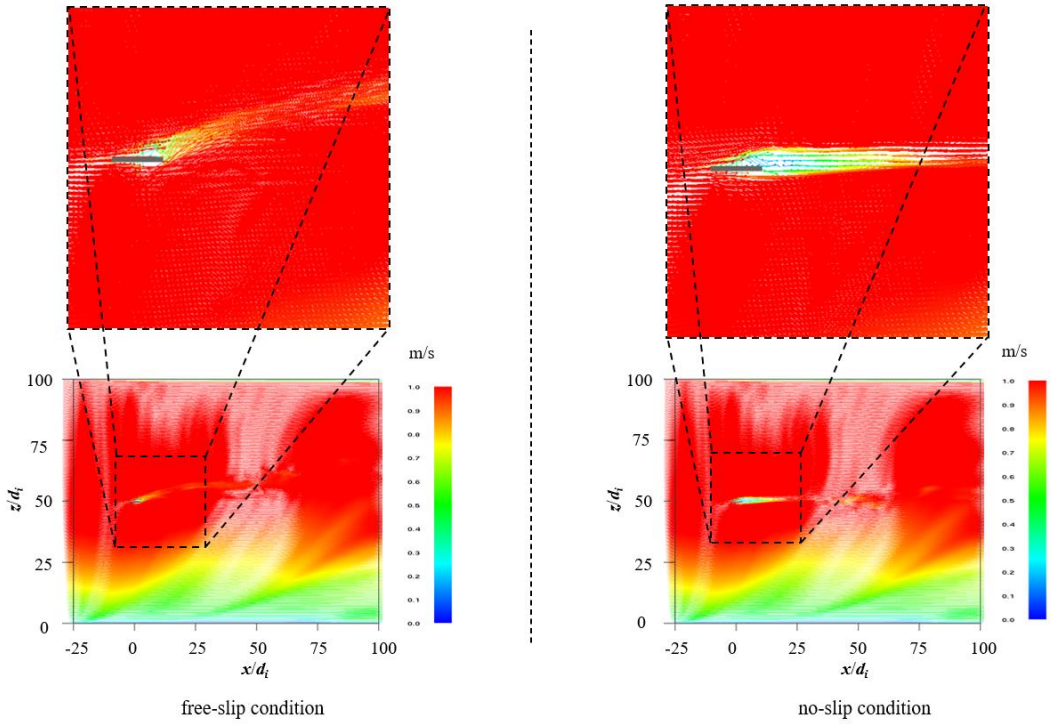

velocity vector

(a) (b)

U_0 = 1.0 m/s, U_j = 0.5 m/s, $\Delta\theta$ = 0 K

Fig. 6.6 Instantaneous images of smoke ejected from the top of chimney showing representative the smoke dispersion.

6.3.3 Inertial force, buoyancy force, and chimney height effect on the downwash pattern

As pointed out in the results of chapter 5 that inertia force of wind, the buoyancy of smoke, and inertia force of smoke were equally responsible for the appearance of the downwash pattern, these results show the validation. Figure 6.7 represents the influence of inertial force due to the mean wind velocity on the smoke released from the chimney in the quasi-isotropic turbulence. Fig. 6.7 (a) shows the smoke contour field and Fig. 6.7 (b) shows the smoke vector field. When the ratio of the jet velocity to the mean wind velocity of the wind tunnel decreases, the smoke curves until it becomes almost horizontal to the ground as shown in the Fig. 6.8. As indicated in the Fig. 6.7 (b) of smoke vector field (zoom image), when the cross-wind velocity past the chimney increases (the ratio of the jet velocity to the mean wind velocity of the wind tunnel decreases), it generates high turbulence in the wake behind the chimney which cause of the appearance of the downwash. This visual display allows us to observe that the ambient flow greatly affects the smoke flow, the main factor determining the smoke behavior being the inertial force of wind velocity. This result agrees with previous research by Said et al. (2005). The downwash pattern appears under the condition of a high cross-wind velocity and a low jet velocity. The downwash pattern occurs if the ratio of jet velocity to mean wind velocity is less than 1 ($U_j/U_0 \leq 1$) in the quasi-isotropic turbulence. Although, previously, Sherlock and Stalker (1941), Briggs (1973) pointed out that the downwash would not occur in the range $U_j \geq 1.5\ U_0$, namely, the ratio of the jet velocity to the mean wind velocity should be greater than 1.5 to avoid downwash pattern. However, this is true irrespective of the imposed inlet turbulent conditions especially the quasi-isotropic turbulence. In addition, Snyder and Lawson (1991) stated that downwash from non-buoyant jets occurs if the speed ratio is less than about 1.5 in the subcritical regime (light wind) and about 1.1 in the supercritical regime (strong wind). When the ratio of the jet velocity to the mean wind velocity decreases, it is accompanied by more rapid entrainment ambient air into the smoke. This suggests that the inertial force due to the cross-wind velocity effects on downwash pattern. In addition, this result also allows us to observe that the mean wind velocity and atmospheric conditions greatly effect of the smoke behaviors. In the other hand, Fig. 6.9 represents the influence of inertial force due to the jet velocity from the chimney on the smoke ejected from the chimney. Fig. 6.9 (a) shows the smoke contour field and Fig. 6.9 (b) shows the smoke vector field. When the ratio of the jet velocity to the mean wind velocity of the wind tunnel increases, the smoke curves rise with an increase of the downstream

distance as shown in the Fig. 6.10. This suggests that the inertial force due to the jet velocity from the chimney effects on downwash pattern. The inertial force of the jet velocity from the chimney plays a role to prevent the appearance of the downwash pattern.

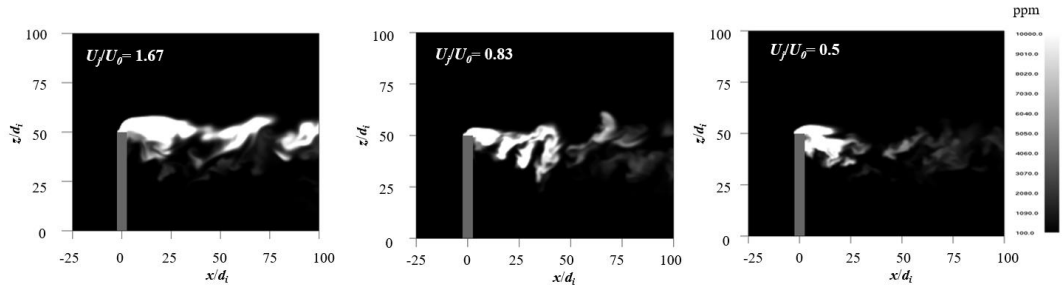

(a) smoke contour

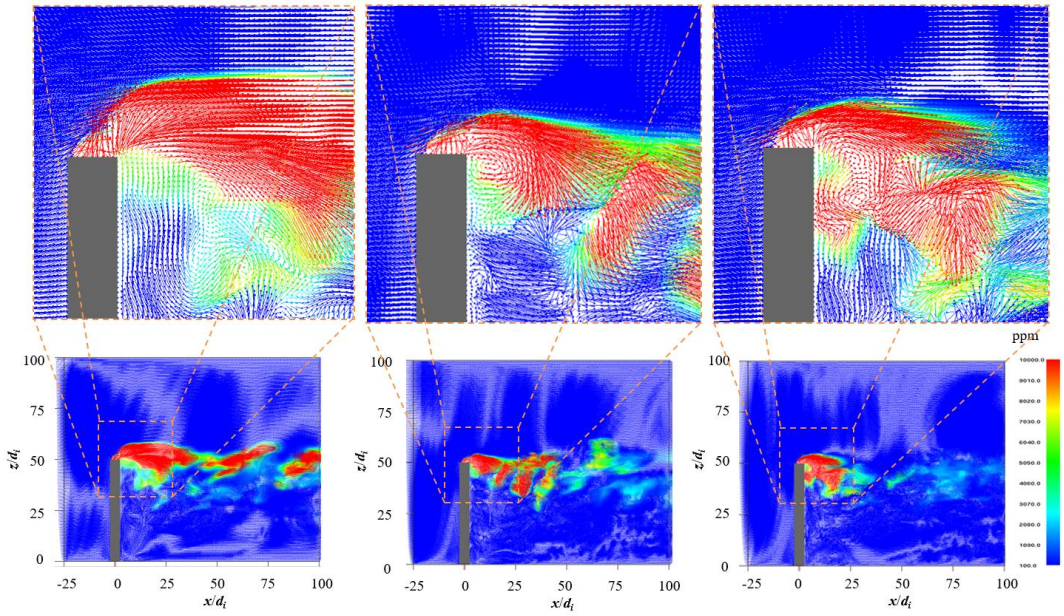

(b) smoke vector

U_j = 0.5 m/s, $\Delta\theta$ = 0 K

Fig. 6.7 Instantaneous image of influents of inertial force of cross-wind on the smoke flow.

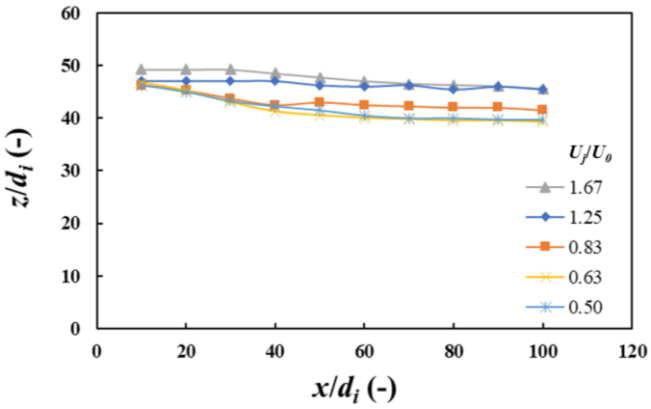

U_j = 0.5 m/s, $\Delta\theta$ = 0 K

Fig. 6.8 Influents of inertial force of cross-wind on the smoke flow center.

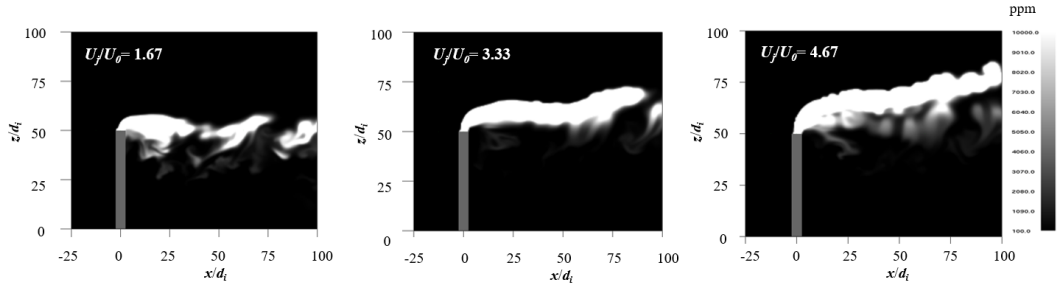

(a) smoke contour

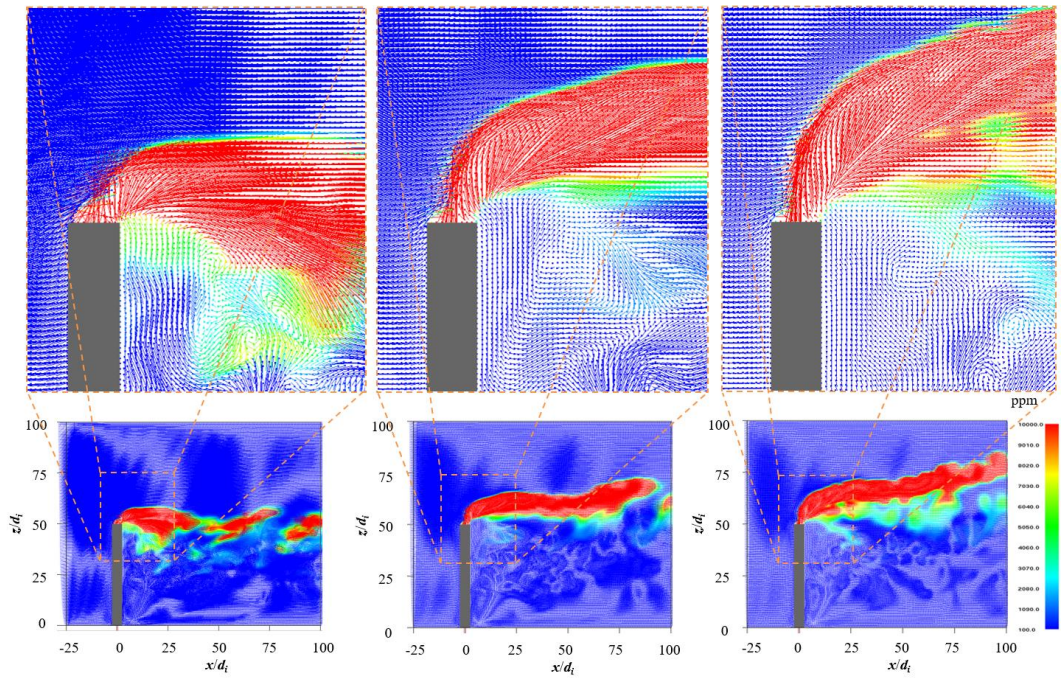

(b) smoke vector

U_0 = 0.3 m/s, $\Delta\theta$ = 0 K

Fig. 6.9 Instantaneous image of influents of inertial force of jet velocity on the smoke flow.

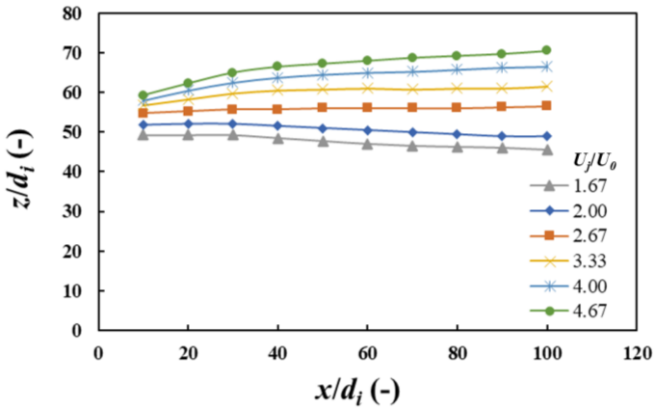

U_0 = 0.3 m/s, $\Delta\theta$ = 0 K

Fig. 6.10 Influents of inertial force of jet velocity on the smoke flow center.

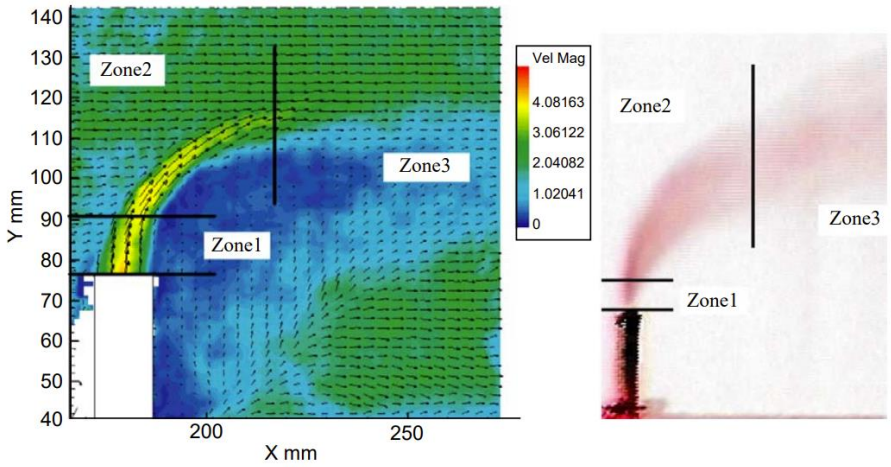

Fig. 6.11 Different region of the plume evolution (Said et al., 2005).

In addition, this result could observe the geometric characteristics of the deflected smoke plume and relatively fair agreed with previous research of Said et al. (2005). As referred from Said et al. (2005) (shown in Fig. 6.11), the Fig. 6.7 (b) and Fig. 6.9 (b) are presented the different region of the smoke plume evolution. The region of smoke plume evolution is defined in three zone. In the first zone, the plume dominated the flows. In the second zone the ejection velocity is equal to the crosswind. In this zone the plume begins to bend. In the third and last zone, the crossflow is dominated, and the flows are carried to the chimney wake. When the ratio of the jet velocity to the mean wind velocity of the wind tunnel is greater than 1, it is possible to distinguish the three phases of the smoke plume evolution within the surrounding environment. In the other hand, when the ratio of the jet velocity to the mean wind velocity of the wind tunnel

is less than 1, the first two phases can no longer be observed. The smoke plume flows only within the wake formed the chimney which is induced by the crossflow passing over the chimney exit, the up-shear effect induced by the issuing smoke plume, and the wakes behind the chimney.

Fig. 6.12 and Fig. 6.13 represent the temperature distribution ($\Delta\theta$ = 0 K, $\Delta\theta$ = 200 K, and $\Delta\theta$ = 500 K) effects on the smoke downwash. It is showed that with increase in the temperature difference effects on the downwash pattern. When the temperature difference increases, the temperature difference field is widely dispersed as shown in Fig. 6.12 and smoke flow center increases gradually with an increase of the downstream distance as shown in Fig. 6.13. This reveals that the buoyancy force of the smoke due to the preheated of the jet would lift-up the smoke to prohibit to have downwash pattern as pointed out in the chapter 5 which is related to the fact that the hot smoke become lighter in density, resulting in the smoke plume rise is higher.

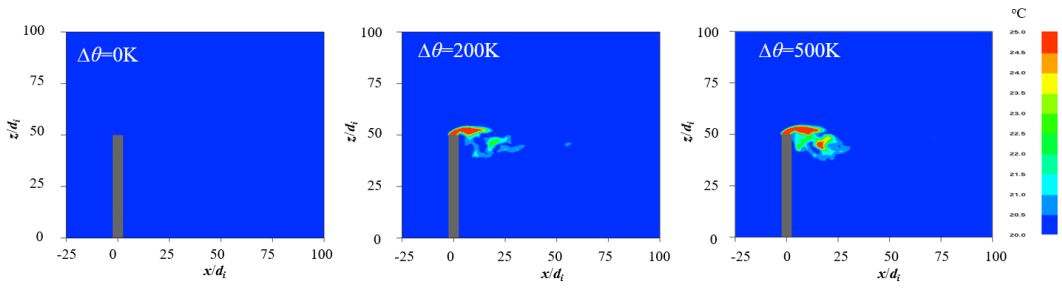

U_0 = 1.0 m/s, U_j = 0.5 m/s

Fig. 6.12 Instantaneous images of temperature distribution effect on the smoke flow.

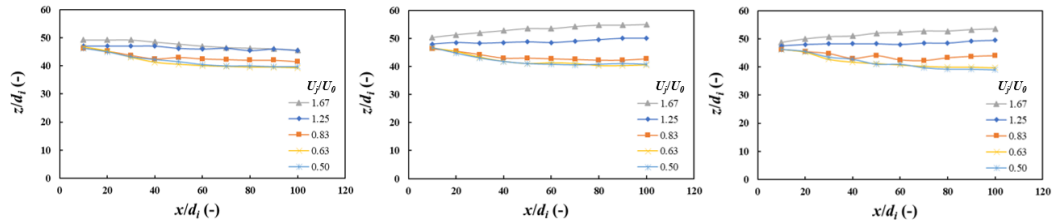

$\Delta\theta$ = 0 K $\Delta\theta$ = 200 K $\Delta\theta$ = 500 K

Fig. 6.13 Influents of inertial force of cross-wind on the smoke flow center, U_j = 0.5 m/s.

Fig. 6.14 represents the chimney height (0.200, 0.250, and 0.300 m) effected on the smoke downwash in the smoke contour (show in Fig. 6.14 (a)) and in the line-smoke contour (show in Fig. 6.14 (b)). It is showed that with increase in the chimney height does not affect much on the downwash pattern. The downwash pattern still occurs even with the increase in the chimney height. Although, previously, Briggs (1969) pointed out that the most enduring rules of thumb for stack design was the recommendation made in 1932 that stacks be built at least 2.5 times the height of surrounding buildings. If such a stack is designed with sufficient efflux velocity to avoid downwash, the plume is normally carried above the region of downflow in the wake of the building. However, this is true irrespective of the imposed the chimney downwash conditions. Nevertheless, the chimney height is the factor to reduce the smoke concentration reach to the ground. The chimney height could increase the clearance length (C) between the smoke dispersion and ground or other obstructions which the smoke diffusion may reduce the concentration of obnoxious constituents of the gases/smoke to within tolerable limits before they reach the ground as shown in the Fig. 6.14 (b). As present in the Fig. 6.15, when the chimney height increases, the clearance length between the smoke dispersion and ground is also increased.

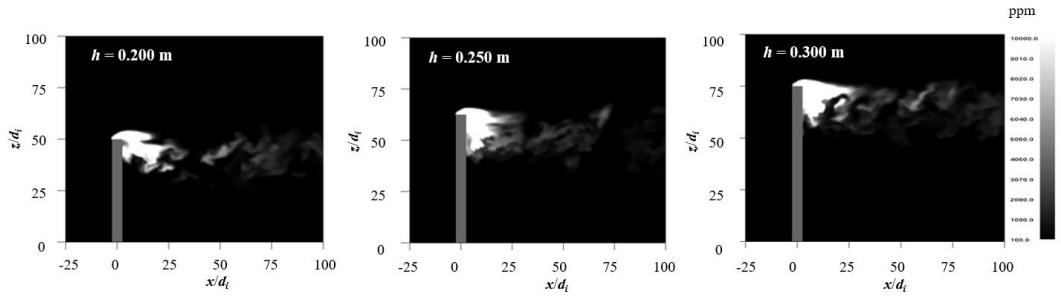

(a) smoke contour

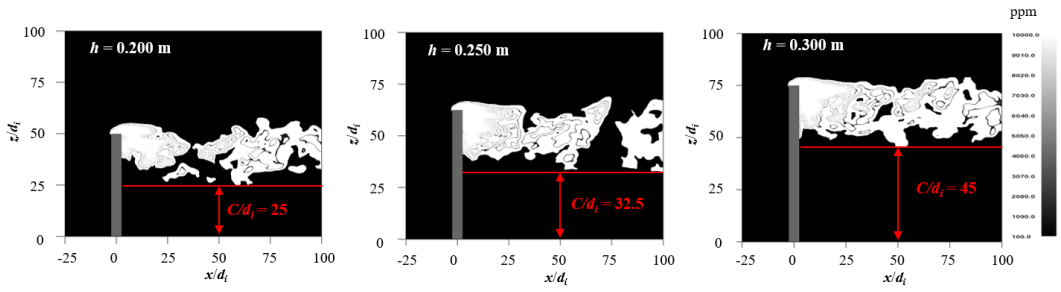

(b) line-smoke contour

U_0 =1.0 m/s, U_j = 0.5 m/s, $\Delta\theta$ = 0 K

Fig. 6.14 Instantaneous images of chimney height effect on the downwash pattern.

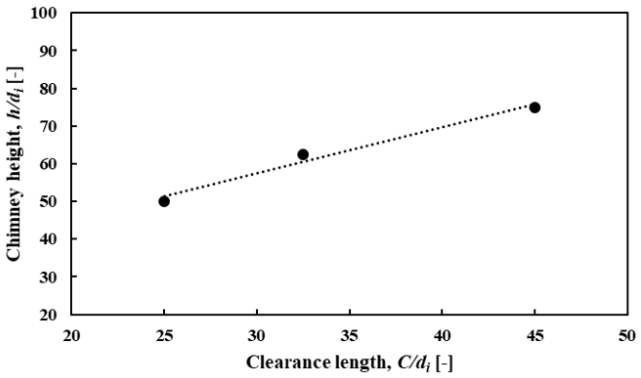

U_0 =1.0 m/s, U_j = 0.5 m/s, $\Delta\theta$ = 0 K

Fig. 6.15 Chimney height versus clearance length.

Based on studied using the numerical simulation, the interpretation of the smoke downwash phenomena is clarified to gain more detailed physics with the insightful understanding from scientific way. This technique which is based on numerical models can be more advantageous than the experimental methods in many ways, such as the richness of the quantitative results, low cost, and rapid turnaround time. The present numerical simulation is successful in the realization of the downwash pattern of the smoke ejected from the chimney which can be observed in the actual atmospheric boundary layer using the fire dynamic simulator (FDS), large eddy simulation (LES). The present numerical results can serve as a reference data for the validation of the numerical study.

6.4 Concluding remarks of this chapter

The numerical simulations were performed using the fire dynamics simulator (FDS) to identify the reason how the downwash pattern occurs of the smoke ejecting from the chimney under certain numerical conditions. The following conclusions were deduced:

(1) The inertia force of wind (wind velocity), the buoyancy of smoke (preheated smoke), inertia force of smoke (jet velocity), and viscous effect around the chimney (boundary of the chimney surface) were equally responsible for the appearance of the downwash pattern, while the chimney height did not affect much on the appearance of the downwash pattern.

(2) The downwash pattern was the phenomenon in which the smoke from the chimney was drop down into low-pressure region in the wake of the chimney which caused by low-speed zones appear at the behind of the chimney. Definition of the downwash condition

was that the high-concentration smoke reaches to the ground level in downstream to cause the potential health damage.

(3) The downwash pattern appeared under the condition of the high cross-wind velocity and the low jet velocity; it means that the inertial force and the turbulent motion were affected on smoke downwash pattern. When the ratio of the jet velocity to the mean velocity of the wind tunnel decreased, the smoke curves until it became almost horizontal to the ground because it is accompanied by more rapid entrainment ambient air into the smoke.

CHAPTER 7
CONCLUSIONS AND FURTURE WORKS

7.1 Conclusions

The objective in this dissertation is three folds as follows:

(1) the patterns of smoke dispersion ejecting with hot-smoke from the chimney and its occurrence conditions were investigated in an active turbulence grid (to promote quasi-isotropic turbulence) and a rectangular grid (to generate grid turbulence).

(2) the scaling law of the critical condition on appearance of the downwash pattern of the hot-smoke ejected from the chimney in turbulent crossflow was elucidated, and

(3) the reason and the key to appear the downwash pattern of smoke ejected from the chimney were investigated.

In this dissertation, the structures of the smoke dispersion with the heated jet and the unheated jet from the chimney were investigated with certain experimental conditions under the quasi-isotropic turbulence with the turbulence intensity, u_{rms}/U_0 = 9.5%–11%, and under the grid turbulence with the turbulence intensity, u_{rms}/U_0 = 2.9%–3.5%. In addition, the scaling law was elucidated to provide the critical condition on appearance of the downwash pattern of the hot-smoke ejected from the chimney in the turbulent crossflow; and identified the reason how the downwash pattern occurs of the smoke ejecting from the chimney under certain numerical conditions. The following conclusions were deduced:

(1) The present experiment succeeded in the realization of the meandering smoke dispersion which could be observed in the actual atmospheric boundary layer. This meandering smoke dispersion was realized in the quasi-isotropic turbulence generated by the atmospheric wind tunnel with the active turbulence grid, suggesting that using active turbulence generator with the lab-scale wind tunnel is quite powerful tool to predict the actual smoke dispersion observed in the wide range of the wind condition. The smoke diffused more widely by the meandering motion by the large integral scale in the case of the high jet velocity and the low crossflow velocity in the high turbulence Reynolds number, suggesting that the turbulent eddies corresponding to the integral scale effectively contribute to the meandering smoke diffusion. Compared in the unheated jet, the meandering smoke structure in the heated jet with higher

temperature occurred in the condition of the lower jet velocity and the higher crossflow velocity.

(2) The structures of the smoke dispersion were divided into the six modes. For the Modes I and II, the two longitudinal vortex tubes were generated without and with strongly mutual interaction, respectively. The bifurcation structure was produced by the buoyancy force near the jet exit when the buoyancy was dominant. For the Mode III, the hairpin-type vortices occurred by the Kelvin-Helmholtz instability. For the Mode IV, the structure was comprised of the developed coherent vortices and the turbulent vortices. For the Mode V, the meandering structure was affected of the turbulent motion. For the Mode VI, the downwash structure occurred behind the chimney. This smoke diffusion was depended on the turbulent motion, the inertia force, the buoyancy force, etc. The Mode V, the meandering dispersion, occurred in the quasi-isotropic turbulence. On the other hand, the Modes I-IV appeared in the grid turbulence. The Mode VI, the downwash dispersion, occurred both in the quasi-isotropic turbulence and in the grid turbulence.

(3) The Mode VI, the downwash pattern occurred behind the chimney, preferred to appear under the quasi-isotropic turbulent case, implying that the selection of proper turbulent field was strongly demanded to predict the condition to have direct smoke exposure.

(4) In the quasi-isotropic turbulence case, the variations of the smoke diffusion width with an increase of downstream distance almost agreed with Sutton's correlation for neutral air stability case. The concentration distribution of smoke could be estimated using equation on the diffusion of air pollution from point source with experimentally obtained constants.

(5) The critical condition for the appearance of the downwash pattern was elucidated. It was found that inertia force of wind, the buoyancy of smoke, inertia force of smoke, and viscous effect around the chimney were equally responsible for the appearance of the downwash pattern, while the chimney height did not affect much on the appearance of the downwash pattern. The observed data were summarized in the physical plane to propose the potential scaling law of jet-Froude number and Reynolds number and it was found that all plots were collapsed into the single line. Although further verification is needed, this proposed scaling law worked well to describe the critical condition of the appearance of the downwash pattern under the condition studied in the present work.

(6) The downwash pattern was the phenomenon in which the smoke from the chimney was drop down into low-pressure region in the wake of the chimney which caused by low-speed zones appear at the behind of the chimney. Definition of the downwash condition

was that the high-concentration smoke reaches to the ground level in downstream to cause the potential health damage.

(7) The downwash pattern appeared under the condition of the high cross-wind velocity and the low jet velocity. It meant that the inertial force and the turbulent motion were affected on smoke downwash pattern. When the ratio of the jet velocity to the mean velocity of the wind tunnel decreased, the smoke curves until it became almost horizontal to the ground because it was accompanied by more rapid entrainment ambient air into the smoke.

(8) The numerical approach could be observed and clarified the smoke downwash phenomena to gain more detailed physics with the insightful understanding from scientific way.

Based on the above conclusion, it displayed to Fig. 7.1.

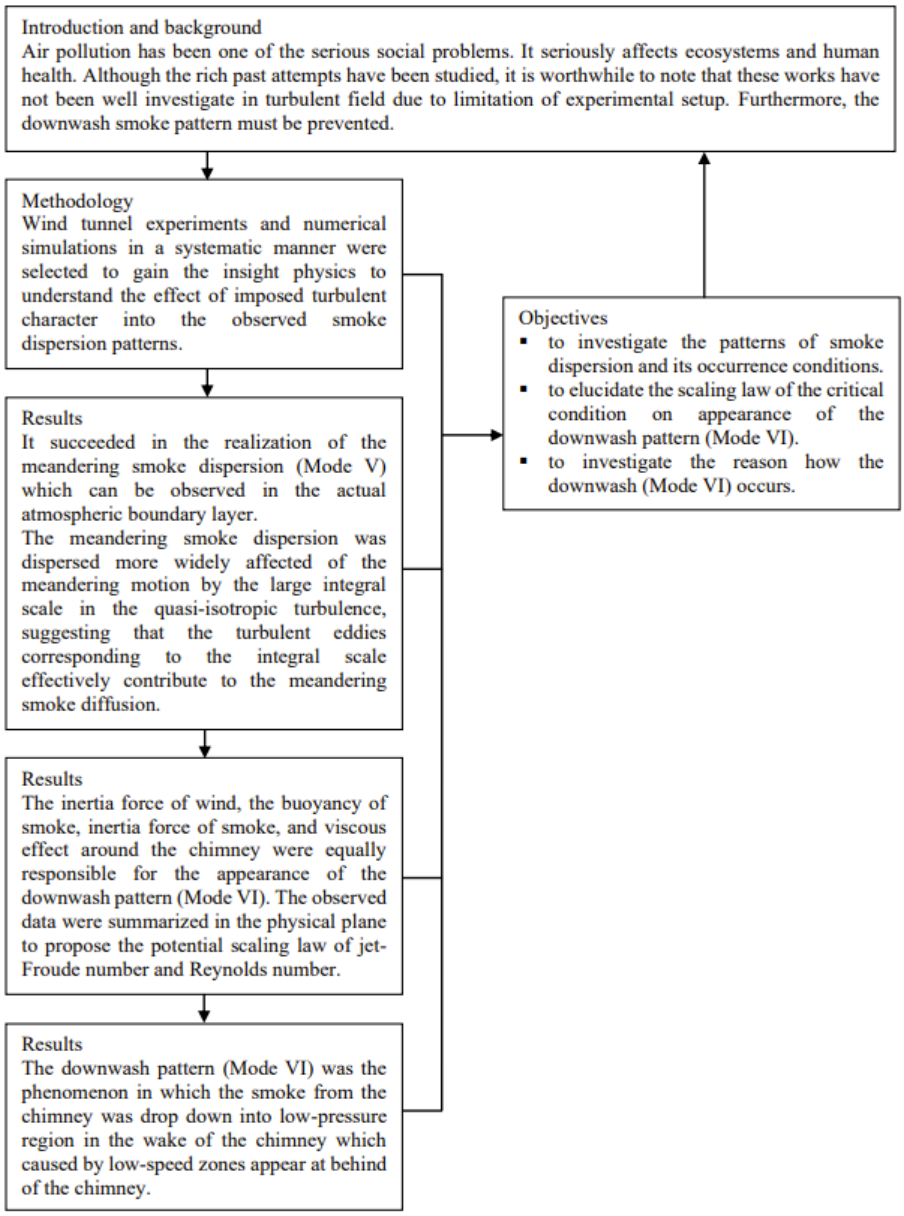

Fig. 7.1 Summarize conclusions.

7.2 Future works

For future work, it should be concerned whether the proposed scaling law is universal or conditional. For instance, this research only focused on the range of the velocity ratio between the jet velocity and the cross-wind velocity around 1 as stated in Eq. (5.2) and the results were obtained by using the single chimney size (no dependency on the characteristic length was taken into account). Indeed, supposing that the actual scale of the chimney (because the characteristic length of the chimney (its diameter) is in order of meters) is considered, jet

Reynolds number becomes extremely larger, suggesting that the viscosity force is relatively negligible. Other forces may be needed to drive the downward force instead of the negative pressure generated by the vortex. To confirm this issue, working on a wide range of testing data is demanded to verify the potential scaling law, which will be also the focus of the future work. As suggested, numerical approach would be valuable on this regard. This technique which is based on numerical models can be more advantageous than the experimental methods in many ways, such as the richness of the quantitative results, low cost, and rapid turnaround time. For instance, we could increase wide ranged of the cross-wind velocity and jet velocity, could change the size and shape of the chimneys to investigated on this regards (for future work). Due to limited time, our work could not be accomplished in wide range of tests, consequently, the wide range of testing is still demanded to verify the potential scaling law, which will be also the focus of the future work.

REFERENCES

Adel, A. A. R., On the atmospheric dispersion and Gaussian plume model, 2nd International Conference on Waste Management, Water Pollution, Air Pollution, Indoor Climate (WWAI'08), Corfu, Greece, October 26-28, (2008), pp.31–39.

Alessandrini, S., Ferrero, E. and Anfossi, D., A new Lagrangian method for modelling the buoyant plume rise, Atmospheric Environment, 77, (2013), pp.239–249.

Aunan, K., Hansen, M. H., Liu, Zh. and Wang, Sh., The hidden hazard of household air pollution in rural China, Environmental Science and Policy, 93, (2019), pp.27–33.

ATSDR (Agency for Toxic Substances and Disease Registry), Toxicological Profile for Carbon Monoxide, U.S., Department of Health and Human Services, Public Health Service, Agency for Toxic Substances and Disease Registry (ATSDR), (2012), DOI:https://www.atsdr.cdc.gov/ToxProfiles/tp201.

Azagba, S., Latham, K. and Shan, L., Exposure to secondhand smoke in vehicles among Canadian adolescents: Years after the adoption of smoke-free car laws, Addictive Behaviors Reports, 10, (2019), pp.1–7.

Bailly, C., Turbulence, Springer International Publishing Switzerland, (2015), DOI:10.1007/978-3-319-16160-0.

Baouabe, I. B., Bournot, H., Said, N. M., Mhiri, H. and Palec, G.L., Experimental and numerical analysis of the jet dispersion from a bent chimney around an obstacle, Heat Mass Transfer, 47, (2011), pp.323–342.

Batchelor, G. K., The theory of homogeneous turbulence, Cambridge university press, (1953).

Bayat, R., Ashrafi, Kh., Motlagh, M. Sh., Hassanvand, M. S., Daroudi, R., Fink, G. and Kunzli, N., Health impact and related cost of ambient air pollution in Tehran, Environmental Research, 176, (2019), pp.1–12.

Bjorklund, J. R. and Bowers, J. F., User's instruction for the SHORTZ and LONGZ computer programs, Volumes I and II. EPA Document EPA-903/9-82-004A and B. US EPA, Middle Atlantic Region III, Philadelphia, Pennsylvania, USA. (1982).

Briggs, G. A., Plume rise, Printed in the United States of America USAEC Division of Technical Information Extension, Oak Ridge, Tennessee, (1969).

Briggs, G. A., Diffusion estimation for small emissions, Air Resources Atmospheric Turbulence and Diffusion Laboratory, NOAA Environmental Resource Laboratory, Oak Ridge, Tennessee, (1973), pp.1–64.

Briggs, G. A., Plume rise and buoyancy effects, Atmospheric Science and Power Production (ed.: Randerson D.), DOE/TIC 27601, Department of Commerce, Springfield, USA, (1984).

Brusca, S., Famoso, F., Lanzafameb, R., Garrano, A. M. C. and Monforte, P., Experimental analysis of a plume dispersion around obstacles, Energy Procedia, 82, (2015), pp.695−701.

Canepa, E., An overview about the study of downwash effects on dispersion of airborne pollutants, Environmental Modelling & Software, 19, (2004), pp.1077−1087.

Canepa, E., Modesti, F. and Ratto, C. F., Evaluation of the SAFE_AIR code against air pollution field and laboratory experiments, Atmospheric Environment, 34 (28), (2000), pp.4805−4818.

Carruthers, D. J., Holroyd, R. J., Hunt, J. C. R., Weng, W. S., Robins, A. G., Apsley, D. D., Smith, F. B., Thomson, D. J. and Hudson, B., UK atmospheric dispersion modelling system, In: Van Dop H., Kallos G. (eds.), Air Pollution Modelling and its Applications IX, Plenum Press, New York, (1992).

Cengel Y. A. and Cimbala J. M., Fluid Mechanics-Fundamentals and Applications, McGraw-Hill Higher Education, New York, (2006).

Chen, F. and Leong, J. C., Smoke flow phenomena and turbulence characteristics of tunnel fires, Applied Mathematical Modelling, 35, (2011), pp.4454−4566.

Cheung, T. W., Study of plume equation using salt water modeling, International Journal on Engineering Performance-Based Fire Codes, Vol.6, (2004), pp.291−294.

Chitsomboon, T., Construction and interpretation of dimensionless variables in a new way, The 15th Conference of Mechanical Engineering Network of Thailand (ME-NETT 2001), (2001), Thailand.

Corrsin, S., Local Isotropy In Turbulent Shear Flow, National Advisory Committee for Aeronautics, Research Memorandum, (1958), pp.1−17.

Dahm, W. J. A. and Dimotakis, P. E., Mixing at large Schmidt number in the self-similar far field of turbulent jets, J. Fluid Mech., Vol.217, (1990), pp.299−330.

Ghenai, C. and Lin, C. X., Dispersion modeling of PM10 released during decontamination activities, Journal of Hazardous Materials, Vol.132, Iss. 1, (2006), pp 58−67.

Gifford, F., Statistical properties of a fluctuating plume dispersion model, Advances in Geophysics, Vol.6, (1959), pp.117−137.

Gifford, F. A., Use of routine meteorological observations for estimating atmospheric dispersion, Nuclear Safety, 2, (1961), pp. 47−51.

Gnatowska, R., A study of downwash effects on flow and dispersion processes around buildings in Tandem arrangement. Pol. J. Environ. Stud, 24(4), (2015), pp.1571−1577.

Graber, M., Mohr, S., Baptiste, L., Duloquin, G., Mariet, A. S., Giroud, M. and Bejot, Y., Air pollution and stroke. A new modifiable risk factor is in the air, Revue neurologique (2019), DOI:10.1016/j.neurol.2019.03.003.

Guo, H., Chang, Zh., Wu, J. and Li, W., Air pollution and lung cancer incidence in China: Who are faced with a greater effect?, Environment International, 132, (2019), pp.1−16.

Gupta, A., Stathopoulos, T. and Saathoff, P., Wind tunnel investigation of the downwash effect of a rooftop structure on plume dispersion, Atmospheric Environment, 46, (2012), pp.496−507.

Guyon E., Hulin J. P., Petit L., Mitescu C. D., Physical-Hydrodynamics, 2nd edition, Oxford University Press, (2017).

Hanna, S. R. and Chang, J. C., Hybrid plume dispersion model (hpdm) improvements and testing at three field sites, Atmospheric Environment, 27A, (1993), pp.1491−1508.

Hatton, A. P. and Carpenter, C., Sixth thermodynamics and fluid mechanics convention (Institution of Mechanical Engineers, pp.81−89). London and New York: Mechanical Engineering Publication, (1976).

Hu, L. H., Xu, Y., Zhu, W., Wu, L., Tang, F. and Lu, K. H., Large eddy simulation of pollutant gas dispersion with buoyancy ejected from building into an urban street canyon, Journal of Hazardous Materials, 192, (2011), pp.940−948.

Hu, Y. and Duan, X., PM2.5 dispersion prediction based on Gaussian Plume model and Multiple Linear Regression model, Journal Arid Land Resources and Environment, 29 (6), (2015), pp. 86−92.

Huang, R. F. and Hsieh, R. H., An experimental study of elevated round jets deflected in a crosswind, Experimental thermal fluid science, 27, (2002), pp.77−86.

Huber, A. H. and Snyder, W. H., Building wake effects on short stack effluents, Preprints, Third Symposium on Atmospheric Turbulence, Diffusion, and Air Quality. 19–22 October 1976, Raleigh, NC, American Meteorological Society, Boston, MA, (1976), pp.235–242.

Jarrin, N., Synthetic Inflow Boundary Conditions for the Numerical Simulation of Turbulence, PhD thesis, The University of Manchester, Manchester M60 1QD, United Kingdom, (2008).

John, R. B., Household air pollution from domestic combustion of solid fuels and health, The Journal of Allergy Clinical and Immunology, Vol.143, (2019), pp.1979–1987, DOI: 10.1016/j.jaci.2019.04.016.

Kistler, A. L. and Vrebalovich, T., Grid turbulence at large Reynolds numbers, Journal of Fluid Mechanics, Vol. 26, (1966), pp. 37–47, DOI: 10.1017/S0022112066001071.

Kuo, K. K., Principles of Combustion, 2nd edition, John Wiley & Sons, Inc., Hoboken, New Jersey, (2005).

Kwon, S. J. and Seo, I. W., Reynolds number effects on the behavior of a non-buoyant round jet, Experiments in Fluids, 38, (2005), pp.801–812, DOI: 10.1007/s00348-005-0976-6.

Lee, D., Robertson, Ch., Ramsay, C., Gillespie, C. and Napier, G., Estimating the health impact of air pollution in Scotland, and the resulting benefits of reducing concentrations in city centres, Spatial and Spatio-temporal Epidemiology, 29, (2019), pp.85–96.

Leelossy, A., Molnar, F. Jr., Izsak, F., Havasl, A., Lagzl, I. and Meszaros, R., Dispersion modeling of air pollutants in the atmosphere: a review, Central European Journal of Geosciences, 6(3), (2014), pp.257–278.

Lerner, J. C., Wind Tunnels and Experimental Fluid Dynamics Research, (2011), DOI: 10.5772/730.

Li, K., Chen, W., Liang, M., Zhou, J., Wang, Y., He, Sh., Yang, J., Yang, D., Shen, H. and Wang, X., A simple data assimilation method to improve atmospheric dispersion based on Lagrangian puff model, Nuclear Engineering and Technology, 53, (2021), pp. 2377–2386.

Lui, F., Lui, Y., Xiong, K., Weng, M. and Wang, J., Experimental and numerical study on the smoke movement and smoke control strategy in a hub station fire, Tunnelling and Underground Space Technology, 96, (2020), pp. 1–13.

Majeski, A. J., Wilson, D. J. and Kostiuk, L. W., Predicting the length of low-momentum jet diffusion flame in cross flow, Combustion Science and Technology, 176:12, (2010), pp.2001–2025.

Makita, H., Forefront of Wind-Tunnel Experiment on Turbulence Structure, Journal of Fluid Science and Technology, Vol. 2, No. 3, (2007), pp.525–534.

Makita, H., Realization of a large-scale turbulence field in a small wind tunnel, Fluid dynamic research, 8, (1991), pp. 53–64.

Mallinson, G. D., Computational fluid dynamics lecture notes, Department of Mechanical Engineering, University of Auckland, (1999).

McGrattan, K., McDermott, R., Forney, G., Overholt, K. and Weinschenk, C., Fire Modeling for the Fire Research, Fire Protection, and Fire Service Communities, Fire Protection Engineering Journal, September 8, (2014), https://www.nist.gov/publications/fire-modeling-fire-research-fire-protection-and-fire-service-communities.

McGrattan, K., Hostikka, S., Floyd, J., McDermott, R. and Vanella, M., Fire dynamics simulator (Sixth Edition): technical reference guide, volume 1: Mathematical Model, NIST Special Publication 1018-1, (2021a), pp. 1–207.

McGrattan, K., McDermott, R., Vanella, M., Hostikka, S. and Floyd, J., Fire dynamics simulator (Sixth Edition): user's guide, NIST Special Publication 1019, (2021b), pp.1–424.

Michael, How Hot Does A Chimney Flue Get, reported on 13 October 2021, https://yardenly.com/home/how-hot-does-a-chimney-flue-get/.

New, T. H., Lim, T. T. and Luo, S.C., Effects of jet velocity profile on a round jet in cross flow, Experiments in Fluids, 40, (2006), pp.859–875.

Oka, Y., Sugawa, O. and Imamura, T., Correlation of temperature rise and velocity along an inclined fire plume axis in crosswinds, Fire Safe Journal, 43, (2008), pp.391–400.

Olesen, H. R., The model validation exercise at model: overview of results, Int. J. Environmental Pollution, Vol.5, (1995), pp.761–784.

Overcamp, T. J., A review of the conditions leading to downwash in physical modeling experiments, Atmospheric Environment, 35, (2001), pp.3503-3508.

Pasquill, F., Atmospheric diffusion, 2nd Edition, Ellis Horwood limited publisher, Chichester, (1974), pp. 1–714.

Pournazeri, S., Princevac, M. and Venkatram., Scaling of building affected plume rise and dispersion in water channels and wind tunnels-Revisit of old problem, Journal of Wind Engineering and Industrial Aerodynamics, 103, (2012), pp.16–30.

Rae, W. H. and Pope, A., Low-Speed Wind Tunnel Testing, Second edition, John Wiley & Sons, Inc, Canada, (1984).

Raman, R. S. and Ramachandran, S., Annual and seasonal variability of ambient aerosols over an urban region in western India, Atmospheric Environment, 44, (2010), pp.1200–1208.

Reynolds, O., An Experimental Investigation of the Circumstances which determine whether the Motion of Water shall be Direct or Sinuous, and of the Law of Resistance in Parallel Channels, Philosophical Transactions of the Royal Society of London, Vol.174, (1883), pp.935–982.

Reynolds, O., On the dynamical theory of incompressible viscous fluid and the determination of the criterion, Philosophical Transactions of the Royal Society of London, 186 (1895), pp.123–164.

Said, N. M., Mhiri, H., Palcc, G. L. and Bournot, P., Experimental and numerical analysis of pollutant dispersion from a chimney, Atmospheric Environment, 39, (2005), pp.1727−1738.

Saito, K. and Williams, F.A., Scale modeling in the age of high-speed computation, Progress in Scale Modeling, Volume II, Springer (2015), pp.1−18, ISBN 978-3-319-10307-5.

Scott, G.M., Computational fluid dynamics for the food industry, Journal of Food Technology International Europe, (1994), pp.49−51.

Scott, G. M. and Richardson, P., The application of computational fluid dynamics in the food industry, Trends in Food Science and Technology, 8, (1997), pp.119−124.

Sekishita, N., Inthavideth, X. and Phommachanh, S., Wind tunnel experiments on smoke Structure dispersed from a chimney in a cross flow, Proceeding of the 10th AUN/SEED-NET Regional Conference on Mechanical and Manufacturing Engineering, (2019), pp.74−77.

Sherlock, R. H. and Stalker, E. A., A study of flow phenomena in the wake of smokestacks, Engineering Research Bulletin No. 29, University of Michigan, Ann Arbor, (1941), pp.1−64, https://hdl.handle.net/2027/mdp.39015087419175.

Sherlock, R. H. and Lesher, E. J., Role of Chimney Design in dispersion of Waste Gases, Air Repair, 4:2, (1954), pp.13−23, DOI: 10.1080/00966665.1954.10467643.

Singh, A., Pant, P. and Pope, F. D., Air quality during and after festivals: Aerosol concentrations, composition and health effects, Atmospheric Research, 227, (2019), pp.220−232.

Snyder, W. H. and Lawson Jr, R. E., Fluid modeling simulation of stack-tip downwash for neutrally buoyant plumes, Atmospheric Environment, 25A, (1991), pp.2837–2850.

Somchai, W. and Kaewnai, S., Fluid Mechanics (2014), Chula Press, Thailand.

Straja, S., The importance of the pollutant dispersion along the nominal wind direction, Atmospheric Environment, Vol. 28, Iss. 2, (1994), pp.371−374.

Sutton, O. G., A theory of eddy diffusion in the atmosphere, Proceeding of the Royal Society London, A. 135, (1932), pp.143−165.

Tao, Ch., Wang, K., Liu. Q. and He, P. X., A simulation investigation of fire smoke behavior above urban street canyon, Procedia Engineering, 211, (2018), pp.681−688.

Taylor, S. G., The present position in the theory of turbulent diffusion, Advances in Geophysics, Vol.6, (1959), pp.101–112.

Tominaga, Y., Mochida, A., Yoshie, R., Kataoka, H., Nozu, T., Yoshikawa, M. and Shirasawa, T., AIJ guidelines for practical applications of CFD to pedestrian wind environment around buildings, Journal of Wind Engineering and Industrial Aerodynamics, 96, (2008), pp.1749–1761.

Turner, D. B., Workbook of atmospheric dispersion estimates, USEPA, Washington, DC, (1970).

Wang, Z., Lu, K., Feng, L., Tao, Y., Wang, J., Ding, Y. and Shi, C., Simulation on smoke re-circulation transition in an urban street canyon for different fire source locations with cross wind, Safety Science, 127, (2020), pp.1–8.

Wen, J. X., Kang, K., Donchev, T. and Karwatzki, J. M., Validation of FDS for the prediction of medium-scale pool fires, Fire Safety Journal, Vol.42: (2007), pp.127–138.

White, F. M, Fluid Mechanics, 5th edition (2003), the McGraw-Hill Companies, Inc., New York.

Wei, Zh., Jinjin, L., Zhaozhou, L. and Tianshui, L., A study of bifurcation flow of fire smoke in tunnel with longitudinal ventilation, International Journal of Heat and Mass Transfer, 67, (2013), pp. 829–835.

Xu, R., Deng, X., Wan, H., Cai, Y. and Pan, X., A deep learning method to repair atmospheric environmental quality data based on Gaussian diffusion, Journal of Cleaner Production, 308, (2021), pp. 1–11.

Yao, X. and Marshall, A. W., Quantitative salt-water modeling of fire-induced flow, Fire Safety Journal, 41, (2006), pp.497–508.

Yao, X. and Marshall, A. W., Quantitative salt-water modeling of fire-induced flow for convective heat transfer model development, Journal of Heat Transfer, Vol.129, (2007), pp.1373–1383.

Zhu, Q., Liu, Y., Jia, R., Hua, Sh., Shao, T. and Wang, B., A numerical simulation study on the impact of smoke aerosol from Russia forest fires on the air pollution over Asia, Atmospheric Environment, 182, (2018), pp.263–274.

APPENDICES

Appendix A: Gaussian plume model

Gaussian plume model uses a realistic description of dispersion, where it represents an analytical solution to the diffusion equation for idealized circumstances. The model assumes that the atmospheric turbulence is both stationary and homogeneous. In reality, none of these conditions is fully satisfied. However, Gaussian plume model has been successfully used for rural configurations. Extensive validation has been done on tracer experiments conducted in Kincaid and Prairie grass (Olesen ,1995; Carruthers et al., 1992). Gaussian model has also been tested against tracer experiments in urban surroundings (e.g Indianapolis experiment, in (Hanna et al., 1993)). The model is still the method of choice for many (e.g. (Ghenai and Lin, 2006) and (Straja, 1994)), especially for the prediction of yearly averaged concentration. It is the most widely used plume model and is the basis for most of the computer models distributed by the EPA.

In the Gaussian plume dispersion model the concentration of pollution downwind from a source is treated as spreading outward from the centerline of the plume following a normal statistical distribution. The plume spreads in both the horizontal and vertical directions.

In the model, determining the pollutant concentrations at ground-level beneath an elevated plume involves two main steps; first, the height to which the plume rises at a given downwind distance from the plume source is calculated. The calculated plume rise is added to the height of the plume's source point to obtain the so-called "effective stack height". Second, the ground-level pollutant concentration beneath the plume at the given downwind distance is predicted using the Gaussian dispersion equation.

The Gaussian dispersion equation can be written as:

$$C(x,y,z)=\frac{Q}{2\pi\sigma_y\sigma_z u}\exp\left(-\frac{y^2}{2\sigma_y^2}\right)\times\left\{\exp\left(-\frac{(z-H)^2}{2\sigma_z^2}\right)+\exp\left(-\frac{(z+H)^2}{2\sigma_z^2}\right)\right\} \quad \text{(A.1)}$$

which was developed by (Sutton, 1932), where C is the concentration, Q is the emission rate of the pollutant from the source, u is the wind speed which defines the direction x. y is the horizontal distance perpendicular to the wind direction, z is the vertical direction, H is the

effective height of the plume (considering the additional height Δh to which the hot gases rise above the physical height of the source h); i.e., $H = h + \Delta h$, and σ_y and σ_z are the parameters of the normal distributions in y and z directions, usually called the dispersion coefficients in y and z directions, respectively. A definition sketch of the plume dispersion is shown in figure below (Fig. A.1).

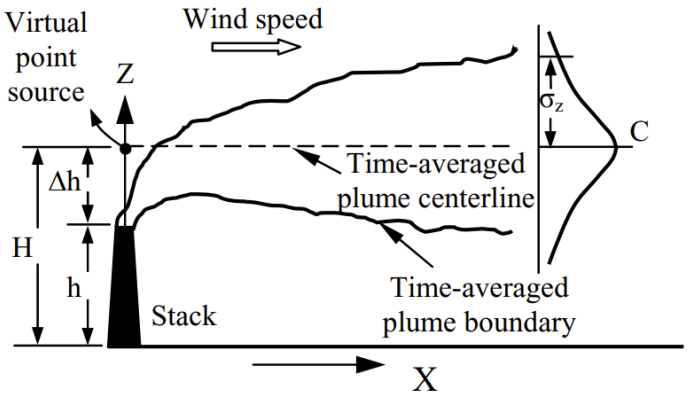

Fig. A.1 Plume dispersion: definition sketch (Adel, 2008).

In this equation, the ground is usually assumed to be a perfect reflector and its presence is represented by a mirror image source placed below ground. For a receptor at the ground surface, or a source located at the ground (z=0), the previous equation reduces to:

$$C(x,y,0)=\frac{Q}{\pi\sigma_y\sigma_z u}\exp\left(-\frac{y^2}{2\sigma_y^2}-\frac{H^2}{2\sigma_z^2}\right) \quad \text{(A.2)}$$

In analyzing the Gaussian plume model, the following assumptions are usually made:

1) Continuous emission and negligible diffusion in the direction of travel.
2) The material diffused is a stable gas or aerosol, with a negligible deposition rate.
3) Mass is conserved through reflection at surfaces.
4) Background pollution is negligible.
5) Steady-state conditions.
6) Constant wind speed and direction with time and elevation.
7) Negligible wind shear effect on horizontal diffusion.
8) The dispersion parameters are assumed to be functions of x (and hence u alone).

9) The terrain is relatively flat, open country.

Plume rise Δh plays an important role in determining ground-level concentrations for real sources. The plume rise schemes of Briggs (Briggs, 1984) are recommended by EPA, and they are the commonly used schemes. These schemes express the final rise height of the buoyant release as a function of, among other parameters, the buoyancy flux, the mean wind speed at the stack top, and the friction velocity.

Gaussian plume models are applicable for downwind distance, x>100 m, because near the source concentration approaches infinity (Briggs, 1973). Accordingly, many researchers imposed a lower limit on $\sigma_y(x)$ and $\sigma_z(x)$, or an upper limit on the near source concentration. The dispersion coefficients, σ, define the spread of the plume. As with the normal distribution, 67% of the pollutant is assumed to be within $\pm\sigma$ of the centerline of the plume. Thus, a plume may be described as being approximately four to six σ wide. The value of σ is determined by the magnitude of the turbulence in the atmosphere. The larger eddies, and larger values of σ, will be observed during periods when the atmosphere is unstable. The smaller eddies, and smaller values of σ, will be observed when the atmosphere is stable.

Measurements of σ have been made under a variety of atmospheric conditions. The measurements of σ used in virtually all the models are those published by Turner (Turner, 1970) (called the "Pasquill-Gifford coefficients") from data taken in open, rural surroundings. Because of their origin they are appropriate for dispersion estimates in rural settings but less so for urban areas. The greater surface roughness and greater release of heat at the surface means that atmospheric conditions in urban areas are seldom as stable as in rural areas.

The measurements of the Pasquill-Gifford coefficients were made over periods of 10 to 20 minutes and are strictly applicable only to such short time periods. In order to calculate long-term (e.g., annual) average concentrations, it is necessary to take into account the wind speed, direction, and atmospheric stability over the entire period.

The physical description of the Gaussian plume model is based on the traditional discrete stability categories (Pasquill-Turner stability classes). The atmosphere is generally described as being in six stability classes, labeled A through F. Classes A through C are unstable conditions, class D is neutral, and classes E and F are stable. The most frequently observed classes are C, D, and E as shown in the appendix B.

Appendix B: Dispersion parameters

Dispersion parameters for windy conditions are as shown in Table B.1 which is the approximation of the Pasquill-Gifford chart.

Table B.1 Dispersion parameters for windy conditions (Gifford, 1961).

$$\sigma_y(x)=\gamma_y \cdot x^{\alpha_y}$$

Atmospheric stability	α_y	γ_y	Down-wind distance, x(m)
A	0.901	0.426	0-1000
	0.851	0.602	1000-…
B	0.914	0.282	0-1000
	0.865	0.396	1000-…
C	0.924	0.1772	0-1000
	0.885	0.232	1000-…
D	0.929	0.1107	0-1000
	0.889	0.1467	1000-…
E	0.921	0.0864	0-1000
	0.897	0.1019	1000-…
F	0.929	0.0554	0-1000
	0.889	0.0733	1000-…
G	0.921	0.0380	0-1000
	0.896	0.0452	1000-…

$$\sigma_z(x)=\gamma_z \cdot x^{\alpha_z}$$

Atmospheric stability	α_z	γ_z	Down-wind distance, x(m)
A	1.122	0.0800	0-300
	1.514	0.00855	300-500
	2.109	0.000212	500-…

B	0.964 1.094	0.1272 0.0570	0-500 500-…
C	0.918	0.1068	0-…
D	0.826 0.632 0.555	0.1046 0.400 0.811	0-1000 1000-10000 10000-…
E	0.788 0.565 0.415	0.0928 0.433 1.732	0-1000 1000-10000 10000-…
F	0.784 0.526 0.323	0.0621 0.370 2.41	0-1000 1000-10000 10000-…
G	0.794 0.637 0.431 0.222	0.0373 0.1105 0.529 3.62	0-1000 1000-2000 2000-10000 10000-…

A – Extremely unstable

B – Moderately unstable

C – Slightly unstable

D – Neutral

E – Slightly stable

F – Moderately stable

G – Extremely stable

Appendix C: Scale modeling and the law approach

Scale modeling involves the use of physical models, whose size is either smaller or larger than that of the full-scale system (which is called the prototype in the technical literature), to conduct experiments for the purpose of testing the scaling laws, attempting to validate them (confirmation tests), or to use validated scale models in various applications (production tests). Fig. C.1 shows a flow diagram that describes the concepts of scale modeling in relationship to those of numerical modeling. Both scale modeling and numerical modeling begin, in the first step, with assumptions. However, there is no well-established logical prescription available for obtaining reasonably good assumptions (RGA), and an individual researcher must rely on her/his unique thinking or intuition to arrive at RGA. Through this struggle, some may be able to develop Kufu eyes to obtain RGA rather than not good assumptions (NGA). This step is followed by the deductive processes indicated in the figure, which are different, depending on whether the approach to be applied is scale modeling or numerical simulation. In other words, if it comes up with RGA, then the final result can be right, independent of the technique, while if it starts with NGA, then the final result must be wrong. Moreover, the two approaches can be complementary, as discussed in detail on the relationships between scale modeling and numerical modeling (Saito and Williams, 2015).

There are indicated that scale modeling involves obtaining pi numbers, for which three different kinds of approaches are available: the parameter approach (identifying parameters involved in the full-scale phenomena and then using Buckingham's pi theorem), the equation approach (ascertaining the governing equations and then converting them into non-dimensional form), and the law approach (determining the governing physical laws and then describing each of them with representative characteristic parameters). The above texts detail all three approaches and recommend the use of the law approach in most cases, since it can help researchers to better understand the governing mechanisms and hence provides a better chance of reaching RGA. First address the relationships of the equation approach and the parameter approach to the law approach.

Contrary to the law approach, the equation approach requires much more detailed information about the phenomenon because it rests upon the development of governing equations by identifying specific interactions among the various parameters involved. This can be quite difficult, and also it often is unnecessary for successful scale modeling. When fully developed equations are available, the equation approach offers the possibility of numerical simulation by directly solving the governing equations. It therefore also underlies addressing

problems by high-speed computation. Nevertheless, it is less universally available in that the law approach can give pi numbers even when such detailed parametric relationships are not known.

The first step of the law approach in Fig. C.1 begins with the identification of RGA, for example, with the help of Kufu eyes. Here researchers are required to identify physical laws that govern the full-scale phenomena. Physical laws in the law approach are often written in terms of forces and energy, since numerous engineering problems deal with them, as has been explained. For example, if researchers have initially identified as three possible forces in a full-scale phenomenon an inertia force, a viscous force, and a gravity force, then, with further thinking and careful observations, they feel justified in making the assumption that the major effects arise from inertia force and gravity forces, while the viscous force is secondary, they end up with one pi number (the presumed controlling dimensionless number), the ratio of the inertia and gravity forces, which is the Froude number. This then becomes the scaling law that appears in the second box along the scale modeling path in Fig. C.1. Such scaling laws give us guidelines and criteria on how to design scale model experiments.

The third box along the scale-modeling path in the figure recommends designing two, three, or possibly more experiments of different sizes. More experiments provide better tests of confirmation but also are more expensive, necessitating trade-offs. In selecting scale models, relatively large-scale ratios are desirable, because normally the larger the scale ratio, the easier it is to test the accuracy of the assumptions. But, on the other hand, all scaling laws apply only over limited ranges of conditions, and therefore, if the scale ratio is too large, there is a higher chance of not satisfying the assumptions of the relationships between the full scale and the scale model that are being tested, and the scaling law becomes invalid. Hence, in this respect as well, trade-offs are needed. When full-scale data are not available, measurements for at least two different size scale models must be performed to test any scaling law. The fourth box along the scale-modeling path in Fig. C.1 represents conducting these scale model tests and measuring the parameters whose values are predicted by the scaling laws. Comparing the results of the measurements with the predictions completes the confirmation test. If the results are deemed to be sufficiently similar, then the scaling law can be considered to be sufficiently well validated for the tests performed; otherwise, the assumptions must be revised to obtain different scaling laws that are then tested by repeating the same procedures. This five-step process is called confirmation testing in scale modeling, and, if successful, it can be followed by production tests, in which the scaling laws are applied at different scales of practical interest. It must be kept in mind, however, that the confirmation applies only over the scale range tested and may not

represent well the full-scale phenomenon if its scale is too different from those tested. For more detail can be found in article of Saito and Williams, (2015).

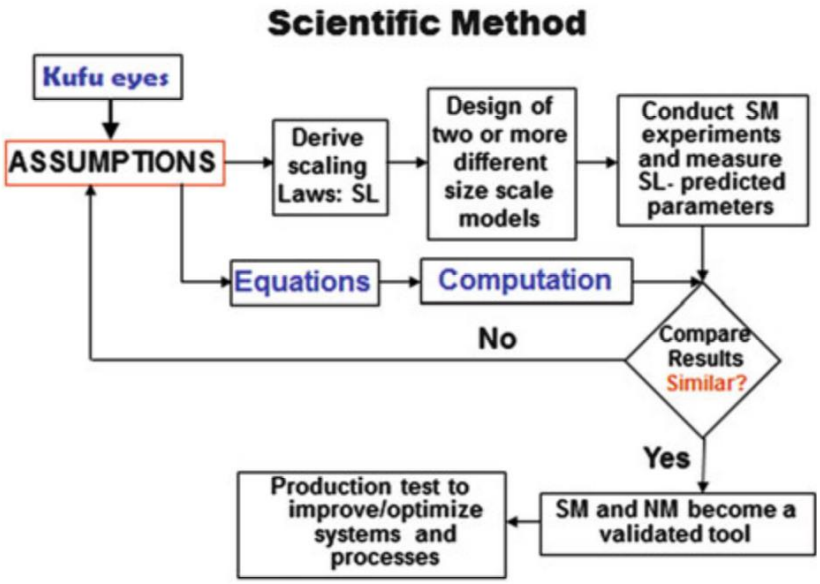

Fig. C.1 Basic concept of scale modeling and numerical simulation (Saito and Williams, 2015).

Appendix D: Glossary of terms

Adiabatic lapse rate	The rate at which air lifted adiabatically cools owing to the drop of pressure with increasing height, 9.8 ^{o}C/km in the earth's atmosphere.
Advection	The transport of a fluid property by the mean velocity field of the fluid.
Buoyant plume	A plume initially of lower density than the ambient fluid after the pressure is adiabatically brought to equilibrium. Usually, the term "buoyant plume" refers to a plume in which the effect of the initial momentum is small, and the term "forced plume" refers to a plume with buoyancy in which the effect of the initial momentum is also important.
Convection	Mixing motions in a fluid arising from the conversion of potential energy of hydrostatic instability into kinetic energy. It is more precise to term this motion "free convection" to distinguish it from "forced convection," which arises from external forces.
Critical wind speed	In the context of this critical review, the wind speed at the height of an elevated plume for which the maximum ground concentration is highest in neutral conditions.
Diffusion	The mixing of a fluid property by turbulent and molecular motions within the fluid.
Downwash	The downward motion of part or all of a plume due to the lower pressure in the wake of the chimney or building or due to a downward step of the terrain.
Effective chimney height	Variously defined. The three most common definitions are: (1) the height at which a plume levels off, which has been observed only in stable conditions; (2) the height of a plume above the point of maximum ground concentration; (3) the virtual height of plume origin based on the diffusion pattern at large distances downwind of the chimney. Definition 1 is the easiest to apply in stable conditions; definition 2 is the most practical in neutral

	and unstable conditions; definition 3 is comprehensive but difficult to apply.
Efflux velocity	The mean speed of exiting chimney gases.
Entrainment	The dilution of plume properties due to mixing with the ambient fluid.
Final rise	The total plume rise after leveling off, if this occurs, especially as opposed to the term “transitional rise.”
Froude number	The ratio of pressure forces to buoyant forces.
Fumigation	The downward diffusion of pollutants due to convective mixing underneath an inversion that prevents upward diffusion.
Inversion	A layer of air in which temperature increases with height. Such a layer is also stable.
Jet	A nonbuoyant plume.
Lapse rate	The rate at which temperature drops with increasing altitude; the negative of the vertical temperature gradient.
Neutral	In hydrostatic equilibrium. A neutral atmosphere is characterized by an adiabatic lapse rate, i.e., by potential temperature constant with height.
Plume rise	The rise of a plume center line or center of mass above its point of origin due to initial vertical momentum or buoyancy, or both.
Potential temperature	The temperature that a gas would obtain if it were adiabatically compressed to some standard pressure, usually 1000 mb in meteorological literature.
Stable	Possessing hydrostatic stability. A stable atmosphere has a positive potential temperature gradient.
Stratification	The variation of potential temperature with height. Usually the term “stratified fluid” refers to a fluid possessing hydrostatic stability, as does the atmosphere when the potential temperature gradient is positive.
Temperature gradient	In meteorology, usually the vertical gradient of mean temperature.
Transitional rise	The rise of a plume under the influence of the mean wind and the properties of the plume itself; i.e., the rise before atmospheric turbulence or stratification has a significant effect.

Turbulence	Three-dimensional diffusive motions in a fluid on a macroscopic scale. According to Lumley and Panofsky,' turbulence is also rotational, dissipative, nonlinear, and stochastic.
Unstable	Possessing hydrostatic instability. An unstable atmosphere has a negative potential temperature gradient.

Appendix E: List of publications

International Journals

1. Inthavideth, X., Sekishita, N., Phommachanh, S. and Nakamura, Y., Experimental study on the effect of turbulence on hot-smoke dispersion ejecting in a cross flow, Journal of Thermal Science and Technology, Vol.17, No.1, (2022), pp.1−14, DOI: 10.1299/jtst.21-00296.
2. Inthavideth, X., Sekishita, N., Phommachanh, S. and Nakamura, Y., Scale modeling of an appearance of downwash pattern of hot smoke ejected from chimney in the turbulent cross flow, Progress in Scale Modeling, an International Journal, Vol. 03, Iss. 1, Article 4, (2022), pp.1−10, DOI: 10.13023/psmij.2022.03-01-04.

International conferences

1. Sekishita, N., Inthavideth, X. and Phommachanh, S., Wind tunnel experiments on smoke Structure dispersed from a chimney in a cross flow, Proceeding of the 10th AUN/SEED-NET Regional Conference on Mechanical and Manufacturing Engineering, pp.74–77, 7th-8th November 2019, Phnom Penh, Cambodia.
2. Inthavideth, X., Sekishita, N. and Phommachanh, S., Wind tunnel experiments on smoke diffusion from a chimney, the 11th AUN/SEED-NET Regional Conference on Mechanical and Manufacturing Engineering, IOP Conference Series: Materials Science and Engineering, Vol.1109, (2021), pp.1−7, 14th-15th January 2021, De La Salle University, Manila, Philippines. DOI:10.1088/1757-899X/1109/1/012055.
3. Inthavideth, X., Sekishita, N., Phommachanh, S. and Nakamura, Y., Scale modeling experiment for better prediction of hot smoke dispersion from the chimney, the 9th International symposium on scale modeling, pp.155−158, 02nd-04th March 2022, Napoli, Italy.